

MASTER'S THESIS

Sum Rules for the Extended Higgs Sector Models: A comparative analysis of 2HDM, GM and the Septet Model

presented by

Sara Chopra

Faculty: II. Institute of Theoretical Physics

Department of Physics

Course of Studies: Accelerator and Particle Physics

Matriculation Number: 7597332

Supervisor: Prof. Dr. Gudrid Moortgat Pick

University of Hamburg

Co-supervisor: Prof. Dr. Sven Heinemeyer

IFT (CSIC), Madrid, Spain

Acknowledgments

I would like to express my gratitude towards everyone who constantly guided and supported my endeavors during my masters at Universität Hamburg and made this thesis possible. I would, first and foremost, like to thank Prof. Dr. Gudrid Moortgat-Pick and Prof. Dr. Sven Heinemeyer for their constant support, guidance for the direction of thesis and to help me grow my academic and soft skills. They also provided an environment for me where I could learn so much and overcome the challenges I faced. And finally, for instilling and improving my critical thinking, which I am sure will be very helpful for me in my journey ahead.

I would also like to express my appreciation for Saurav Bania and his significant contributions to this project. His support and team-spirit made this thesis, truly a wonderful and enriching experience. Special thanks to Prof. Dr. Heather Logan, Ting Kuo Chen, and Prof. Dr. Cheng Wei Chiang for their research and guidance during the project.

I would also like to thank all the people, in “THDM working group”, which gives us the opportunities to present the work, and sharing the interesting ideas together. I would like to express my appreciation to my family, my parents and my sister, and my close friends, including Rohan Gupta. Their support has helped me overcome the challenges I faced during my masters at Universität Hamburg, Germany. Finally, I would like to thank all those who have contributed to my research in any way. Without their support, this work would not have been possible.

List of Contents

Acknowledgments	i
1 Introduction and Motivation	1
1.1 Structure of the Thesis	2
1.2 The Standard Model of Particle Physics	3
1.2.1 Electroweak Symmetry Breaking and Higgs Mechanism	4
1.2.2 Higgs Couplings to Gauge Bosons and Fermions	6
1.3 Constraints on Extended Higgs Model Theories	6
1.3.1 The ρ Parameter	7
1.3.2 Unitarity Constraints and Sum Rules	8
1.3.3 Higgs–Vector Boson Coupling and Unitarity Conservation in the SM	9
1.4 Tree-Level Contributions to $W^+W^- \rightarrow W^+W^-$	10
2 Extended Higgs Sector Models	15
2.1 Two Higgs Doublet Model (2HDM)	16
2.1.1 Motivation and Overview	16
2.1.2 Scalar Field Content and Potential	16
2.1.3 Spontaneous Symmetry Breaking and Field Decomposition	16
2.1.4 Tadpole Conditions and Mass Matrices	17
2.1.5 Electroweak Lagrangian and Higgs Couplings	18
2.1.6 Tree-Level Higgs Couplings to Gauge Bosons	19
2.2 Georgi-Machacek Model (GM)	21
2.2.1 Motivation and Overview	21
2.2.2 Field Content and Bi-Triplet Structure	21
2.2.3 Vacuum Alignment and Custodial Symmetry	22
2.2.4 Scalar Potential and Tadpole Conditions	23
2.2.5 Tadpole Conditions and Custodial Multiplets	23
2.2.6 Multiplet Structure due to Custodial Symmetry and the Scalar Physical Spectrum	24
2.2.7 Custodial Decomposition and Physical Spectrum from Gauge field in GM model	24
2.2.8 Electroweak Lagrangian and Gauge Boson Couplings in the GM Model . . .	26
2.3 The Scalar Septet Model	29
2.3.1 Physical Spectrum and Mixing of Gauge states to Physics states	30

2.3.2	Couplings to Gauge Boson	31
3	Higgs and Vector Boson Scattering Unitarity Sum Rules	34
3.1	Vector Boson Scattering in the 2HDM	34
3.2	Vector Boson Scattering in the GM Model	35
3.3	Vector Boson Scattering in the Septet Model	37
3.4	Theoretical Mass Bounds from Perturbative Unitarity Constraints	38
3.4.1	Standard Model	39
3.4.2	Two-Higgs-Doublet Model	39
3.4.3	Georgi–Machacek Model	40
3.4.4	Scalar Septet Model	41
4	Comparative Analysis of Extended Higgs Sectors and Experimental Limits	43
4.1	Comparative Analysis of extended Higgs models	43
4.1.1	Field Content and Physical Spectrum	43
4.1.2	VEV Structure and Mixing Angles	44
4.1.3	Higgs and Vector Boson Effective Couplings and Sum Rules	45
4.2	Experimental limits on extended Higgs models	48
4.3	Effective Couplings of heavy Higgs States Constrained by $\kappa_V^{h^0}$	49
4.3.1	Heat maps for $\kappa_V^{h^0}$ and 2σ constraint	49
4.3.2	Heat maps for $\kappa_V^{H^0}$ constrained by the 2σ $\kappa_V^{h^0}$ Experimental Limits	52
4.3.3	Heat maps for $\kappa_{WW}^{H^{++}}$ constrained by the 2σ $\kappa_V^{h^0}$ experimental limits	53
4.3.4	Numerical 2σ intervals for effective couplings for all Higgs states for the extended Higgs models	55
5	HiggsTools Framework and Analysis Strategy	56
5.1	Exclusion Logic and Ratios	57
5.2	Parameter Scan Setup	57
5.3	Post-processing and Physics Filters	58
5.4	Data Visualization and Analysis	59
5.4.1	Scatter Panel for BSM model : $\sigma \times \text{BR}$ vs. $\kappa_V^{H^0}$ (allowed points)	59
5.4.2	Channel-wise panels: $\sigma \times \text{BR}$ vs. m_{H^0} (allowed points, model-coloured)	60
5.4.3	Plots for $\kappa_V^{H^0}$ versus m_{H^0} (allowed region)	62
5.4.4	Mass panels for $\kappa_V^{H^0}$ coupling heatmaps with allowed and excluded points	63
5.5	Interpretation of Results	67
6	Summary and Future Prospects	69
6.1	Summary of Theoretical Analysis	69
6.2	Experimental Constraints and the 2σ Higgs–Coupling Band	69
6.3	HiggsTools Analysis and Results	70

6.4 Future Prospects	70
A Perturbative Unitarity in Quantum Field Theory	72
A.1 Unitarity and Partial Wave Expansion	72
A.1.1 Unitarity Constraint	72
A.2 From Quantum Mechanics to Field Theory	73
A.2.1 Tree-Level Unitarity Bound	73
B Mass Matrices in the 2HDM	74
C Custodial Symmetry Transformations in the GM Model	76
D Coupling Structures in the GM Model	78
D.1 Higgs Vector Boson Vector Boson Effective Couplings	78
D.2 Higgs Higgs Vector Boson Couplings	78
E Other Vector Boson Scattering Channels	79
E.1 2HDM: Higgs-mediated $W_L^+ W_L^- \rightarrow Z_L Z_L$ Scattering	79
E.2 2HDM: Higgs mediated $Z_L Z_L \rightarrow Z_L Z_L$ Scattering	79
E.3 GM Model: $W_L^+ W_L^- \rightarrow Z_L Z_L$	80
E.4 GM Model: $Z_L Z_L \rightarrow Z_L Z_L$	80
E.5 Septet Model: $Z_L Z_L \rightarrow Z_L Z_L$	80
E.6 Septet Model: $W^\pm Z \rightarrow W^\pm Z$	81
E.7 Constraints from Perturbative Unitarity on Model Parameters	81
E.7.1 2HDM: Bounds on $\cos^2(\beta - \alpha)$ and m_{H^0}	82
E.7.2 GM Model: Bound on the Fiveplet Mass and s_H	82
E.7.3 Septet Model: Constraint on s_7	83
F Reference plots for κ_V vs. mixing angles at several α	84
G HiggsTools Analysis: Reference paper comparison and consistency checks	85
G.1 Channel wise comparison plots with reference papers	85
G.2 Model-wise most sensitive $\sigma \times \text{BR}$ bands	89
G.2.1 Heatmaps: most-sensitive channel in the $(m_{H^0}, \kappa_V^{H^0})$ plane	89
Eidesstattliche Versicherung	96

List of Figures

Fig. 1.1	Left: Higgs potential for $\mu^2 > 0$, no spontaneous symmetry breaking. Right: Higgs potential for $\mu^2 < 0$, allowing spontaneous symmetry breaking and a non-zero vacuum expectation value at $\pm v$ [23].	5
Fig. 1.2	Feynman diagram for the 4-point vector-boson scattering at tree level, arising from the non-Abelian structure of the $SU(2)_L$ gauge group.	11
Fig. 1.3	Gauge boson exchange diagrams (Z, γ) in the s - and t -channels contributing to $W^+W^- \rightarrow W^+W^-$ scattering. These diagrams partially cancel the high-energy growth from the 4-point vertex.	12
Fig. 1.4	Higgs boson exchange diagrams in the s - and t -channels contributing to $W^+W^- \rightarrow W^+W^-$ scattering. The Higgs diagrams cancel the residual high-energy growth from the gauge sector, restoring unitarity.	12
Fig. 3.1	Feynman diagrams for $W_L^+W_L^- \rightarrow W_L^+W_L^-$ in the 2HDM via h^0 and H^0 exchange in the s - and t -channel.	35
Fig. 3.2	Feynman diagrams for $W_L^+W_L^- \rightarrow W_L^+W_L^-$ scattering in the GM model. Shown are the s - and t -channel exchanges of CP-even scalars h^0, H^0 , and H_5^0 , as well as the u -channel exchange of the doubly charged scalar H_5^{++}	36
Fig. 3.3	Feynman diagrams contributing to $W_L^+W_L^- \rightarrow W_L^+W_L^-$ scattering in the Septet model: s - and t -channel exchange of the CP-even neutral scalars h and H , and u -channel exchange of the doubly charged scalar H^{++}	37
Fig. 3.4	2HDM mass bound from perturbative unitarity. Constraint on the heavy CP-even scalar H^0 as a function of $\kappa_{WW}^{H^0} = \cos(\beta - \alpha)$	40
Fig. 3.5	Georgi–Machacek model: mass bound for H_5^{++}. Constraint derived from the custodial-sum rule of Eq. (3.16) and the s -wave unitarity condition in sec. 3.4; bound shown as a function of $\kappa_{WW}^{H_5^{++}}$ and m_5	41
Fig. 3.6	Septet model: mass bound for H^{++}. Constraint obtained using the septet unitarity relation in sec. 3.4 (see the H^{++} bound) and expressed in terms of $\kappa_{WW}^{H^{++}}$ versus $m_{H^{++}}$	42
Fig. 4.1	Vev structure in the three models: v_2 (2HDM), v_χ (GM), and v_χ (Septet) as functions of the SM-like doublet VEV v_ϕ . The relations $v^2 = v_1^2 + v_2^2$, $v^2 = v_\phi^2 + 8v_\chi^2$, and $v^2 = v_\phi^2 + 16v_\chi^2$ illustrates how extended multiplet contributions decouple as $v_\phi \rightarrow v$	45
Fig. 4.2	2HDM effective couplings $\kappa_{VV}^{h^0}$ and $\kappa_{VV}^{H^0}$ versus β at fixed $\alpha = \pi/4$. The green dotted curve shows $(\kappa_{VV}^{h^0})^2 + (\kappa_{VV}^{H^0})^2$	46
Fig. 4.3	GM effective couplings versus θ_H at fixed $\alpha = \pi/4$ with effective couplings $\kappa_{VV}^{h^0}$, $\kappa_{VV}^{H^0}$, $\kappa_{VV}^{H_5^0}$, and $\kappa_{WW}^{H_5^{++}}$. The purple dotted curve shows the GM sum–rule $(\kappa_{VV}^{h^0})^2 + (\kappa_{VV}^{H^0})^2 + (\kappa_{VV}^{H_5^0})^2 - (\kappa_{WW}^{H_5^{++}})^2$	47

Fig. 4.4	Septet effective couplings versus θ_7 at fixed $\alpha = \pi/4$: $\kappa_{VV}^{h^0}$, $\kappa_{VV}^{H^0}$, and $\kappa_{WW}^{H^{++}}$. The red dotted curve shows the Septet sum-rule $(\kappa_{VV}^h)^2 + (\kappa_{VV}^H)^2 - (\kappa_{WW}^{H^{++}})^2$	48
Fig. 4.5	2HDM heat map in (β, α)	50
Fig. 4.6	GM heat map in the (θ_H, α) plane with the same 2σ and best-fit conventions as mentioned in the caption of Fig. 4.5.	51
Fig. 4.7	Septet heat map in the (θ_7, α) plane with the same 2σ and best-fit conventions as in Fig. 4.5.	51
Fig. 4.8	2HDM: Heatmap for $\kappa_V^{H^0}(\beta, \alpha)$	52
Fig. 4.9	GM: Heatmap for $\kappa_{VV}^{H^0}(\theta_H, \alpha)$	52
Fig. 4.10	Septet: Heatmap for $\kappa_V^{H^0}(\theta_7, \alpha)$	53
Fig. 4.11	Doubly charged effective-coupling maps constrained by the 2σ $\kappa_V^{h^0}$ constrained by $0.86 \leq \kappa_V^{h^0} \leq 1.18$	54
Fig. 5.1	The panel depicts $(\sigma \times BR)_{\text{theory}}$ versus $\kappa_V^{H^0}$ for the 2HDM, GM and Septet model. The colour of the markers are obtained from the most-sensitive channel.	60
Fig. 5.2	Channel-wise panels with allowed points coloured by model for the most sensitive channels with broad mass coverage: inclusive $H \rightarrow WW, ZZ$, combined $\tau\tau$ ($ggH+bbH$), $VBF \rightarrow WW, ZZ$, $ggH \rightarrow ZZ$, inclusive $H \rightarrow ZZ$, and $\gamma\gamma$. These panels let us directly compare which cross sections remain viable in each channel across the three models, which can be compared to confirm the channel specific ranges, as discussed in Appendix G.	61
Fig. 5.3	Channel-wise panels with allowed points coloured by model. This figure groups channels with sparse mass coverage or smaller samples (e.g. $vbfH \rightarrow b\bar{b}$, $ggH \rightarrow t\bar{t}$, $ggH, vbfH, WH, ZH \rightarrow WW$).	62
Fig. 5.4	Allowed ranges of $\kappa_V^{H^0}$ as a function of m_{H^0} for the three models. Solid (dashed) curves are the per-mass maxima (minima) over all allowed points. The edges at a given mass can be set by different channels; see the channel coded heatmaps for channel specific $\kappa_V^{H^0}$ vs m_{H^0} in Appendix G.2.1.	63
Fig. 5.5	2HDM mass panel overlays in the (β, α) plane, with a $\kappa_V^{H^0}$ heatmap as the background and the color-coded regions are most-sensitive channel from the HiggsBounds result.	64
Fig. 5.6	GM mass panel overlays in the (θ_H, α) plane, with a $\kappa_V^{H^0}$ heatmap as the background and the color-coded regions are most-sensitive channel from the HiggsBounds result.	65
Fig. 5.7	Septet mass panel overlays in the (θ_7, α) plane, with a $\kappa_V^{H^0}$ heatmap as the background and the color-coded regions are most-sensitive channel from the HiggsBounds result.	66
Fig. A.1	Allowed region for partial wave amplitudes a_ℓ in the complex plane.	73

Fig. F.1	Effective couplings κ_V versus mixing angles for several fixed α values. Solid (dashed) lines show the h^0 (H^0) couplings in each model.	84
Fig. G.1	Comparison to CMS $ggH \rightarrow \tau\tau$ limits (138 fb^{-1}) [41]. Top: our overlay with observed/expected curves from the HiggsTools dataset and allowed points coloured by $\kappa_V^{H^0}$. Bottom: the corresponding CMS summary panel (units as in the original paper).	85
Fig. G.2	Comparison to ATLAS $H \rightarrow ZZ$ limits with ggH and VBF categories (139 fb^{-1}) [36]. Right: our overlay (pb); left/bottom: ATLAS reference panel (fb).	86
Fig. G.3	Overlay for a high-mass $H^0 \rightarrow ZZ$ comparison using the HiggsTools entry mapped to Ref. [45]. The ATLAS panel (bottom) is shown for visual scale (fb); the overlay (top right) is in pb.	86
Fig. G.4	Comparison to ATLAS $ggH \rightarrow \tau\tau$ limits (139 fb^{-1}) [39]. Top right: our overlay; bottom: ATLAS reference figure.	87
Fig. G.5	Comparison to CMS VBF $H \rightarrow ZZ$ limits (35.9 fb^{-1}) [42]. Right: our overlay in pb; left/bottom: CMS panel as published.	87
Fig. G.6	Comparison to ATLAS VBF $\gamma\gamma$ limits at 8 TeV [43]. Our overlay uses the HiggsTools entry for this analysis (top right); the ATLAS panel (bottom) is reproduced for context (fb).	88
Fig. G.7	Envelope of $(\sigma \times \text{BR})$ values over the <u>most sensitive</u> analysis at each point, shown versus m_{H^0} for the three benchmark models. Shaded bands indicate the range spanned by excluded points after the filters of Sec. 5.3. Note that while the bands appear continuous, our scan used a mass step of $\Delta m = 20 \text{ GeV}$; the bands are a visual aid.	89
Fig. G.8	Most-sensitive channel across the $(m_{H^0}, \kappa_V^{H^0})$ plane for the three models. Each pixel indicates the production–decay topology that provides the most sensitive channel in that region. We also indicate the obsRatio of each bin.	90

List of Tables

Tab. 1.1	Comparison of Hypercharge and Isospin for 2HDM, GM, and Septet models.	8
Tab. 2.1	2HDM Model: Effective Higgs-gauge boson couplings	20
Tab. 2.2	Effective couplings of GM Higgs states to gauge bosons in terms of mixing angles s_H , c_H , and α	28
Tab. 2.3	Effective couplings of septet Higgs states to gauge bosons.	32

Tab. 4.1	Model comparison for field content and vev structure for the 2HDM, GM, and Septet models.	44
Tab. 4.2	Effective Higgs–vector–boson couplings grouped by model. Here $V = W, Z$	45
Tab. 4.3	Mixing angle set for all heatmaps as a grids in $(\alpha, \beta / \theta_H / \theta_7)$	49
Tab. 4.4	2σ effective–coupling intervals derived from the CMS band on $\kappa_V^{h^0}$ [20].	55
Tab. 5.1	Model-wise ranges for the effective coupling $\kappa_V^{H^0}$. The “scan range” is the input interval used to generate points. The “updated range” is inferred from the allowed points in the figures above.	63
Tab. 5.2	Channel-wise ($\sigma \times \text{BR}$) ranges for the HB-selected analysis for the allowed points (sec. 5.3). A uniform floor of 10^{-6} pb is applied to the lower bound of ($\sigma \times \text{BR}$) to match the plotting convention. The last column lists representative references used in the HiggsTools dataset for each channel.	68
Tab. D.1	Effective couplings $\kappa_{VV}^{h_i}$ of scalar bosons to pairs of electroweak vector bosons in the GM model.	78
Tab. D.2	Effective couplings κ for Higgs–Higgs–Vector boson vertices in the GM model.	78

1. Introduction and Motivation

The Standard Model (SM) of particle physics [1, 2] successfully describes electromagnetic, weak, and strong interactions through a gauge invariant quantum field theory framework. A key missing piece of this theory, Higgs boson, was discovered in 2012 at the Large Hadron Collider (LHC) [3, 4], consistent with the Higgs mechanism as the source of electroweak symmetry breaking (EWSB). The mechanism through which the W^\pm , Z bosons attain their masses is called the Brout–Englert–Higgs (BEH) mechanism [5].

Despite many successes, the SM has some well-known limitations. For example, it does not describe the small non-zero neutrino masses, the observed matter–antimatter asymmetry of the universe, or the existence of dark matter. Additionally, it faces theoretical problems such as the hierarchy problem, where we observe the instability of the Higgs boson mass with respect to quantum corrections. These limitations suggest that the SM is only an effective theory, valid up to a certain energy scale, beyond which new physics may appear [6].

One well-motivated research area for extending the SM is through the **extended Higgs sectors**, which can provide solutions to some of these open problems. For example, the Two-Higgs Doublet Model (2HDM) can enable a strong first-order electroweak phase transition and introduce new sources of CP violation, both necessary ingredients for successful electroweak baryogenesis [7].

This thesis focuses on three such models:

The Two-Higgs Doublet Model (2HDM) [8, 9, 10, 11] introduces a second $SU(2)_L$ doublet, enriching the scalar spectrum and enabling modified Higgs couplings.

The Georgi-Machacek (GM) model [12, 13, 14, 15] adds real and complex triplets preserving custodial symmetry and introducing singly and doubly charged Higgs bosons, which provides us with rich structures in our BSM models.

The Scalar Septet Model [16, 17, 18] includes a higher-isospin $SU(2)_L$ septet field, also including higher charged fields.

An interesting fact about all three models under our study, is that they all preserve custodial symmetry [19], with $\rho = 1$ at tree level. We exploit this fact in our analysis for deriving sum rules for high-energy vector boson scattering processes. We will discuss the ρ parameter in more detail in **section 2.1**.

In this thesis, we perform a comparative analysis of the phenomenological implications of these extended Higgs sectors. We focus on the *coupling structure* of the scalar fields, deriving sum rules that follow from perturbative unitarity in longitudinal vector boson scattering. We utilized *theoretical constraints*, such as unitarity, to obtain theoretical limits on mass bounds for heavy Higgs states in our models. We also explored *experimental bounds* [20] on masses and couplings from the collider data. The goal of the thesis is to evaluate how each model compares under current experimental precision, and to highlight distinctive features that could be probed at the LHC or future colliders.

1.1. Structure of the Thesis

This thesis develops extended Higgs-sector models from first principles, derives their unitarity sum rules, and confronts the resulting parameter spaces with collider data using `HiggsTools`. The material is organized as follows.

Chapter 1 — Introduction and Motivation. We review the Standard Model with emphasis on electroweak symmetry breaking and the Higgs mechanism, then introduce the theoretical consistency requirements used throughout the thesis. In particular, we discuss the ρ parameter, tree-level perturbative unitarity and sum rules, and the role of Higgs-vector-boson couplings, followed by the tree-level contributions to high-energy $W^+W^- \rightarrow W^+W^-$ scattering. The chapter closes with a brief outline of the thesis structure.

Chapter 2 — Extended Higgs Sector Models. We define the three custodial-symmetry preserved models studied in this work: the Two-Higgs-Doublet Model (2HDM), the Georgi-Machacek (GM) model, and a scalar Septet extension. For each model we present the field content, scalar potentials, vacuum structure, mass matrices, and gauge interactions, and we collect the tree-level Higgs couplings to vector bosons that are used later in the unitarity and collider analyses.

Chapter 3 — Higgs and Vector-Boson Scattering Unitarity Sum Rules. We derive and compare the high-energy cancellations that enforce perturbative unitarity in the three models. After presenting the model-specific $VV \rightarrow VV$ amplitudes, we extract theoretical mass bounds implied by the sum rules for each extended model. These bounds provide the theoretical baseline against which collider limits are interpreted in later chapters.

Chapter 4 — Comparative Analysis and Experimental Limits. We first summarise the three models side-by-side: comparing their field content and spectra, VEV structure and mixing angles, and the resulting effective couplings and sum rules. We then refer and mention the experimental landscape relevant to additional Higgs states and translate the 2σ bounds on the SM-like Higgs coupling $\kappa_V^{h^0}$ into constraints on mixing parameters and on the heavy Higgs couplings $\kappa_V^{H^0}$. The chapter includes heat maps for $\kappa_V^{h^0}$, derived limits for $\kappa_V^{H^0}$ and (where applicable) $\kappa_{WW}^{H^{++}}$, and tabulated 2σ coupling intervals that are used as inputs to the `HiggsTools` study.

Chapter 5 — `HiggsTools` Framework and Analysis Strategy. We describe the exclusion logic (observed/expected ratios), the parameter scan, post-processing filters, and the visualization strategy. We focus on $\sigma \times \text{BR}$ (computed by the `HiggsTools`), $\kappa_V^{H^0}$ and the mass of the heavy Higgs boson m_{H^0} . Using these parameters we make scatter and line plots which we analyze to obtain exclusion and allowed ranges on the same. We also compare the model predictions ($\sigma \times \text{BR}$)_{theory} with the observed/expected 95% CL limits from the underlying papers referenced by `HiggsBounds`, see Appendix G. We find exclusion channels which tighten the allowed ranges of the effective couplings compared to those we had derived analytically from the three models using the 2σ bounds [20].

Chapter 6 — Summary and Future Prospects. This chapter summarizes the entire thesis, including the theoretical and experimental analysis for the BSM models, along with the final results obtained

from the `HiggsTools` analysis.

Appendices The Appendices collect derivations and supporting plots used in the main text which supports the thesis work for completeness.

This structure moves from theory to phenomenology in a consistent way: Chapters 2-3 defines the BSM models and unitarity sum rules; Chapter 4 aligns them with existing coupling measurements and experimental limits; Chapter 5 performs the `HiggsTools` analysis and provides the consolidated interpretation.

1.2. The Standard Model of Particle Physics

The SM is a gauge theory describing all known fundamental particles and their interactions, excluding gravity. The fundamental particles are categorized into fermions, which are the matter particles, and bosons, which are the force carriers. The full gauge group that describes the SM is given by [2]:

$$SU(3)_c \times SU(2)_L \times U(1)_Y,$$

where $SU(3)_c$ describes the strong interaction mediated by gluons and associated with color charge, and $SU(2)_L \times U(1)_Y$ describes the electroweak interaction, mediated by W , Z , and the photon. The matter particles of the SM consists of three generations of fermions, divided into quarks and leptons. These are represented by chiral fields, with hypercharge defined as $Y = 2(Q - T^3)$, where Q is the electric charge and T^3 is the third component of weak isospin.

The SM Electroweak Lagrangian describes the interaction between the gauge bosons, fermions, and the Higgs. [2]:

$$\mathcal{L} = \sum_{\text{fermions}} (i\bar{\psi}\gamma^\mu D_\mu \psi + Y_f \bar{\psi}_L \phi \psi_R + \text{h.c.}) - \sum_{\text{gauge bosons}} \left(\frac{1}{4} F_{\mu\nu}^a F^{a,\mu\nu} \right) + |D_\mu \Phi|^2 - V(\Phi). \quad (1.1)$$

Here, ψ denotes fermionic fields, Φ is the $SU(2)_L$ complex scalar doublet, and $F_{\mu\nu}^a$ is the electromagnetic non-Abelian field strength tensor:

$$F_{\mu\nu}^a = \partial_\mu A_\nu^a - \partial_\nu A_\mu^a + g f^{abc} A_\mu^b A_\nu^c, \quad (1.2)$$

where A_μ^a are the gauge fields and f^{abc} the structure constants.

The covariant derivative is given by:

$$D_\mu = \partial_\mu - ig \frac{\sigma_a}{2} W_\mu^a - ig' \frac{Y}{2} B_\mu. \quad (1.3)$$

with g and g' being the $SU(2)_L$ and $U(1)_Y$ coupling constants respectively and σ_a correspond to the

Pauli matrices¹ and W_μ^a and B_μ are the $SU(2)_L$ and $U(1)_Y$ gauge fields respectively. [1].

1.2.1. Electroweak Symmetry Breaking and Higgs Mechanism

Before symmetry breaking, the gauge bosons are massless and to explain the massive gauge bosons (W^\pm and Z), the BEH (Higgs) mechanism introduces a $SU(2)_L$ Higgs doublet which is given by [11]:

$$\Phi = \begin{pmatrix} \phi^+ \\ \phi^0 \end{pmatrix}. \quad (1.4)$$

This doublet is used to construct the scalar sector of SM which is described by the Higgs mechanism. The Higgs field is subject to a potential that is symmetric under gauge transformations, but its ground state does not respect this symmetry. This phenomenon is known as spontaneous symmetry breaking (SSB) [21]. In the SM, after spontaneous symmetry breaking (SSB), this is realized when the Higgs field acquires a non-zero vacuum expectation value (VEV), breaking the electroweak gauge group as:

$$SU(2)_L \times U(1)_Y \rightarrow U(1)_{EM}. \quad (23)$$

This mechanism provides masses to the W^\pm and Z bosons, while leaving the photon massless. To study the field content after symmetry breaking, the scalar doublet ϕ can be conveniently rewritten as [22]:

$$\phi(x) = \frac{1}{\sqrt{2}} e^{i\chi(x)/v} \begin{pmatrix} 0 \\ v + H(x) \end{pmatrix}, \quad (10)$$

where $\chi(x)$ and $H(x)$ are real scalar fields with zero VEVs. The field $H(x)$ represents the physical Higgs boson, while $\chi(x)$ is the would-be Goldstone boson.

Goldstone's theorem states that for every spontaneously broken continuous global symmetry, there exists a massless scalar boson. In gauge theories like the SM, these Goldstone bosons are not physical, rather they are "eaten" by the gauge bosons, supplying the longitudinal degree of freedom needed to make them massive. In unitary gauge, the $\chi(x)$ field disappears entirely, leaving only the observable Higgs excitation $H(x)$ [22].

The full scalar Higgs Lagrangian is:

$$\mathcal{L}_{\text{scalar}} = |D_\mu \Phi|^2 - V(\Phi), \quad (1.5)$$

where the SM Higgs potential $V(\Phi)$ is given by:

$$V(\Phi) = \mu^2 \Phi^\dagger \Phi + \lambda (\Phi^\dagger \Phi)^2. \quad (1.6)$$

¹The three Pauli matrices are: $\sigma_x = \begin{pmatrix} 0 & 1 \\ 1 & 0 \end{pmatrix}$, $\sigma_y = \begin{pmatrix} 0 & -i \\ i & 0 \end{pmatrix}$, and $\sigma_z = \begin{pmatrix} 1 & 0 \\ 0 & -1 \end{pmatrix}$.

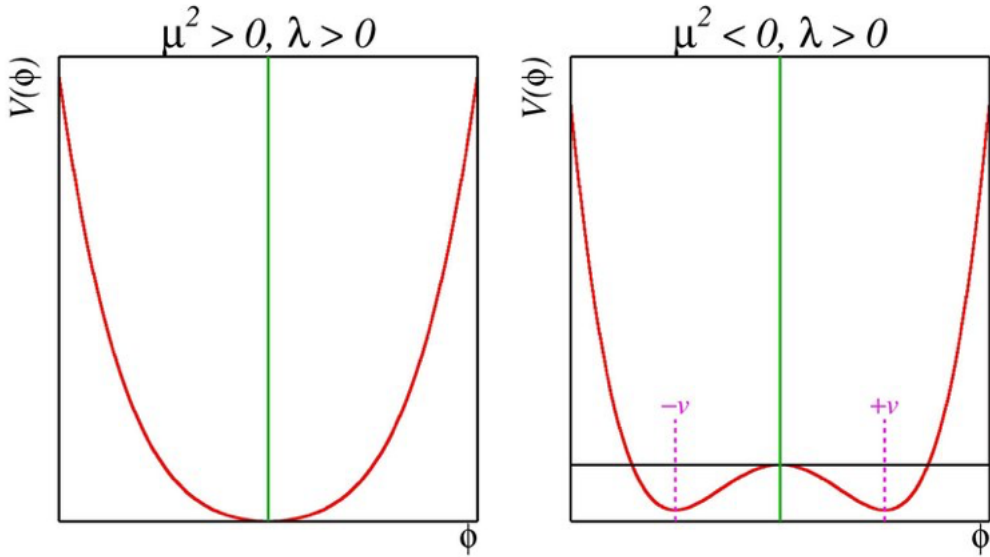


Figure 1.1.: Left: Higgs potential for $\mu^2 > 0$, no spontaneous symmetry breaking. Right: Higgs potential for $\mu^2 < 0$, allowing spontaneous symmetry breaking and a non-zero vacuum expectation value at $\pm v$ [23].

As we can see in 1.1, for spontaneous symmetry breaking, $\mu^2 < 0$, leading to the vacuum expectation value, vev:

$$\langle \Phi \rangle = \frac{1}{\sqrt{2}} \begin{pmatrix} 0 \\ v \end{pmatrix}, \quad \text{with } |v|^2 = -\frac{\mu^2}{\lambda}. \quad (1.7)$$

Expanding the field around the vacuum:

$$\Phi = \frac{1}{\sqrt{2}} \begin{pmatrix} 0 \\ v + H \end{pmatrix}, \quad (1.8)$$

leads to mass generation for W and Z bosons while the vector bosons interact with the Higgs field:

$$M_{W^\pm} = \frac{gv}{2}, \quad M_Z = \frac{v\sqrt{g^2 + g'^2}}{2}. \quad (1.9)$$

And the resulting couplings for the interaction between gauge boson and Higgs are given as

$$g_{hW^+W^-} = \frac{2M_W^2}{v}, \quad g_{hZZ} = \frac{2M_Z^2}{v}, \quad (1.10)$$

where h refers to the SM Higgs boson, with mass $m_h = 125.35 \pm 0.15$ GeV.

The weak mixing angle θ_W is defined by [11]:

$$\cos \theta_W = \frac{g}{\sqrt{g^2 + g'^2}} = \frac{M_W}{M_Z}, \quad (1.11)$$

which yields the ρ parameter:

$$\rho = \frac{M_W^2}{M_Z^2 \cos^2 \theta_W} = 1, \quad (1.12)$$

consistent with electroweak symmetry to preserve custodial symmetry. Custodial symmetry is a global $SU(2)_C$ symmetry of the Higgs sector that protects the electroweak ρ parameter from large corrections, ensuring $\rho = 1$ at tree level [13].

1.2.2. Higgs Couplings to Gauge Bosons and Fermions

The Higgs coupling to vector bosons is obtained by expanding the kinetic term:

$$\mathcal{L} \supset (D_\mu \Phi)^\dagger (D^\mu \Phi), \quad (1.13)$$

resulting in the interactions of the Higgs field with the gauge bosons and fermions.

Fermions are grouped into chiral representations as left-handed doublet fermionic fields, with isospin $\pm \frac{1}{2}$ and right-handed singlet fields. For the first generation of fermions, the singlets and doublets are given by [11]:

$$U_R = u_R, \quad D_R = d_R, \quad L_R = e_R,$$

$$Q_L = \begin{pmatrix} u_L \\ d_L \end{pmatrix}, \quad L_L = \begin{pmatrix} v_{e,L} \\ e_L \end{pmatrix}. \quad (1.14)$$

The Yukawa interaction Lagrangian is given by:

$$\mathcal{L}_{\text{Yukawa}} = -\bar{Q}_L Y^u \tilde{\Phi} u_R - \bar{Q}_L Y^d \Phi d_R - \bar{L}_L Y^l \Phi l_R + \text{h.c.}, \quad (1.15)$$

with $\tilde{\Phi} = i\sigma_2 \Phi^*$.

From the kinetic part of the Yukawa Lagrangian, we extract the fermion mass and the Higgs coupling:

$$m_f = \frac{v Y_f}{\sqrt{2}}, \quad (1.16)$$

$$g_{H f \bar{f}} = \frac{m_f}{v}. \quad (1.17)$$

Due to the absence of right-handed neutrinos in the SM, neutrinos do not acquire mass terms.

1.3. Constraints on Extended Higgs Model Theories

Perturbative unitarity is a theoretical constraint for testing the consistency of spontaneously broken gauge theories and to make sure that the model remains physically viable. Its most notable application was the 1977 derivation by Lee, Quigg, and Thacker [24] of a 1 TeV upper bound on the SM Higgs

mass, which influenced the design of the LHC and shaped expectations leading up to the Higgs discovery in 2012.

To ensure the viability of extended Higgs sectors, models must satisfy both theoretical and experimental constraints. This includes maintaining perturbative unitarity and complying with electroweak precision observables such as the ρ parameter, which are central to the analysis presented here.

1.3.1. The ρ Parameter

The parameter ρ is a dimensionless quantity defined as:

$$\rho = \frac{M_W^2}{M_Z^2 \cos^2 \theta_W}, \quad (1.18)$$

where M_W and M_Z are the masses of the W and Z bosons, respectively, and θ_W is the weak mixing angle. In the SM, the preservation of this ratio, when calculated at the tree level, is evaluated as $\rho = 1$.

Experimentally, the value of the ρ parameter is measured with high precision. According to [1],

$$\rho_{\text{exp}} = 1.00040 \pm 0.00024. \quad (1.19)$$

In extended Higgs sectors, the general expression for ρ is modified due to the presence of multiple scalar multiplets with arbitrary weak isospin I_i , hypercharge Y_i , and vacuum expectation values (VEVs) v_i . The general form in relation to Y_i, I_i, v_i is given by [11]:

$$\rho = \frac{\sum_{i=1}^n v_i^2 [4I_i(I_i + 1) - Y_i^2]}{\sum_{i=1}^n 2Y_i^2 v_i^2}. \quad (1.20)$$

For the SM Higgs doublet ($I = \frac{1}{2}$, $Y = 1$), this reduces to:

$$\rho_{\text{SM}} = \frac{M_W^2}{M_Z^2 \cos^2 \theta_W} = 1. \quad (1.21)$$

This observation highlights that while the SM naturally satisfies $\rho = 1$, this condition can also be met in extended models provided the vev structure and representation content are carefully chosen.

In particular, custodial symmetry plays a crucial role in maintaining this relation. Custodial symmetry preserves the global $SU(2)_L \times SU(2)_R \rightarrow SU(2)_C$ symmetry breaking pattern and thereby ensures that $\rho = 1$.

Exploiting $\rho = 1$ and using Eq. (1.20), we obtain the hypercharge and isospin combination that preserves the parameter. We therefore chose extended scalar sector models for analysis, which indeed preserve the value of the ρ parameter. This is an important fact, as this ensures the consistency of the important experimental constraint when we study and compare our models with collider data [13]. For instance, models composed solely of singlets and doublets automatically preserve $\rho = 1$ [13],

while models with scalar triplets typically do not. The Georgi-Machacek (GM) and the Septet model are notable exceptions, as they specifically constructed to maintain $\rho = 1$ even with triplet and septet representations, by arranging the VEVs in a custodially symmetric way. In Table 1.1, we can see the combinations of hypercharge and isospin, which lead to custodially symmetric models.

Model	Hypercharge (Y)	Isospin (I)
2HDM	$Y = 1/2$	$I = 1/2$
GM	$Y_D = 1/2$	$I_D = 1/2$
	$Y_{RT} = 0$	$I_T = 1$
	$Y_{CT} = 1$	
Septet	$Y = 2$	$I = 3$

Table 1.1.: Comparison of Hypercharge and Isospin for 2HDM, GM, and Septet models.

where for GM, we find the hypercharge(Y), Y_D = for doublet, Y_{RT} = for real triplet, Y_{CT} = for complex triplet, and isospin (I) I_D = for doublet, I_T = for triplets.

1.3.2. Unitarity Constraints and Sum Rules

A second class of theoretical constraints arises from unitarity considerations in high-energy scattering processes. In particular, the longitudinal scattering of vector bosons ($V_L V_L \rightarrow V_L V_L$, where $V = W^\pm, Z$) can exhibit amplitudes that grow indefinitely with center-of-mass energy if not properly regulated. Such behaviour violates unitarity and is not physically viable.

In the SM, this problematic growth is canceled by the inclusion of the Higgs boson in the s and t channel diagrams, a consequence of electroweak symmetry breaking. The Higgs coupling to vector bosons ensures the cancellation of these divergences at tree level, preserving unitarity. This will be discussed in more detail in the next section.

In extended Higgs models, analogous cancellations are required. These lead to algebraic relations among the couplings of the various Higgs states to vector bosons, known as the *sum rules*. These sum rules are not ad hoc constraints, but arise naturally from the model construction and ensure that the amplitudes remain bounded at high energies. This elimination of this bad high-energy behaviour ensures that the theory respects perturbative unitarity. This process will be discussed in detail for our extended Higgs models in 3.

Sum rules have profound phenomenological implications. They not only validate the theoretical structure of a given model, but also put constraints on the possible values of couplings and mass parameters.

Additionally, perturbative unitarity bounds are imposed by requiring that the partial wave amplitudes do not exceed unitary limits. The zeroth partial wave amplitude, a_0 , for scalar scattering processes, must satisfy [13]:

$$\text{Re}(a_0) \leq \frac{1}{2}. \quad (1.22)$$

In particular, the partial wave unitarity condition is used throughout this thesis to derive mass bounds

for heavy Higgs states in extended scalar sectors. A more detailed analysis is discussed in the Appendix A.

This leads to bounds on the scalar masses. For instance, in the SM, this implies:

$$m_h^2 \leq 4\pi v^2 \simeq (870 \text{ GeV})^2. \quad (1.23)$$

Such constraints are central in identifying phenomenologically viable parameter spaces for crucial parameters such as scalar masses, gauge couplings, and mixing angles. In this thesis, we systematically:

- derive and analyze the tree-level high-energy scattering amplitudes for longitudinal vector bosons in each model (2HDM, GM, Septet);
- extract coupling sum rules for Higgs–vector boson interactions that ensure cancellation of bad high-energy behavior, preserving perturbative unitarity;
- apply perturbative unitarity bounds to constrain the mass of heavy scalar states from the sum rule structure and partial wave unitarity limits;
- perform a comparative analysis of the coupling structures, sum rules, and scalar mass bounds across 2HDM, GM, and Septet models;
- constrain the mixing angles and heavy scalar masses in each model using the latest experimental limits on Higgs coupling modifiers (κ_V), as obtained from [20];
- incorporate these κ_V bounds to obtain indirect but model-specific constraints on scalar sector parameters, especially for CP-even and charged Higgs bosons;
- use the `HiggsTools` software to incorporate collider-exclusion data and compare it with theoretically allowed regions, determining which CP-even heavy Higgs mass ranges are excluded or allowed and also obtain the effective coupling ranges for the same.

In the following chapters, we will systematically derive these constraints and apply them to each model under consideration. This provides a theoretical foundation upon which experimental analyses can be performed.

1.3.3. Higgs–Vector Boson Coupling and Unitarity Conservation in the SM

The unitarity of the SM is maintained through a delicate interplay between various scattering processes that contribute to longitudinal vector boson scattering, especially in processes such as $W_L^+ W_L^- \rightarrow W_L^+ W_L^-$. These amplitudes, without the Higgs boson contributions, grow rapidly with center-of-mass energy and would ultimately violate perturbative unitarity at high energies. The cancellation of this bad energy behavior can be attributed to the gauge and Higgs boson contributions and the structure of

the gauge theory. A more comprehensive analysis can be found in [13], where perturbative unitarity in SM is discussed in detail, as well as the models under our investigation.

1.4. Tree-Level Contributions to $W^+W^- \rightarrow W^+W^-$

Higgs-Mediated Vector Boson Scattering in the SM

The process $W_L^+W_L^- \rightarrow W_L^+W_L^-$ plays a central role in testing perturbative unitarity in the SM. At the tree-level, the total amplitude receives contributions from:

- The 4-point contact interaction from the non-Abelian gauge structure.
- s - and t -channel exchange of neutral gauge bosons (Z, γ).
- s - and t -channel Higgs boson exchange.

Each of these contributes terms that scale with energy (E^2) or (E^4), and, unless carefully canceled, would violate unitarity. This will be discussed in detail in the following sections.

Kinematics and Polarization Vectors

Let the four-momenta of the initial and final W bosons in the center-of-mass frame be:

$$\begin{aligned} p_+ &= (E, 0, 0, p), & p_- &= (E, 0, 0, -p), \\ k_+ &= (E, p \sin \theta, 0, p \cos \theta), & k_- &= (E, -p \sin \theta, 0, -p \cos \theta), \end{aligned} \tag{1.24}$$

where $E \gg M_W$ in the high-energy limit, and $p = \sqrt{E^2 - M_W^2}$.

Then, the longitudinal polarization vectors of the external W bosons are:

$$\begin{aligned} \epsilon_L(p_+) &= \left(\frac{p}{M_W}, 0, 0, \frac{E}{M_W} \right), & \epsilon_L(p_-) &= \left(\frac{p}{M_W}, 0, 0, -\frac{E}{M_W} \right), \\ \epsilon_L(k_+) &= \left(\frac{p}{M_W}, \frac{E}{M_W} \sin \theta, 0, \frac{E}{M_W} \cos \theta \right), & \epsilon_L(k_-) &= \left(\frac{p}{M_W}, -\frac{E}{M_W} \sin \theta, 0, -\frac{E}{M_W} \cos \theta \right). \end{aligned} \tag{1.25}$$

These satisfy $\epsilon_L(p_i) \cdot p_i = 0$ and $\epsilon_L(p_i)^2 = -1$ as required by the Lorentz invariance.

4-Point Gauge Vertex Contribution

The Feynman rule for the quartic gauge interaction gives:

$$\mathcal{M}_{4\text{pt}} = -ig^2 (2g_{\mu\sigma}g_{\nu\rho} - g_{\mu\nu}g_{\rho\sigma} - g_{\mu\rho}g_{\nu\sigma}) \epsilon_1^\mu \epsilon_2^\nu \epsilon_3^{*\rho} \epsilon_4^{*\sigma}. \tag{1.26}$$

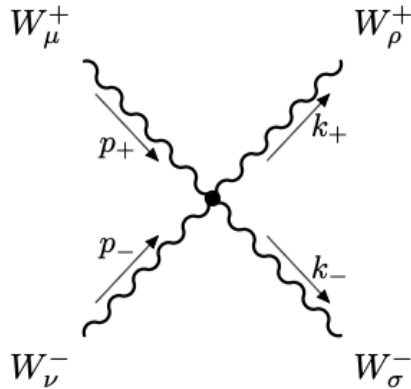


Figure 1.2.: Feynman diagram for the 4-point vector-boson scattering at tree level, arising from the non-Abelian structure of the $SU(2)_L$ gauge group.

Using the high-energy polarization vectors, the amplitude grows as:

$$\mathcal{M}_{\text{4pt}} \sim i \frac{g^2 E^4}{M_W^4} [\dots], \quad (1.27)$$

which indicates unitarity violation unless cancelled.

Gauge Boson Exchange Contributions

The Figure 1.3 corresponds to the Feynman diagrams with gauge boson propagators. From the s - and t -channel diagrams with gauge (Z and γ) bosons, we have the propagators:

$$\frac{-ig_{\mu\nu}}{q^2}, \quad \text{and} \quad \frac{-i}{q^2 - M_Z^2} \left(g_{\mu\nu} - \frac{q_\mu q_\nu}{M_Z^2} \right). \quad (1.28)$$

The Feynman Rules for the vertex of the gauge boson mediated propagators is given by:

$$i \left\{ \frac{e}{g \cos \theta_W} \right\} [g_{\mu\nu}(-p_- + p_+)\alpha + g_{\mu\alpha}(q + p_+)\nu + g_{\nu\alpha}(-q - p_-)\mu], \quad (17)$$

Here, e is the electromagnetic coupling constant, g is the weak $SU(2)$ gauge coupling, and θ_W is the Weinberg angle. Their contribution partially cancels the $\mathcal{O}(E^4)$ behavior, but a residual $\mathcal{O}(E^2)$ term remains:

$$\mathcal{M}_{\text{gauge}} \approx i \frac{g^2}{4M_W^2} (s + t + \mathcal{O}(M_W^2)) \sim \mathcal{O}(E^2). \quad (1.29)$$

where s and t denote the Mandelstam variables corresponding to the center-of-mass energy and the squared momentum transfers in the scattering process.

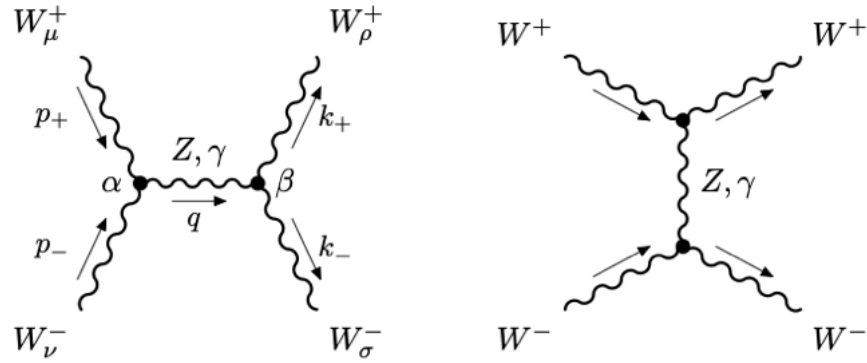


Figure 1.3.: **Gauge boson exchange diagrams** (Z , γ) in the s - and t -channels contributing to $W^+W^- \rightarrow W^+W^-$ scattering. These diagrams partially cancel the high-energy growth from the 4-point vertex.

SM Higgs boson Exchange

We now include the s - and t -channel diagrams involving SM Higgs boson exchange. The Figure 1.3 corresponds to the Feynman diagrams which are mediated by the Higgs boson. These contribute via the interaction term:

$$\mathcal{L}_{HWW} = g_{HWW} HW_\mu^+ W^{-\mu} \quad \text{with} \quad g_{HWW} = \frac{2M_W^2}{v}. \quad (1.30)$$

The Feynman rule for the vertex is:

$$\frac{2iM_W^2}{v} g_{\mu\nu} = i \frac{g^2 v}{2} g_{\mu\nu}. \quad (1.31)$$

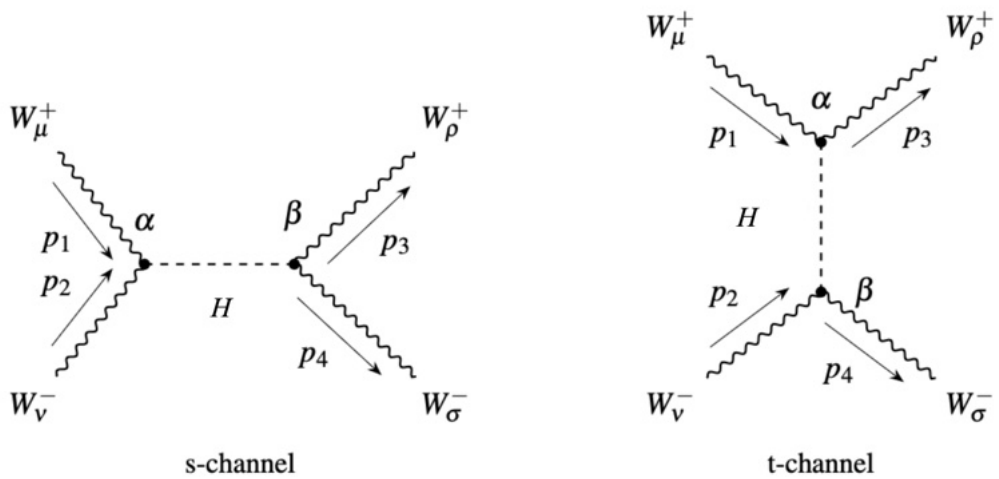


Figure 1.4.: **Higgs boson exchange diagrams** in the s - and t -channels contributing to $W^+W^- \rightarrow W^+W^-$ scattering. The Higgs diagrams cancel the residual high-energy growth from the gauge sector, restoring unitarity.

Calculating the s - and t -channel Higgs exchange diagrams yields:

$$\mathcal{M}_{\text{Higgs}} = -i \frac{1}{v^2} \left(\frac{s^2}{s - m_h^2} + \frac{t^2}{t - m_h^2} \right), \quad (1.32)$$

where m_h is the Higgs mass, and the s^2 and t^2 numerators originate from contractions of the longitudinal W -boson polarization vectors through the $g_{\mu\nu}$ vertex factors.

In the high-energy limit, where $s, t \gg m_h^2$, we expand the denominators and find:

$$\mathcal{M}_{\text{Higgs}} \simeq -i \frac{1}{v^2} (s + t + 2m_h^2 + \dots). \quad (1.33)$$

Hence, we observe that the $\mathcal{O}(E^2)$ terms cancel exactly:

$$\mathcal{M}_{\text{total}} = \mathcal{M}_{\text{4pt}} + \mathcal{M}_{\text{gauge}} + \mathcal{M}_{\text{Higgs}} \simeq -i \frac{1}{v^2} (2m_h^2). \quad (1.34)$$

This cancellation ensures that the total amplitude no longer grows with energy. The residual constant term is of the order $\mathcal{O}(g^2)$ and remains finite in the high-energy limit [11]. We shall exploit this cancellation of the $(s+t)$ contribution to derive sum rules for our extended Higgs model. This will also ensure that our BSM models are unitarily sound.

Higgs Mass Bound from Perturbative Unitarity

For any $2 \rightarrow 2$ scattering process in quantum field theory, when the center-of-mass energy E_{COM} is much larger than the masses of the particles involved, the scattering amplitude \mathcal{M} can be expressed using a partial wave expansion² [14]:

$$\mathcal{M} = 16\pi \sum_{l=0}^{\infty} (2l+1) a_l(|\vec{p}|) P_l(\cos \theta), \quad (1.35)$$

where a_l are the partial wave amplitudes for the partial wave l^{th} , and $P_l(\cos \theta)$ are the Legendre polynomials.

In leading order, the dominant contribution typically comes from the s -wave ($l = 0$), simplifying the amplitude to:

$$\mathcal{M} = 16\pi a_0 + \dots. \quad (1.36)$$

In order to ensure unitarity (conservation of probability), the partial wave amplitudes are constrained by the following bounds:

$$|a_l| \leq 1; \quad |\text{Re}(a_l)| \leq \frac{1}{2}; \quad 0 \leq |\text{Im}(a_l)| \leq 1. \quad (1.37)$$

²Refer to Appendix A for more details.

At tree level, the a_l are real, and hence we apply the constraint:

$$|\text{Re}(a_0)| \leq \frac{1}{2}$$

as the primary unitarity condition on our scattering amplitudes.

Using 1.34 the finite remainder of the amplitude can be equated to the amplitude given in Equation 1.4 using the $l = 0$ partial wave expansion [13]:

$$\mathcal{M} \simeq -\frac{1}{v^2}(2m_h^2) = 16\pi a_0 \quad \Rightarrow \quad a_0 \simeq -\frac{1}{16\pi v^2}(2m_h^2). \quad (1.38)$$

Applying the unitarity constraint: $|\text{Re } a_0| \leq \frac{1}{2}$, we obtain the upper bound on the Higgs boson mass:

$$m_h^2 \leq 4\pi v^2 \quad \Rightarrow \quad m_h \leq \sqrt{4\pi} v \approx 870 \text{ GeV}. \quad (1.39)$$

Thus, perturbative unitarity places a theoretical limit on the Higgs mass, derived purely from tree-level considerations of the zeroth partial wave amplitude in $W_L^+W_L^-$ scattering [13]. We shall use the perturbative unitarity scheme to extract theoretical mass limits for our extended Higgs models and then get experimental estimates from the same.

2. Extended Higgs Sector Models

Introduction

The SM, introduced in Chapter 1.2, describes electroweak symmetry breaking via a single Higgs doublet, successfully predicting a neutral scalar particle, the Higgs boson. However, as discussed earlier, this setup leaves several fundamental issues unresolved, including the hierarchy problem, the origin of dark matter, and the observed baryon asymmetry in the universe.

To explore possible solutions, this chapter focuses on extensions of the scalar sector. Although our analysis does not address any limitations of the SM directly, nevertheless, some solutions to the limitations of the SM have been proposed using the extended Higgs models investigated in the thesis. So, our motivation does not come directly from addressing such problems; rather, it is the ρ -parameter, which provides the basis for our extensions, as we discussed before. We examine the three following extended Higgs models: the Two Higgs Doublet Model (2HDM) [8, 9, 25, 6, 26, 19], the Georgi-Machacek (GM) model [14, 12, 13, 15, 27], and the scalar Septet model [17, 16]. Each introduces new scalar multiplets while maintaining gauge invariance and custodial symmetry. These models differ in their field content, vacuum structure, and nature of their scalar couplings to gauge bosons [8].

The chapter is structured into separate sections, each focusing on one model. For each case, we introduce the scalar potential and electroweak Lagrangian, and compute the couplings of the physical Higgs states to electroweak gauge bosons. These couplings form the basis for the calculations and analyses carried out in the following chapters.

The results obtained here feed directly into the next chapter, where we derive theoretical constraints, most notably the Higgs–gauge boson sum rules that emerge from high-energy vector boson scattering. These sum rules capture the core features of perturbative unitarity and allow us to test the internal consistency of the extended scalar sectors under study. In this work, we have used MATHEMATICA [28], (including FeynCalc [29], FeynArts [30], and SARAH [31]) to calculate the couplings from the kinetic Lagrangian, the matrix elements (which is derived in the next chapter) as well as the Feynman diagrams for the same [19].

2.1. Two Higgs Doublet Model (2HDM)

2.1.1. Motivation and Overview

The SM Higgs sector contains a single scalar $SU(2)_L$ doublet, which gives mass to the W and Z bosons and the fermions after spontaneous symmetry breaking. The Two Higgs Doublet Model (2HDM) is one of the simplest extensions of the SM scalar sector. It introduces an additional complex $SU(2)_L$ doublet, increasing the number of scalar degrees of freedom. The phenomenology of the 2HDM is considerably richer: after EWSB, the physical spectrum contains five Higgs particles; two neutral CP-even scalars (h^0, H^0), one neutral CP-odd pseudoscalar (A^0), and a pair of charged Higgs bosons (H^\pm).

However, having two scalar doublets generally introduces flavor-changing neutral currents (FC-NCs) at tree level. To prevent these, a discrete \mathbb{Z}_2 symmetry is often imposed: $\Phi_1 \rightarrow \Phi_1$, $\Phi_2 \rightarrow -\Phi_2$. In this chapter, we study the CP-conserving 2HDM with a softly broken \mathbb{Z}_2 symmetry, where the symmetry-breaking term is of mass dimension two [13].

2.1.2. Scalar Field Content and Potential

We define the two complex scalar doublets as:

$$\Phi_1 = \begin{pmatrix} \phi_1^+ \\ \phi_1^0 \end{pmatrix}, \quad \Phi_2 = \begin{pmatrix} \phi_2^+ \\ \phi_2^0 \end{pmatrix}, \quad (2.1)$$

where each doublet has hypercharge $Y = +\frac{1}{2}$, as shown in Table 1.1. The most general CP-conserving and renormalizable scalar potential, respecting the \mathbb{Z}_2 symmetry up to a soft-breaking term, is given by:

$$\begin{aligned} V(\Phi_1, \Phi_2) = & m_{11}^2 (\Phi_1^\dagger \Phi_1) + m_{22}^2 (\Phi_2^\dagger \Phi_2) - m_{12}^2 [(\Phi_1^\dagger \Phi_2) + \text{h.c.}] \\ & + \frac{\lambda_1}{2} (\Phi_1^\dagger \Phi_1)^2 + \frac{\lambda_2}{2} (\Phi_2^\dagger \Phi_2)^2 + \lambda_3 (\Phi_1^\dagger \Phi_1)(\Phi_2^\dagger \Phi_2) \\ & + \lambda_4 (\Phi_1^\dagger \Phi_2)(\Phi_2^\dagger \Phi_1) + \frac{\lambda_5}{2} [(\Phi_1^\dagger \Phi_2)^2 + \text{h.c.}]. \end{aligned} \quad (2.2)$$

All parameters m_{ij} , $(i, j = 1, 2)$ and λ_i , $(i = 1, \dots, 5)$ are real. The parameters m_{12}^2 and λ_5 could be complex, but are real for a CP-conserving potential. The quartic couplings λ_i ($i = 1, \dots, 5$) are dimensionless, and m_{ij}^2 are mass parameters. It is common to define, $\lambda_{345} \equiv \lambda_3 + \lambda_4 + \lambda_5$. [8]

2.1.3. Spontaneous Symmetry Breaking and Field Decomposition

We assume that both doublets acquire vacuum expectation values (vevs) as:

$$\langle \Phi_1 \rangle = \begin{pmatrix} 0 \\ v_1/\sqrt{2} \end{pmatrix}, \quad \langle \Phi_2 \rangle = \begin{pmatrix} 0 \\ v_2/\sqrt{2} \end{pmatrix}, \quad (2.3)$$

where v_1 and v_2 are real and satisfy $v = \sqrt{v_1^2 + v_2^2} \approx 246$ GeV. We define the ratio of vevs as:

$$\tan \beta = \frac{v_2}{v_1}. \quad (2.4)$$

The parameterization is performed by the introduction of eight real fields ω_i^\pm , ρ_i , and η_i ($i = 1, 2$). The charged fields ω_i^\pm correspond to the upper components of the doublets, while the neutral components are decomposed into a vacuum expectation value v_i , a real CP-even field ρ_i , and a real CP-odd field η_i , as [13]:

$$\Phi_1 = \begin{pmatrix} \omega_1^+ \\ \frac{1}{\sqrt{2}}(v_1 + \rho_1 + i\eta_1) \end{pmatrix}, \quad \Phi_2 = \begin{pmatrix} \omega_2^+ \\ \frac{1}{\sqrt{2}}(v_2 + \rho_2 + i\eta_2) \end{pmatrix}. \quad (2.5)$$

These fields will later mix to form physical mass eigenstates, while the Goldstone bosons associated with electroweak symmetry breaking are identified among the parts of the ω_i^\pm and η_i fields [8] depending on the parametrization of the fields.

2.1.4. Tadpole Conditions and Mass Matrices

Substituting the above decomposition into the potential, we identify linear terms in ρ_1 and ρ_2 . These terms must vanish for the vacuum to correspond to a true minimum. After electroweak symmetry breaking, the requirement that the vacuum corresponds to a true minimum of the scalar potential leads to the following minimization conditions on the vacuum expectation values (VEVs):

$$\left. \frac{\partial V_{2HDM}}{\partial \Phi_1} \right|_{\langle \Phi_1 \rangle, \langle \Phi_2 \rangle} = 0, \quad \left. \frac{\partial V_{2HDM}}{\partial \Phi_2} \right|_{\langle \Phi_1 \rangle, \langle \Phi_2 \rangle} = 0. \quad (2.6)$$

This yields the tadpole conditions, which we obtain from the above minimization conditions:

$$T_1 = m_{11}^2 v_1 - m_{12}^2 v_2 + \frac{\lambda_1}{2} v_1^3 + \frac{\lambda_{345}}{2} v_1 v_2^2 = 0, \quad (2.7)$$

$$T_2 = m_{22}^2 v_2 - m_{12}^2 v_1 + \frac{\lambda_2}{2} v_2^3 + \frac{\lambda_{345}}{2} v_2 v_1^2 = 0. \quad (2.8)$$

These equations allow us to express m_{11}^2 and m_{22}^2 as:

$$m_{11}^2 = m_{12}^2 \frac{v_2}{v_1} - \frac{\lambda_1}{2} v_1^2 - \frac{\lambda_{345}}{2} v_2^2, \quad (2.9)$$

$$m_{22}^2 = m_{12}^2 \frac{v_1}{v_2} - \frac{\lambda_2}{2} v_2^2 - \frac{\lambda_{345}}{2} v_1^2. \quad (2.10)$$

The mass terms for the CP-even, CP-odd, and charged Higgs fields arise from the second-order (quadratic) terms in the Higgs potential. This corresponds to isolating the bilinear contributions in the fields ρ , η , and ω^\pm after substituting the scalar doublets Φ_1 and Φ_2 into the potential. The resulting

bilinear form of the 2HDM potential can be written compactly as [8]:

$$V_{\text{bilinear}} = \frac{1}{2} \begin{pmatrix} \rho_1 & \rho_2 \end{pmatrix} M_\rho^2 \begin{pmatrix} \rho_1 \\ \rho_2 \end{pmatrix} + \frac{1}{2} \begin{pmatrix} \eta_1 & \eta_2 \end{pmatrix} M_\eta^2 \begin{pmatrix} \eta_1 \\ \eta_2 \end{pmatrix} + \frac{1}{2} \begin{pmatrix} \omega_1^+ & \omega_2^+ \end{pmatrix} M_\omega^2 \begin{pmatrix} \omega_1^- \\ \omega_2^- \end{pmatrix}. \quad (2.11)$$

The explicit forms of the mass matrices M_ρ^2 , M_η^2 , and M_ω^2 , along with the resulting tree-level scalar masses, which are explained in further detail in Appendix B.

2.1.5. Electroweak Lagrangian and Higgs Couplings

After EWSB, the scalar sector not only provides masses to the W and Z bosons but also introduces interaction terms between the Higgs and the gauge bosons. These interactions are derived from the kinetic part of the scalar Lagrangian:

$$\mathcal{L}_{\text{kin}} = (D_\mu \Phi_1)^\dagger (D^\mu \Phi_1) + (D_\mu \Phi_2)^\dagger (D^\mu \Phi_2), \quad (2.12)$$

where the covariant derivative is defined as

$$D_\mu = \partial_\mu - i \frac{g}{2} \sigma^a W_\mu^a - i \frac{g'}{2} Y B_\mu. \quad (2.13)$$

where, g and g' denote the gauge couplings of the $SU(2)_L$ and $U(1)_Y$ groups respectively. The σ^a are Pauli matrices and Y is the hypercharge. The gauge group breaks into $SU(2)_L \times U(1)_Y \rightarrow U(1)_{\text{em}}$ gives rise to the physical gauge bosons via the field redefinitions:

$$W^\pm = \frac{1}{\sqrt{2}} (W_\mu^1 \mp i W_\mu^2), \quad (2.14)$$

$$\begin{pmatrix} Z_\mu \\ A_\mu \end{pmatrix} = \begin{pmatrix} \cos \theta_W & -\sin \theta_W \\ \sin \theta_W & \cos \theta_W \end{pmatrix} \begin{pmatrix} W_\mu^3 \\ B_\mu \end{pmatrix}, \quad (2.15)$$

with θ_W the weak mixing angle, defined by $\tan \theta_W = g'/g$. This leads to the tree-level relations [8]:

$$M_W^2 = \frac{1}{4} g^2 v^2, \quad (2.16)$$

$$M_Z^2 = \frac{1}{4} (g^2 + g'^2) v^2, \quad (2.17)$$

$$M_\gamma^2 = 0, \quad (2.18)$$

and the ρ -parameter, which reflects custodial symmetry, takes the value, as we also saw in Equation 1.21

$$\rho = \frac{M_W^2}{M_Z^2 \cos^2 \theta_W} = 1. \quad (2.19)$$

2.1.6. Tree-Level Higgs Couplings to Gauge Bosons

To study Higgs-gauge boson interactions, we expand the covariant kinetic term in the Lagrangian around the vacuum. The resulting interaction terms depend on the mixing angles α (for the CP-even higgs states) and β , which is defined as:

$$\tan \beta = \frac{v_2}{v_1}. \quad (2.20)$$

The CP-even mass eigenstates h^0 and H^0 are related to the gauge basis via:

$$\rho_1 = H^0 \cos \alpha - h^0 \sin \alpha, \quad (2.21)$$

$$\rho_2 = H^0 \sin \alpha + h^0 \cos \alpha. \quad (2.22)$$

Similarly, for the CP-odd and charged states:

$$\eta_1 = G^0 \cos \beta - A^0 \sin \beta, \quad \omega_1^\pm = G^\pm \cos \beta - H^\pm \sin \beta, \quad (2.23)$$

$$\eta_2 = G^0 \sin \beta + A^0 \cos \beta, \quad \omega_2^\pm = G^\pm \sin \beta + H^\pm \cos \beta. \quad (2.24)$$

These replacement rules map the interaction (gauge) eigenstates to the physical fields, allowing us to compute the Higgs couplings [8].

Higgs Couplings for 2HDM

The CP-even tree-level couplings involving Higgs (h^0 and H^0) and gauge bosons are:

$$g_{h^0WW} = \frac{vg^2}{2} \sin(\beta - \alpha), \quad g_{H^0WW} = \frac{vg^2}{2} \cos(\beta - \alpha), \quad (2.25)$$

$$g_{h^0ZZ} = \frac{v(g^2 + g'^2)}{2} \sin(\beta - \alpha), \quad g_{H^0ZZ} = \frac{v(g^2 + g'^2)}{2} \cos(\beta - \alpha). \quad (2.26)$$

The effective (relative to SM) couplings of the CP-even Higgs bosons to vector bosons are given by:

$$\kappa_V^{h^0} = \sin(\beta - \alpha) = \frac{g_{h^0VV}}{g_{h_{\text{SM}}VV}}, \quad \kappa_V^{H^0} = \cos(\beta - \alpha) = \frac{g_{H^0VV}}{g_{h_{\text{SM}}VV}}, \quad (2.27)$$

where $\kappa_V^{h^i}$ represents the ratio $g_{h^iVV}/g_{h_{\text{SM}}VV}$ for $V = W, Z$ and $h^i = h^0, H^0$.

The CP-odd and charged couplings are given by:

$$g_{H^0H^+W^-} = \frac{g}{2} \cos(\beta - \alpha), \quad g_{h^0H^+W^-} = \frac{g}{2} \sin(\beta - \alpha), \quad (2.28)$$

$$g_{H^0A^0Z} = \frac{\sqrt{g^2 + g'^2}}{2} \cos(\beta - \alpha), \quad g_{h^0A^0Z} = \frac{\sqrt{g^2 + g'^2}}{2} \sin(\beta - \alpha). \quad (2.29)$$

Coupling	Effective Coupling $\kappa_V^{h^i}$
$\kappa_{W^+W^-}^{h^0}$	$\sin(\beta - \alpha)$
$\kappa_{W^+W^-}^{H^0}$	$\cos(\beta - \alpha)$
$\kappa_{ZZ}^{h^0}$	$\sin(\beta - \alpha)$
$\kappa_{ZZ}^{H^0}$	$\cos(\beta - \alpha)$

Table 2.1.: 2HDM Model: Effective Higgs-gauge boson couplings

From the above table, the effective couplings of the CP-even scalars to vector bosons in extended Higgs sectors satisfy the sum rule:

$$\begin{aligned} \left(\kappa_V^{h^0} \right)^2 + \left(\kappa_V^{H^0} \right)^2 &= 1, \\ \sin^2(\beta - \alpha) + \cos^2(\beta - \alpha) &= 1. \end{aligned} \tag{2.30}$$

These coupling structures are also vital for collider observables, such as production cross sections and branching ratios, and their deviations from SM expectations offer a powerful probe of extended Higgs sectors. Table 2.1 lists all the relevant effective couplings for the interactions between 2HDM higgs states and the vector boson (W^\pm and Z).

2.2. Georgi-Machacek Model (GM)

2.2.1. Motivation and Overview

The Georgi-Machacek (GM) model is an extension of the Standard Model (SM) scalar sector that includes additional scalar triplet fields while preserving custodial symmetry. In contrast to the 2HDM, which only adds an extra scalar doublet, the GM model introduces one real and one complex $SU(2)_L$ triplet, enabling a custodial symmetric scalar potential that allows sizable deviations in Higgs couplings to vector bosons without conflicting with electroweak precision observables [13].

This introductory chapter presents the structure of the GM model in detail. This sets the stage for the next chapter, where we will compute the theoretical sum rules governing the Higgs-gauge boson couplings for extended Higgs sectors, comparing the three models under our investigation.

2.2.2. Field Content and Bi-Triplet Structure

In the GM model, the SM Higgs doublet ϕ with a complex triplet χ (hypercharge $Y = 1$) and a real triplet ξ ($Y = 0$). These fields are represented as:

$$\phi = \begin{pmatrix} \phi^+ \\ \phi^0 \end{pmatrix}, \quad \chi = \begin{pmatrix} \chi^{++} \\ \chi^+ \\ \chi^0 \end{pmatrix}, \quad \xi = \begin{pmatrix} \xi^+ \\ \xi^0 \\ \xi^- \end{pmatrix}. \quad (2.31)$$

To make custodial symmetry manifest, the scalar fields are embedded in representations of the global $SU(2)_L \times SU(2)_R$ symmetry. The doublet is recast as a bidoublet Φ , and the two triplets as a bitriplet Δ as the following forms

$$\Phi = \begin{pmatrix} \phi^{0*} & \phi^+ \\ -\phi^- & \phi^0 \end{pmatrix}, \quad \Delta = \begin{pmatrix} \chi^{0*} & \xi^+ & \chi^{++} \\ -\chi^- & \xi^0 & \chi^+ \\ \chi^{--} & -\xi^- & \chi^0 \end{pmatrix}. \quad (2.32)$$

After EWSB, the neutral components are decomposed as follows¹:

$$\phi^0 = \frac{1}{\sqrt{2}}(\nu_\phi + \phi_r^0 + i\phi_i^0), \quad \chi^0 = \nu_\chi + \frac{1}{\sqrt{2}}(\chi_r^0 + i\chi_i^0), \quad \xi^0 = \nu_\chi + \xi_r^0. \quad (2.33)$$

The vacuum expectation values (vevs) are defined as:

$$\langle \Phi \rangle = \frac{\nu_\phi}{\sqrt{2}} \mathbb{1}_{2 \times 2}, \quad \langle \Delta \rangle = \nu_\chi \mathbb{1}_{3 \times 3}, \quad (2.34)$$

where ν_ϕ and ν_χ are the doublet and triplet vevs, respectively.

¹It is important to note the difference in the vev structure between the triplet and doublet vev as mentioned in: see Eq. 2.33.

The full Lagrangian of the GM model is written as:

$$\mathcal{L}_{GM} = \mathcal{L}_{kin} + \mathcal{L}_{Yuk} + \mathcal{L}_v - V_{GM}(\Phi, \Delta), \quad (2.35)$$

where \mathcal{L}_{kin} contains the kinetic and gauge interactions, \mathcal{L}_{Yuk} is the Yukawa interaction between the Higgs doublet and fermions, \mathcal{L}_v involves neutrino couplings to the triplets, and $V_{GM}(\Phi, \Delta)$ is the custodially symmetric scalar potential of the model.

2.2.3. Vacuum Alignment and Custodial Symmetry

The scalar fields in the GM model transform under a global $SU(2)_L \times SU(2)_R$ symmetry, which is spontaneously broken down to the custodial $SU(2)_C$ subgroup after EWSB. To manifest this symmetry structure, the Higgs doublet Φ is promoted to a bi-doublet and the triplets χ and ξ are organized into a bi-triplet under $SU(2)_L \times SU(2)_R$.

The vacuum expectation values (vevs) are chosen to preserve custodial symmetry by aligning the vevs in the direction of the identity:

$$\langle \Phi \rangle = \begin{pmatrix} v_\phi/\sqrt{2} & 0 \\ 0 & v_\phi/\sqrt{2} \end{pmatrix}, \quad \langle X \rangle = \begin{pmatrix} v_\chi & 0 & 0 \\ 0 & v_\chi & 0 \\ 0 & 0 & v_\chi \end{pmatrix}. \quad (2.36)$$

The combination of these vevs gives the electroweak scale as:

$$v^2 = v_\phi^2 + 8v_\chi^2 = \frac{4M_W^2}{g^2} \approx (246 \text{ GeV})^2. \quad (2.37)$$

and the vev decomposition gives

$$\tan \theta_H = 2\sqrt{2} \frac{v_\Delta}{v_\phi}. \quad (2.38)$$

where θ_H is the CP odd and charged state mixing angle.

To ensure custodial symmetry is preserved after symmetry breaking, we impose the condition $v_\chi = v_\xi$, so that the neutral components χ^0 and ξ^0 acquire the same vev. This choice is not unique, but is necessary to maintain $\rho = 1$ at the tree level. The phase conventions for the scalar components are set as:

$$\chi^{--} = (\chi^{++})^*, \quad \chi^- = -(\chi^+)^*, \quad \phi^- = -(\phi^+)^*, \quad \xi^- = -(\xi^+)^*, \quad \xi^0 = (\xi^0)^*.$$

A detailed discussion on custodial symmetry preservation and its role in maintaining $\rho = 1$ can be found in [19].

2.2.4. Scalar Potential and Tadpole Conditions

The most general custodially symmetric scalar potential is given by:

$$\begin{aligned} V_{GM}(\Phi, \Delta) = & \frac{m_\phi^2}{2} \text{Tr}(\Phi^\dagger \Phi) + \frac{m_\Delta^2}{2} \text{Tr}(\Delta^\dagger \Delta) + \lambda_1 [\text{Tr}(\Phi^\dagger \Phi)]^2 + \lambda_2 [\text{Tr}(\Delta^\dagger \Delta)]^2 \\ & + \lambda_3 \text{Tr}(\Phi^\dagger \Phi) \text{Tr}(\Delta^\dagger \Delta) + \lambda_4 \text{Tr}(\Phi^\dagger \tau^a \Phi \tau^b) \text{Tr}(\Delta^\dagger T^a \Delta T^b) \\ & + \mu_1 \text{Tr}(\Phi^\dagger \tau^a \Phi \tau^b) (P^\dagger \Delta P)_{ab} + \mu_2 \text{Tr}(\Delta^\dagger T^a \Delta T^b) (P^\dagger \Delta P)_{ab}, \end{aligned} \quad (2.39)$$

where τ^a and T^a are the $SU(2)$ generators for doublet and triplet representations respectively, and P is the similarity transformation matrix. The matrices σ^a are the usual Pauli matrices, while the generators T^a represent the $SU(2)$ algebra in the triplet (adjoint) representation. These 3×3 matrices are defined as:

$$T^1 = \frac{1}{\sqrt{2}} \begin{pmatrix} 0 & 1 & 0 \\ 1 & 0 & 1 \\ 0 & 1 & 0 \end{pmatrix}, \quad T^2 = \frac{1}{\sqrt{2}} \begin{pmatrix} 0 & -i & 0 \\ i & 0 & -i \\ 0 & i & 0 \end{pmatrix}, \quad T^3 = \begin{pmatrix} 1 & 0 & 0 \\ 0 & 0 & 0 \\ 0 & 0 & -1 \end{pmatrix}. \quad (2.40)$$

The similarity transformation matrix P , used to rotate between different bases in the representation space, is given by:

$$P = \frac{1}{\sqrt{2}} \begin{pmatrix} -1 & i & 0 \\ 0 & 0 & \sqrt{2} \\ 1 & i & 0 \end{pmatrix}. \quad (2.41)$$

The transformation properties of the triplet field under $SU(2)_L \times SU(2)_R$, including the role of the similarity transformation matrix P , are discussed in detail in Appendix C.

2.2.5. Tadpole Conditions and Custodial Multiplets

To identify the physical vacuum, we impose the tadpole conditions by minimizing the scalar potential with respect to the real neutral components of the scalar fields, similar to the 2HDM procedure discussed in section 2.1.4:

$$\left. \frac{\partial V_H}{\partial \phi_r} \right|_{\langle \phi \rangle} = 0, \quad \left. \frac{\partial V_H}{\partial \chi_r} \right|_{\langle \chi \rangle} = 0, \quad \left. \frac{\partial V_H}{\partial \xi_r} \right|_{\langle \xi \rangle} = 0. \quad (2.42)$$

Solving these conditions allows us to eliminate the mass parameters m_1^2 and m_2^2 as:

$$m_1^2 = -v^2 \left(4\lambda_1 c_H^2 + \frac{3}{4}\lambda_4 s_H^2 + \frac{3}{8}\lambda_5 s_H^2 \right) + \frac{3}{4}s_H^2 M_1^2, \quad (2.43)$$

$$m_2^2 = -v^2 \left(\frac{3}{2}\lambda_2 s_H^2 + \frac{1}{2}\lambda_3 s_H^2 + 2\lambda_4 c_H^2 + \lambda_5 c_H^2 \right) + c_H^2 M_1^2 + \frac{1}{2}M_2^2, \quad (2.44)$$

where $s_H = \sin \theta_H$ and $c_H = \cos \theta_H$ are the mixing angles between the CP-odd and charged Higgs

states and M_1^2 and M_2^2 are the mass parameters, and are defined as:

$$\cos \theta_H = \frac{v_\phi}{v}, \quad \sin \theta_H = \frac{\sqrt{8} v_\chi}{v} \quad (2.45)$$

$$M_1^2 = -\frac{v}{\sqrt{2}s_H} \mu_1, \quad M_2^2 = -3\sqrt{2}s_H \mu_2 v. \quad (2.46)$$

2.2.6. Multiplet Structure due to Custodial Symmetry and the Scalar Physical Spectrum

After EWSB, the scalar states decompose under the custodial $SU(2)_C$ symmetry. The $SU(2)_L \times SU(2)_R$ symmetry breaks to the diagonal subgroup $SU(2)_C$, and the scalar multiplets reorganize according to their custodial transformation properties.

The Higgs doublet Φ transforms as a bi-doublet $2 \otimes 2 \rightarrow 3 \oplus 1$ under $SU(2)_C$, while the bi-triplet Δ transforms as $3 \otimes 3 \rightarrow 5 \oplus 3 \oplus 1$. The singlet states combine to form the CP-even scalars h^0 and H^0 . The triplet states combine to give the Goldstone bosons (G^\pm, G^0) and the physical triplet charged and neutral Higgs states (H_3^\pm, H_3^0). The custodial fiveplet, formed entirely from the triplets, consists of $H_5^{\pm\pm}, H_5^\pm$, and H_5^0 . Hence, these custodial multiplet states (singlet, triplet and fiveplet) are formed from the 1,3 and 5 representations of $SU(2)_c$ symmetry.

The fiveplet states are pure triplet components and do not mix with other states due to their custodial symmetry quantum numbers. For example, H_3^+ , which couples to fermions, cannot mix with H_5^+ , which couples only to vector bosons. This is a direct consequence of the custodial symmetry. This is different from septet states, H_V^\pm and H_f^\pm as we see in the next subsection.

Furthermore, custodial symmetry guarantees mass degeneracy within each multiplet. The triplet states (H_3^+, H_3^0) share a common mass m_3 , while the fiveplet states (H_5^{++}, H_5^+, H_5^0) are degenerate with mass m_5 .

2.2.7. Custodial Decomposition and Physical Spectrum from Gauge field in GM model

After EWSB, the neutral components decompose as defined in Equation 2.33. The electroweak vevs satisfy $v^2 = v_\phi^2 + 8v_\chi^2$. From the custodial $SU(2)_C$ symmetry, we obtain the following intermediate states, which are formed by the charged and neutral components of irreducible representations (irreps) of the bi-triplet Δ :

$$H_5^{\pm\pm} = \chi^{\pm\pm}, \quad (2.47)$$

$$H_5^\pm = \frac{\chi^\pm - \xi^\pm}{\sqrt{2}}, \quad (2.48)$$

$$\tilde{H}_3^\pm = \frac{\chi^\pm + \xi^\pm}{\sqrt{2}}, \quad (2.49)$$

$$\tilde{H}_3^0 = \chi^{0,i}, \quad (2.50)$$

$$\tilde{H}_1^0 = \frac{1}{\sqrt{3}} (\chi^{0,r} + \sqrt{2} \xi^{0,r}), \quad (2.51)$$

$$H_5^0 = \frac{1}{\sqrt{3}} (\chi^{0,r} - \sqrt{2} \xi^{0,r}). \quad (2.52)$$

These gauge states with a tilde ($\tilde{}$) are not mass eigenstates; they will mix with the irreducible representations (irreps.) from the doublet Φ , namely the custodial triplet ² ($\phi^+, \phi^{0,i}, \phi^-$) and the custodial singlet $\phi^{0,r}$.

Rotation of gauge states to obtain physical states

The custodial triplet components (from Φ and Δ) are rotated using the mixing angle θ_H to give the Goldstones and the physical custodial triplet and fiveplet (H_3^0, H_5^0, H_3^\pm and H_5^\pm). The singlets (from Φ and Δ) mix with angle α to give the two CP-even Higgs bosons (h^0, H^0):

$$\begin{pmatrix} \phi^{0,i} \\ \tilde{H}_3^0 \end{pmatrix} = \begin{pmatrix} \cos \theta_H & \sin \theta_H \\ \sin \theta_H & \cos \theta_H \end{pmatrix} \begin{pmatrix} G^0 \\ H_3^0 \end{pmatrix}, \quad (2.53)$$

$$\begin{pmatrix} \phi^+ \\ \tilde{H}_3^+ \\ H_5^+ \end{pmatrix} = \begin{pmatrix} \cos \theta_H & \sin \theta_H & 0 \\ \sin \theta_H & \cos \theta_H & 0 \\ 0 & 0 & 1 \end{pmatrix} \begin{pmatrix} G^+ \\ H_3^+ \\ H_5^+ \end{pmatrix}, \quad (2.54)$$

$$\begin{pmatrix} \phi^{0,r} \\ \tilde{H}_1^0 \\ H_5^0 \end{pmatrix} = \begin{pmatrix} \cos \alpha & \sin \alpha & 0 \\ \sin \alpha & \cos \alpha & 0 \\ 0 & 0 & 1 \end{pmatrix} \begin{pmatrix} h^0 \\ H^0 \\ H_5^0 \end{pmatrix}. \quad (2.55)$$

These relations are the replacement rules, which are used whenever amplitudes are written in the gauge basis, the physical fields are obtained by the above rotations. These are important to find the couplings between the vector bosons and physical Higgs states.

Using the intermediate definitions above and the rotation matrices, the mass eigenstates are ex-

²not to be confused with the triplet Higgs states as discussed in sub-section 2.2.6

pressed directly in terms of the gauge fields as

$$h^0 = \cos \alpha \phi^{0,r} - \sin \alpha \left(\frac{1}{\sqrt{3}} \chi^{0,r} + \sqrt{\frac{2}{3}} \xi^{0,r} \right), \quad (2.56)$$

$$H^0 = \sin \alpha \phi^{0,r} + \cos \alpha \left(\frac{1}{\sqrt{3}} \chi^{0,r} + \sqrt{\frac{2}{3}} \xi^{0,r} \right), \quad (2.57)$$

$$H_5^0 = \sqrt{\frac{2}{3}} \xi^{0,r} - \frac{1}{\sqrt{3}} \chi^{0,r}, \quad (2.58)$$

where the above states correspond to the CP-even physical states and for the CP-odd/charged states the relations are as follows

$$G^0 = \cos \theta_H \phi^{0,i} + \sin \theta_H \chi^{0,i}, \quad (2.59)$$

$$H_3^0 = -\sin \theta_H \phi^{0,i} + \cos \theta_H \chi^{0,i}, \quad (2.60)$$

$$G^\pm = \cos \theta_H \phi^\pm + \sin \theta_H \frac{\chi^\pm + \xi^\pm}{\sqrt{2}}, \quad (2.61)$$

$$H_3^\pm = -\sin \theta_H \phi^\pm + \cos \theta_H \frac{\chi^\pm + \xi^\pm}{\sqrt{2}}, \quad (2.62)$$

$$H_5^\pm = \frac{\chi^\pm - \xi^\pm}{\sqrt{2}}, \quad H_5^{++} = \chi^{++}. \quad (2.63)$$

The Equations (2.56)–(2.63) provide the relevant mass eigenstates for our analysis. The final spectrum includes three CP-even neutrals (h^0, H^0, H_5^0), one CP-odd neutral H_3^0 (and goldstone neutral state G^0), two singly charged pairs (H_3^\pm, H_5^\pm) (and charged goldstone states G^\pm), and one doubly charged pair $H_5^{\pm\pm}$. It is important to note that the fiveplet states ($H_5^{\pm\pm}, H_5^\pm, H_5^0$) are only mixed using the triplets, and custodial symmetry enforces $m(H_5^{\pm\pm}) = m(H_5^\pm) = m(H_5^0) \equiv m_5$ and $m(H_3^\pm) = m(H_3^0) \equiv m_3$.

2.2.8. Electroweak Lagrangian and Gauge Boson Couplings in the GM Model

The electroweak gauge interactions of the GM model arise from the kinetic terms of the scalar fields, which include the SM-like Higgs doublet ϕ , the complex triplet χ , and the real triplet ξ . The full kinetic Lagrangian is given by:

$$\mathcal{L}_{\text{kin}} = (D^\mu(\phi)\phi)^\dagger D_\mu(\phi)\phi + (D^\mu(\chi)\chi)^\dagger D_\mu(\chi)\chi + \frac{1}{2}(D^\mu(\xi)\xi)^\dagger D_\mu(\xi)\xi - V_{GM}(\Phi, \Delta), \quad (2.64)$$

where $D_\mu(i)(i = \phi, \chi, \xi)$, see Eq. 2.65, 2.66 and 2.67,³ are the covariant derivatives acting on the respective fields, and $V_{GM}(\Phi, \Delta)$ is the scalar potential of the GM model as shown in Equation 2.39.

³Here $D_\mu(\phi)$ is not a function of ϕ itself, it is used to distinguish between the different covariant derivatives defined according to the dimensions of the fields (ϕ, χ, ξ) and thus are written this way.

The explicit forms of the covariant derivatives are:

$$D_\mu(\phi) = \partial_\mu - i \frac{g}{\sqrt{2}} \begin{pmatrix} 0 & W_\mu^+ \\ W_\mu^- & 0 \end{pmatrix} - i \frac{Z_\mu}{2} \begin{pmatrix} -g's_W + gc_W & 0 \\ 0 & -g's_W + gc_W \end{pmatrix}, \quad (2.65)$$

$$D_\mu(\xi) = \partial_\mu - ig \begin{pmatrix} 0 & W_\mu^+ & 0 \\ W_\mu^- & 0 & W_\mu^+ \\ 0 & W_\mu^- & 0 \end{pmatrix} - iZ_\mu \begin{pmatrix} g'c_W & 0 & 0 \\ 0 & 0 & 0 \\ 0 & 0 & -gc_W \end{pmatrix}, \quad (2.66)$$

$$D_\mu(\chi) = \partial_\mu - ig \begin{pmatrix} 0 & W_\mu^+ & 0 \\ W_\mu^- & 0 & W_\mu^+ \\ 0 & W_\mu^- & 0 \end{pmatrix} - iZ_\mu \begin{pmatrix} -g's_W + gc_W & 0 & 0 \\ 0 & -g's_W & 0 \\ 0 & 0 & -g's_W - gc_W \end{pmatrix}. \quad (2.67)$$

The hypercharge assignments used here are:

$$Y(\phi) = \frac{1}{2}, \quad Y(\xi) = 0, \quad Y(\chi) = 1.$$

The interaction terms involving vector bosons arise when these covariant derivatives act on the fields after electroweak symmetry breaking. The resulting Higgs–vector boson couplings can be derived by expanding the Lagrangian and are given below. You can find all couplings in Appendix D. The couplings were generated using `Mathematica` in the analysis of Ref. [14].

Using the mixing angle θ_H , defined in Eq. 2.45, we find the effective couplings of CP-even states:

$$\kappa_V^{h^0} = \cos \theta_H \cos \alpha - \frac{\sqrt{8}}{\sqrt{3}} \sin \theta_H \sin \alpha, \quad (2.68)$$

$$\kappa_V^{H^0} = \cos \theta_H \sin \alpha + \frac{\sqrt{8}}{\sqrt{3}} \sin \theta_H \cos \alpha, \quad (2.69)$$

$$\kappa_{WW}^{H_5^0} = \frac{1}{\sqrt{3}} \sin \theta_H, \quad \kappa_{ZZ}^{H_5^0} = -\frac{2}{\sqrt{3}} \sin \theta_H. \quad (2.70)$$

The effective coupling Table 2.2 shows all GM Higgs states coupling with vector boson W^\pm, Z

Interaction ($\kappa_{VV}^{h^i}$)	Effective Coupling
$\kappa_{WW}^{h^0}$	$c_H c_\alpha - \frac{\sqrt{8}}{\sqrt{3}} s_H s_\alpha$
$\kappa_{ZZ}^{h^0}$	$c_H c_\alpha - \frac{\sqrt{8}}{\sqrt{3}} s_H s_\alpha$
$\kappa_{WW}^{H_5^0}$	$-\frac{2}{\sqrt{3}} s_H$
$\kappa_{ZZ}^{H_5^0}$	$-\frac{2}{\sqrt{3}} s_H$
$\kappa_{WW}^{H_5^{++}}$	$\sqrt{2} s_H$
$\kappa_{WW}^{H^0}$	$c_H s_\alpha + \frac{\sqrt{8}}{\sqrt{3}} s_H c_\alpha$
$\kappa_{ZZ}^{H^0}$	$c_H s_\alpha + \frac{\sqrt{8}}{\sqrt{3}} s_H c_\alpha$
$\kappa_{W^+ W^-}^{H_5^0}$	$-\frac{1}{\sqrt{3}} s_H$
$\kappa_{W^\pm Z}^{H_5^+}$	s_H

Table 2.2.: Effective couplings of GM Higgs states to gauge bosons in terms of mixing angles s_H , c_H , and α .

These couplings exceed unity and satisfy the sum rule

$$\left(\kappa_V^{h^0}\right)^2 + \left(\kappa_V^{H^0}\right)^2 = \cos^2 \theta_H + \frac{8}{3} \sin^2 \theta_H \geq 1, \quad (2.71)$$

indicating the enhancement of gauge couplings in the GM model compared to the SM or 2HDM.

From Equation 2.30, we can see an α dependency in the 2HDM sum rule that is not present in GM. These coupling patterns are essential for collider phenomenology and will be compared across models in the next chapter through theoretical sum rules.

2.3. The Scalar Septet Model

The scalar Septet Model [16, 17] extends the scalar sector of the SM by introducing a complex $SU(2)_L$ septet scalar field with hypercharge $Y = 2$. This higher-dimensional representation introduces an additional higher charged state, including the doubly charged Higgs state H^{++} as we also see in the GM, up to H^{+5} and the gauge structure also modifies the SM Higgs couplings while maintaining tree-level custodial symmetry ($\rho = 1$) [18].

Field Content and VEV Structure

The field content includes the SM Higgs doublet ϕ and a septet field X with isospin $T = 3$ and $Y = 2$:

$$\Phi = \begin{pmatrix} \phi^+ \\ \phi^0 \end{pmatrix}, \quad X = \begin{pmatrix} \chi^{+5} \\ \chi^{+4} \\ \chi^{+3} \\ \chi^{+2} \\ \chi_1^{+1} \\ \chi^0 \\ \chi_2^{-1} \end{pmatrix}. \quad (2.72)$$

To ensure $\rho = 1$ at the tree level, the neutral components of the septet field attain doublet and triplet vevs, v_ϕ and v_χ . It is important to note that χ_1^{+1} and χ_2^{-1} have different T^3 quantum numbers, see Equation 2.89, and they are independent states, and hence they are labeled χ_1 , where χ_2 and $(\chi_1^{+1})^* \neq \chi_2^{-1}$ [17].

The neutral components are expanded around the vacuum as follows:

$$\phi^0 = \frac{1}{\sqrt{2}}(v_\phi + \phi^{0,r} + i\phi^{0,i}), \quad \chi^0 = v_\chi + \chi^{0,r} + i\chi^{0,i}. \quad (2.73)$$

where $\phi^{0,r}, \phi^{0,i}$ and $\chi^{0,r}, \chi^{0,i}$ are the real and imaginary components of the neutral decomposed state of the doublet and triplet, respectively.

The total electroweak vev structure for the septet is given by:

$$v^2 = v_\phi^2 + 16v_\chi^2 = \frac{1}{\sqrt{2}G_F} \simeq (246 \text{ GeV})^2, \quad (2.74)$$

where G_F is the Fermi constant.

The mixing angle of the septet representation θ_7 is defined as:

$$\cos \theta_7 \equiv c_7 = \frac{v_\phi}{v}, \quad \sin \theta_7 \equiv s_7 = \frac{4v_\chi}{v}. \quad (2.75)$$

2.3.1. Physical Spectrum and Mixing of Gauge states to Physics states

After EWSB, the physical spectrum includes the following 15 states:

- Two CP-even neutral scalars: h (light) and H (heavy),
- One CP-odd neutral scalar: A , and the goldston bosons G^0 and G^\pm
- Two singly-charged Higgs bosons: H_1^\pm and H_2^\pm ,
- A doubly-charged scalar: $H^{++} \equiv \chi^{+2}$,
- Additional highly charged states: $\chi^{\pm 3}, \chi^{\pm 4}, \chi^{\pm 5}$.

The Goldstone bosons that are “eaten” by Z and W^\pm are:

$$G^0 = c_7 \phi^{0,i} + s_7 \chi^{0,i}, \quad (2.76)$$

$$G^\pm = c_7 \phi^\pm + s_7 \left(\sqrt{\frac{5}{8}} \chi_1^{\pm 1} - \sqrt{\frac{3}{8}} (\chi_2^{-1})^* \right). \quad (2.77)$$

The CP-even mass eigenstates are:

$$h = c_\alpha \phi^{0,r} - s_\alpha \chi^{0,r}, \quad (2.78)$$

$$H = s_\alpha \phi^{0,r} + c_\alpha \chi^{0,r}, \quad (2.79)$$

where $c_\alpha = \cos \alpha$, $s_\alpha = \sin \alpha$ and α is the CP-even mixing angle.

The CP-odd neutral scalar orthogonal to G^0 is:

$$A = -s_7 \phi^{0,i} + c_7 \chi^{0,i}. \quad (2.80)$$

The two singly-charged fields that mix into physical eigenstates are:

$$H_f^+ = -s_7 \phi^+ + c_7 \left(\sqrt{\frac{5}{8}} \chi_1^{+1} - \sqrt{\frac{3}{8}} (\chi_2^{-1})^* \right), \quad (2.81)$$

$$H_V^+ = \sqrt{\frac{3}{8}} \chi_1^{+1} + \sqrt{\frac{5}{8}} (\chi_2^{-1})^*. \quad (2.82)$$

Here, H_f^+ couples to fermions but not gauge bosons, and H_V^+ couples to gauge bosons but not to fermions. We saw similar behavior in states in GM due to custodial symmetry, with the difference that in the septet model, the mixing of the H_V^\pm and H_f^\pm is allowed, and hence we obtain the physical states H_1^\pm and H_2^\pm . The physical mass eigenstates are then:

$$H_1^+ = c_\gamma H_f^+ - s_\gamma H_V^+, \quad (2.83)$$

$$H_2^+ = s_\gamma H_f^+ + c_\gamma H_V^+, \quad (2.84)$$

where $c_\gamma = \cos \gamma$, $s_\gamma = \sin \gamma$ and γ is the mixing angle for the rotation of the charge stated in the septet model [17]. The model contains higher charged scalars, including the doubly charged state, which we also saw in the GM model:

$$H^{++} = \chi^{+2}, H^{+3} = \chi^{+3}, H^{+4} = \chi^{+4} \text{ and } H^{+5} = \chi^{+5} \quad (2.85)$$

where H^{++} couples to $W^- W^-$ and can give rise to distinct collider signatures, such as same-sign dilepton or diboson final states [17].

2.3.2. Couplings to Gauge Boson

The kinetic term of the Lagrangian of the scalar gives us the couplings with the gauge bosons:

$$\mathcal{L} \supset (D^\mu \Phi)^\dagger (D_\mu \Phi) + (D^\mu X)^\dagger (D_\mu X), \quad (2.86)$$

where the covariant derivative is defined as:

$$D_\mu = \partial_\mu - i \frac{g}{\sqrt{2}} \left(W_\mu^+ T^+ + W_\mu^- T^- \right) - i \frac{e}{s_W c_W} Z_\mu (T^3 - s_W^2 Q) - ie A_\mu Q. \quad (2.87)$$

where s_W and c_W denote $\sin \theta_W$ and $\cos \theta_W$ respectively, where θ_W is the weak mixing angle. The generators T^a for the doublet are $T^a = \sigma^a/2$, where σ^a refers to the Pauli matrices. Here, $T^\pm = T^1 \pm iT^2$ are the septet representations of SU(2) generators,

$$T^+ = \begin{pmatrix} 0 & \sqrt{6} & 0 & 0 & 0 & 0 & 0 \\ 0 & 0 & \sqrt{10} & 0 & 0 & 0 & 0 \\ 0 & 0 & 0 & 2\sqrt{3} & 0 & 0 & 0 \\ 0 & 0 & 0 & 0 & 2\sqrt{3} & 0 & 0 \\ 0 & 0 & 0 & 0 & 0 & \sqrt{10} & 0 \\ 0 & 0 & 0 & 0 & 0 & 0 & \sqrt{6} \\ 0 & 0 & 0 & 0 & 0 & 0 & 0 \end{pmatrix}, \quad (2.88)$$

$$T^3 = \begin{pmatrix} 3 & 0 & 0 & 0 & 0 & 0 & 0 \\ 0 & 2 & 0 & 0 & 0 & 0 & 0 \\ 0 & 0 & 1 & 0 & 0 & 0 & 0 \\ 0 & 0 & 0 & 0 & 0 & 0 & 0 \\ 0 & 0 & 0 & 0 & -1 & 0 & 0 \\ 0 & 0 & 0 & 0 & 0 & -2 & 0 \\ 0 & 0 & 0 & 0 & 0 & 0 & -3 \end{pmatrix}, \quad (2.89)$$

$$T^- = (T^+)^T. \quad (2.90)$$

After expanding the kinetic lagrangian, we obtain the following effective couplings of the neutral scalars to WW and ZZ are:

$$\kappa_{WW}^{h^0} = \kappa_{ZZ}^{h^0} = c_7 c_\alpha - 4 s_7 s_\alpha \equiv \kappa_V^h, \quad (2.91)$$

$$\kappa_{WW}^{H^0} = \kappa_{ZZ}^{H^0} = c_7 s_\alpha + 4 s_7 c_\alpha \equiv \kappa_V^H. \quad (2.92)$$

The singly- and doubly-charged states also have non-zero couplings to vector bosons:

$$\kappa_{WZ}^{H_V^+} = -\sqrt{15} s_7, \quad (2.93)$$

$$\kappa_{WW}^{H^{++}} = \sqrt{15} s_7. \quad (2.94)$$

The couplings of the physical singly-charged mass eigenstates H_1^+ and H_2^+ , which arise from mixing of H_f^+ and H_V^+ by an angle γ , are:

$$\kappa_{WZ}^{H_1^+} = \sqrt{15} s_7 s_\gamma, \quad (2.95)$$

$$\kappa_{WZ}^{H_2^+} = -\sqrt{15} s_7 c_\gamma. \quad (2.96)$$

The following Table 2.3 contains the effective couplings of the Septet model higgs states to vector bosons:

Interaction	Effective Coupling
$\kappa_{WW}^{h^0} = \kappa_{ZZ}^{h^0}$	$c_7 c_\alpha - 4 s_7 s_\alpha \equiv \kappa_V^h$
$\kappa_{WW}^{H^0} = \kappa_{ZZ}^{H^0}$	$c_7 s_\alpha + 4 s_7 c_\alpha \equiv \kappa_V^H$
$\kappa_{WZ}^{H_V^+}$	$-\sqrt{15} s_7$
$\kappa_{WW}^{H^{++}}$	$\sqrt{15} s_7$
$\kappa_{WZ}^{H_1^+}$	$\sqrt{15} s_7 s_\gamma$
$\kappa_{WZ}^{H_2^+}$	$-\sqrt{15} s_7 c_\gamma$

Table 2.3.: Effective couplings of septet Higgs states to gauge bosons.

The WW and ZZ couplings of h and H satisfy the generalized sum rule:

$$(\kappa_V^h)^2 + (\kappa_V^H)^2 = c_7^2 + 16 s_7^2 \geq 1. \quad (2.97)$$

This identity is consistent with unitarity constraints in longitudinal vector boson scattering processes. The enhancement of the gauge boson couplings, especially for $\kappa_V^H > 1$, can lead to ob-

servable deviations from the SM at high energies. However, perturbative unitarity is preserved due to the charged scalar exchange contributions which cancel the energy growth in amplitudes like $W_L^+ W_L^- \rightarrow W_L^+ W_L^-$ [17]. We will discuss this in detail in the next chapter, where we will also derive the matrix elements of the vector-boson scattering for our extended Higgs models and the sum rules for the same.

3. Higgs and Vector Boson Scattering

Unitarity Sum Rules

Extended Higgs sectors such as the Two-Higgs-Doublet Model (2HDM), the Georgi-Machacek (GM) model, and the Septet Model modify the couplings of CP-even scalars to electroweak vector bosons. These modified couplings affect longitudinal vector boson scattering amplitudes at high energies, which can grow with center-of-mass energy and violate perturbative unitarity if not properly constrained [19, 17].

This chapter focuses on high-energy $W_L^+ W_L^- \rightarrow W_L^+ W_L^-$ scattering and derives the associated unitarity sum rules. The related processes $W_L^+ W_L^- \rightarrow Z_L Z_L$ and $Z_L Z_L \rightarrow Z_L Z_L$ are discussed in Appendix E, where we also show that $Z_L Z_L \rightarrow Z_L Z_L$ does not exhibit any bad high-energy behavior from gauge boson exchange, and that the Higgs-mediated terms follow a similar sum rule structure as discussed in the following sections [13].

We begin with the 2HDM coupling sum rules and their implications for $VV \rightarrow VV$ scattering in the first section. The Higgs-exchange matrix elements in the GM and Septet models are then analyzed in sections 3.2 and 3.3. Lastly, in section 3.4 we derive perturbative–unitarity mass bounds using the unitarity condition $|\text{Re } a_0| \leq \frac{1}{2}$, see Eq. 1.22 in section 1.3.2. This section is a continuation of the SM mass bound section 1.4 in the decoupling cases ($\kappa_V^{H^0} = 0$) and obtaining analytic constraints on m_{H^0} , m_5 , and $m_{H^{++}}$ as functions of the relevant κ_V couplings [13].

3.1. Vector Boson Scattering in the 2HDM

In 2HDM, both CP-even scalars h^0 and H^0 contribute to $W_L^+ W_L^- \rightarrow W_L^+ W_L^-$ scattering, through s - and t -channel Higgs exchange. The relevant Feynman diagrams are shown in Figure 3.1.

At high energy ($s \gg m_{h^0}^2, m_{H^0}^2$), the matrix element for the s - and t -channel h^0 and H^0 propagators is given by [13]:

$$i\mathcal{M}_{\text{Higgs}} = -i \frac{g^2}{4m_W^2} \left[\left(\kappa_{WW}^{h^0} \right)^2 \left(\frac{s^2}{s - m_{h^0}^2} + \frac{t^2}{t - m_{h^0}^2} \right) + \left(\kappa_{WW}^{H^0} \right)^2 \left(\frac{s^2}{s - m_{H^0}^2} + \frac{t^2}{t - m_{H^0}^2} \right) \right], \quad (3.1)$$

$$\mathcal{M}_{\text{Higgs}} \simeq -\frac{1}{v^2} \left[\left(\left(\kappa_{WW}^{h^0} \right)^2 + \left(\kappa_{WW}^{H^0} \right)^2 \right) (s+t) + 2 \left(\kappa_{WW}^{h^0} \right)^2 m_{h^0}^2 + 2 \left(\kappa_{WW}^{H^0} \right)^2 m_{H^0}^2 + \dots \right]. \quad (3.2)$$

This expression is obtained by Taylor expanding the propagator in the high-energy limit and keeping only the leading terms in s, t . The potentially bad high energy behaviour $\mathcal{O}(E^2)$ is canceled when the sum of squared couplings satisfies [19]:

$$\left(\kappa_{WW}^{h^0} \right)^2 + \left(\kappa_{WW}^{H^0} \right)^2 = 1. \quad (3.3)$$

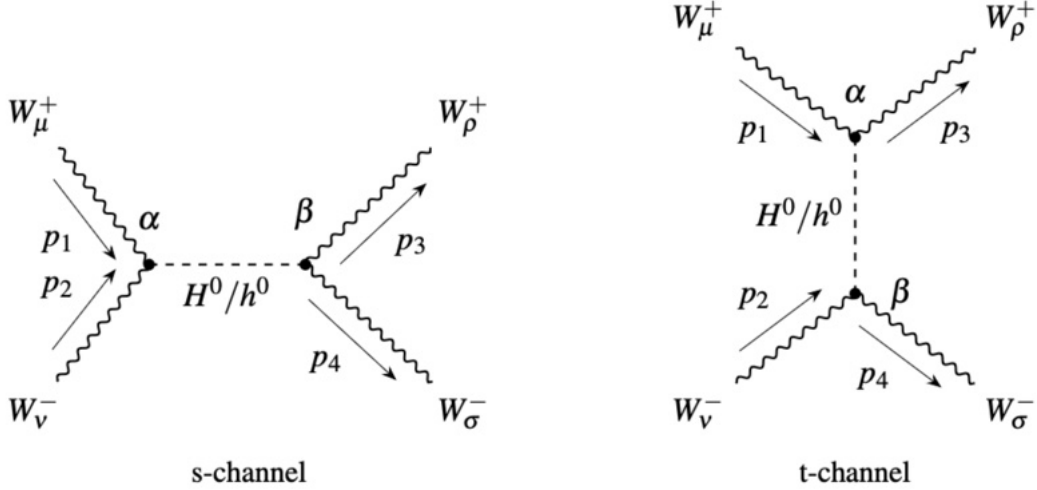


Figure 3.1.: Feynman diagrams for $W_L^+W_L^- \rightarrow W_L^+W_L^-$ in the 2HDM via h^0 and H^0 exchange in the s - and t -channel.

From Table 2.1, this identity holds because:

$$\kappa_{WW}^{h^0} = \sin(\beta - \alpha), \quad \kappa_{WW}^{H^0} = \cos(\beta - \alpha), \quad (3.4)$$

so $\sin^2(\beta - \alpha) + \cos^2(\beta - \alpha) = 1$.

Combining all relevant VBS(vector boson scattering) channels, the generalised unitarity sum rules for the 2HDM are:

$$\begin{aligned} \left(\kappa_{VV}^{h^0} \right)^2 + \left(\kappa_{VV}^{H^0} \right)^2 &= 1, \quad V = W, Z \text{ or} \\ \sum_i g_{h_i VV}^2 &= g_{H_{\text{SM}} VV}^2, \quad h_i = h^0, H^0 \end{aligned} \quad (3.5)$$

3.2. Vector Boson Scattering in the GM Model

In the GM model, the process $W_L^+W_L^- \rightarrow W_L^+W_L^-$ receives contributions from the exchange of four CP-even scalars: h^0, H^0 , the custodial singlet H_5^0 , and the doubly charged scalar H_5^{++} . The full set of Higgs-mediated Feynman diagrams is shown in Figure 3.2, including the s - and t -channel exchanges of h^0, H^0 , and H_5^0 , and the u -channel exchange of H_5^{++} .

The matrix element from these Higgs-mediated diagrams is given by [13]:

$$\begin{aligned} \mathcal{M}_{Higgs} = -\frac{1}{v^2} &\left[\left(\kappa_{WW}^{h^0} \right)^2 \left(\frac{s^2}{s - m_{h^0}^2} + \frac{t^2}{t - m_{h^0}^2} \right) + \left(\kappa_{WW}^{H^0} \right)^2 \left(\frac{s^2}{s - m_{H^0}^2} + \frac{t^2}{t - m_{H^0}^2} \right) \right. \\ &+ \left. \left(\kappa_{WW}^{H_5^0} \right)^2 \left(\frac{s^2}{s - m_5^2} + \frac{t^2}{t - m_5^2} \right) + \left(\kappa_{WW}^{H_5^{++}} \right)^2 \left(\frac{u^2}{u - m_5^2} \right) \right]. \end{aligned} \quad (3.6)$$

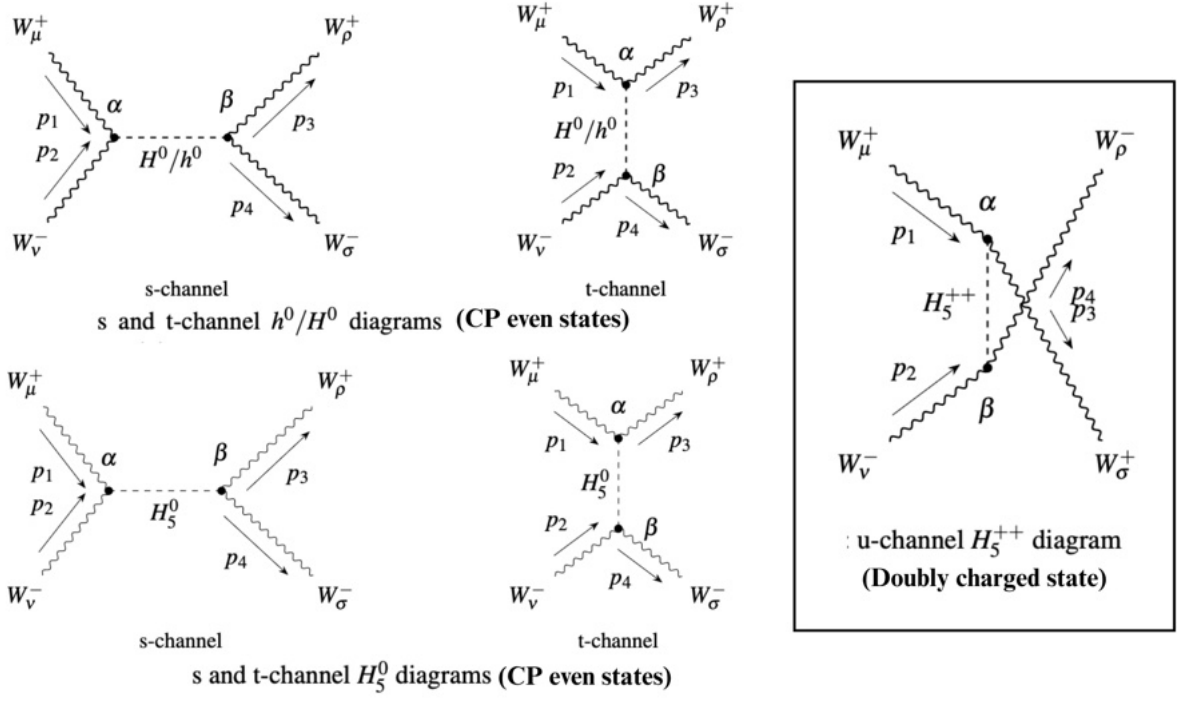


Figure 3.2.: Feynman diagrams for $W_L^+ W_L^- \rightarrow W_L^+ W_L^-$ scattering in the GM model. Shown are the s - and t -channel exchanges of CP-even scalars h^0 , H^0 , and H_5^0 , as well as the u -channel exchange of the doubly charged scalar H_5^{++} .

In the high-energy limit ($s \gg m^2$, $u \approx -(s+t)$), the leading behavior becomes:

$$\begin{aligned} \mathcal{M} \simeq & -\frac{1}{v^2} \left[\left(\left(\kappa_{WW}^{h^0} \right)^2 + \left(\kappa_{WW}^{H^0} \right)^2 + \left(\kappa_{WW}^{H_5^0} \right)^2 - \left(\kappa_{WW}^{H_5^{++}} \right)^2 \right) (s+t) \right. \\ & \left. + 2 \left(\kappa_{WW}^{h^0} \right)^2 m_{h^0}^2 + 2 \left(\kappa_{WW}^{H^0} \right)^2 m_{H^0}^2 + 2 \left(\kappa_{WW}^{H_5^0} \right)^2 m_5^2 + \left(\kappa_{WW}^{H_5^{++}} \right)^2 m_5^2 \right]. \end{aligned} \quad (3.7)$$

The $\mathcal{O}(s+t)$ behavior must cancel against the gauge boson exchange diagrams to maintain perturbative unitarity. This leads to the sum rule [13]:

$$\begin{aligned} \left(\kappa_{WW}^{h^0} \right)^2 + \left(\kappa_{WW}^{H^0} \right)^2 + \left(\kappa_{WW}^{H_5^0} \right)^2 - \left(\kappa_{WW}^{H_5^{++}} \right)^2 &= 1, \\ \sum_i g_{h_i WW}^2 - g_{h^{++} WW}^2 &= g_{H_{SM} WW}^2, \quad \text{where } h_i = \{h^0, H^0, H_5^0\}, \quad h^{\pm\pm} = H_5^{\pm\pm}. \end{aligned} \quad (3.8)$$

This condition is analytically satisfied in the GM model. Substituting the effective couplings from the GM couplings, we get:

$$c_H^2 + \frac{8}{3}s_H^2 + \frac{1}{3}s_H^2 - 2s_H^2 = c_H^2 + s_H^2 = 1, \quad \text{which is indeed true.} \quad (3.9)$$

3.3. Vector Boson Scattering in the Septet Model

The scalar Septet model contains two neutral CP-even Higgs bosons, h and H , and a doubly charged scalar H^{++} from the septet representation. Similar to the 2HDM and GM model, the modified couplings of these scalars to the electroweak vector bosons influence the unitarity of longitudinal vector boson scattering at high energies [17].

We now consider the $W_L^+ W_L^- \rightarrow W_L^+ W_L^-$ scattering process, which receives contributions from the s - and t -channel exchange of the CP-even neutral scalars h and H , and a u -channel contribution from the doubly-charged scalar H^{++} . The relevant Feynman diagrams for $W_L^+ W_L^- \rightarrow W_L^+ W_L^-$ in the Septet model are shown in Figure 3.3, featuring h , H in the s - and t -channels, and H^{++} in the u -channel.

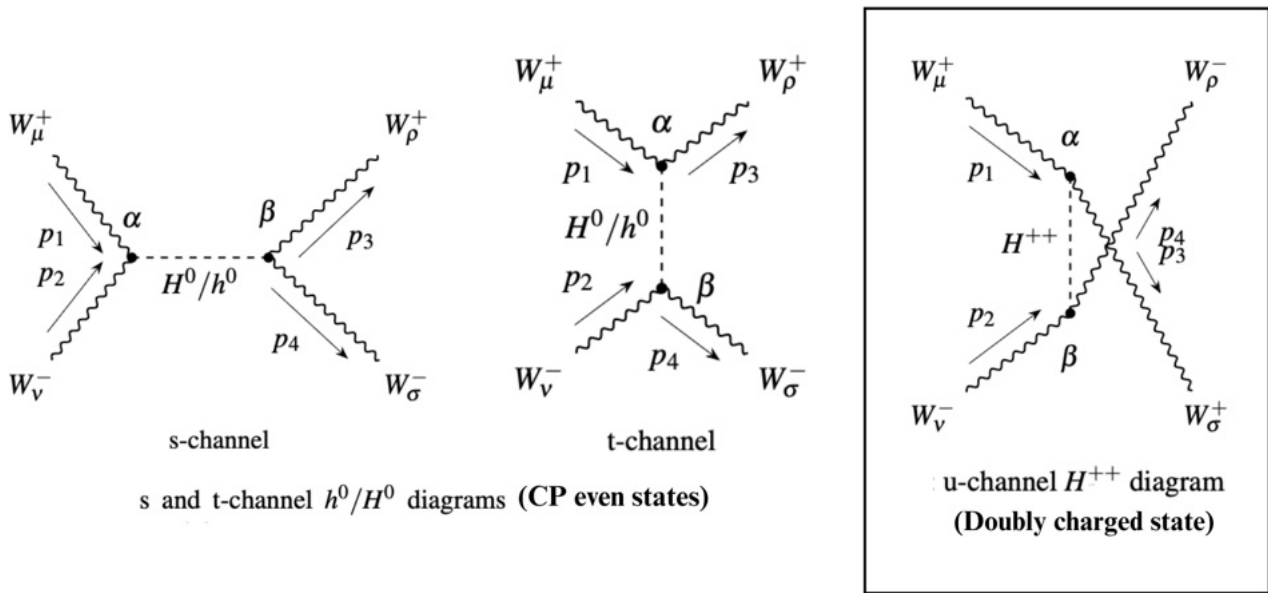


Figure 3.3.: Feynman diagrams contributing to $W_L^+ W_L^- \rightarrow W_L^+ W_L^-$ scattering in the Septet model: s - and t -channel exchange of the CP-even neutral scalars h and H , and u -channel exchange of the doubly charged scalar H^{++} .

The matrix element for this scattering process is:

$$\mathcal{M}_{Higgs} = -\frac{1}{v^2} \left[(\kappa_V^h)^2 \left(\frac{s^2}{s-m_h^2} + \frac{t^2}{t-m_h^2} \right) + (\kappa_V^H)^2 \left(\frac{s^2}{s-m_H^2} + \frac{t^2}{t-m_H^2} \right) + (\kappa_{WW}^{H^{++}})^2 \left(\frac{u^2}{u-m_{H^{++}}^2} \right) \right]. \quad (3.10)$$

where κ_V^h and κ_V^H are as defined in equation 2.92

In the high-energy limit, where $s, t, u \gg m^2$ and $u \simeq -(s+t)$, we Taylor-expand the propagators and keep only the leading terms:

$$\mathcal{M}_{Higgs} \simeq -\frac{1}{v^2} \left[((\kappa_V^h)^2 + (\kappa_V^H)^2 - (\kappa_{WW}^{H^{++}})^2) (s+t) + 2(\kappa_V^h)^2 m_h^2 + 2(\kappa_V^H)^2 m_H^2 + (\kappa_{WW}^{H^{++}})^2 m_{H^{++}}^2 \right]. \quad (3.11)$$

To ensure unitarity, the bad high-energy behavior proportional to $(s+t)$ must vanish. This cancellation yields the following **unitarity sum rule** for the Septet model [17]:

$$(\kappa_V^h)^2 + (\kappa_V^H)^2 - (\kappa_{WW}^{H^{++}})^2 = 1. \quad (3.12)$$

The effective couplings in the Septet model sum rule are defined from equation 2.92 and 2.94:

$$\kappa_{WW}^h = \kappa_{ZZ}^h = c_7 c_\alpha - 4 s_7 s_\alpha \equiv \kappa_V^h, \quad (3.13)$$

$$\kappa_{WW}^H = \kappa_{ZZ}^H = c_7 s_\alpha + 4 s_7 c_\alpha \equiv \kappa_V^H, \quad (3.14)$$

$$\kappa_{WW}^{H^{++}} = \sqrt{15} s_7. \quad (3.15)$$

After calculating analytically from the above equation, we indeed see a similar trend as the GM model,

$$c_7^2 + 16 s_7^2 - 15 s_7^2 = c_7^2 + s_7^2 = 1, \quad (3.16)$$

where we can see no dependence on α and that the sum rule holds true.

These expressions ensure custodial symmetry and allow us to evaluate whether the sum rule is satisfied for given mixing angles θ_7 and α . The presence of the H^{++} scalar uniquely distinguishes the Septet and GM model from 2HDM, and its contribution must be included to maintain perturbative unitarity in the scattering amplitude [17].

3.4. Theoretical Mass Bounds from Perturbative Unitarity Constraints

The perturbative unitarity of the S -matrix places theoretical constraints on the scattering amplitudes of $2 \rightarrow 2$ processes in quantum field theory. When the center-of-mass energy E_{COM} is much larger than the masses of the particles involved, the scattering amplitude \mathcal{M} can be expanded in partial waves as follows:

$$\mathcal{M} = 16\pi \sum_{l=0}^{\infty} (2l+1) a_l(|\vec{p}|) P_l(\cos \theta), \quad (3.17)$$

where a_l are the partial wave amplitudes and P_l are Legendre polynomials. In the leading order, the s -wave ($l = 0$) dominates, giving $\mathcal{M} \simeq 16\pi a_0 + \dots$. The tree-level unitarity condition requires $|\text{Re}(a_l)| \leq \frac{1}{2}$, and for scattering processes at the tree level, a_l are real, so we apply $|\text{Re}(a_0)| \leq \frac{1}{2}$ as the primary bound. The following mass bounds are discussed using the analysis done in [13, 17].

3.4.1. Standard Model

As discussed in section 1.4, for $W_L^+ W_L^- \rightarrow W_L^+ W_L^-$ scattering in the SM, after gauge and Higgs contributions cancel the high-energy growth, the finite remainder of the amplitude is:

$$\mathcal{M} \simeq -\frac{1}{v^2} (2m_H^2) = 16\pi a_0, \quad (3.18)$$

where H is the SM Higgs boson and $v \simeq 246$ GeV. This gives $a_0 = -\frac{m_H^2}{8\pi v^2}$, and the unitarity bound $|\text{Re}(a_0)| \leq \frac{1}{2}$ implies:

$$m_H^2 \leq 4\pi v^2 \Rightarrow m_H \leq \sqrt{4\pi} v \approx 870 \text{ GeV}. \quad (3.19)$$

This bound serves as the reference for our analysis of the extended Higgs sector. The same process will be followed below to impose perturbative unitarity bounds and to obtain theoretical mass bounds for all models in our study [13].

3.4.2. Two-Higgs-Doublet Model

In 2HDM, longitudinal $W^+ W^- \rightarrow W^+ W^-$ scattering receives Higgs-exchange contributions from the two CP-even scalars h^0 and H^0 . After the gauge–Higgs cancellations, the zeroth partial-wave amplitude is obtained from Equation 3.2

$$16\pi a_0 = -\frac{1}{v^2} \left[2(\kappa_{WW}^{h^0})^2 m_{h^0}^2 + 2(\kappa_{WW}^{H^0})^2 m_{H^0}^2 \right], \quad (3.20)$$

with the unitarity sum-rule relation as seen in Equation 3.5

$$(\kappa_{WW}^{h^0})^2 + (\kappa_{WW}^{H^0})^2 = 1, \quad \text{and} \quad \kappa_{WW}^{H^0} = \kappa_{ZZ}^{H^0} = \cos(\beta - \alpha). \quad (3.21)$$

Imposing perturbative unitarity, $|\text{Re } a_0| \leq \frac{1}{2}$, yields the bound

$$(\kappa_{WW}^{H^0})^2 \leq \frac{4\pi v^2 - m_{h^0}^2}{m_{H^0}^2 - m_{h^0}^2}. \quad (3.22)$$

when we express the above bounds in terms of the mixing-angles, this gives us the following mass bound:

$$\cos^2(\beta - \alpha) \lesssim \frac{4\pi v^2 - m_{h^0}^2}{m_{H^0}^2 - m_{h^0}^2} \simeq \left(\frac{880 \text{ GeV}}{m_{H^0}} \right)^2, \quad (3.23)$$

where we used $v = 246$ GeV and $m_{h^0} = 125$ GeV. Equivalently, one may write the bound as a limit on the heavy-scalar mass [13]:

$$m_{H^0}^2 \lesssim \left(\frac{880 \text{ GeV}}{\kappa_{WW}^{H^0}} \right)^2. \quad (3.24)$$

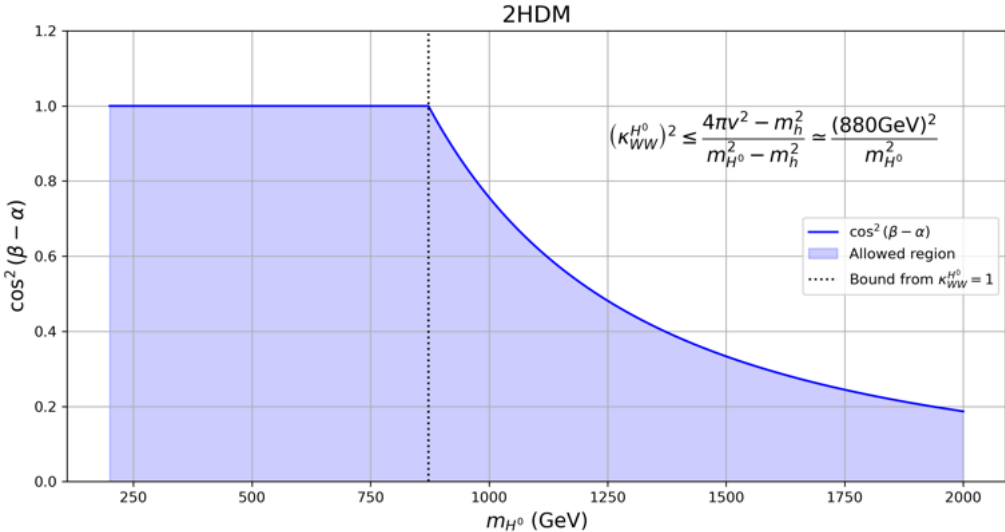


Figure 3.4.: **2HDM mass bound from perturbative unitarity.** Constraint on the heavy CP-even scalar H^0 as a function of $\kappa_{WW}^{H^0} = \cos(\beta - \alpha)$

In the plot in Figure 3.4, we see the inverse relationship between the effective vector boson coupling and mass of the heavy Higgs (H^0), which we derived from the perturbative unitarity condition in sec. 3.4. The SM reference bound in Equation 3.19 is recovered in the decoupling limit, which we can see reflected between 250 GeV and 880 GeV in the above plot.

In the special case $\kappa_{WW}^{H^0} = 0$ (i.e. $\cos(\beta - \alpha) = 0$), then $\kappa_{WW}^{H^0}$ becomes 1, see Eq. 3.21, and one recovers the SM bound discussed in sec. 3.4.1. In the generic case, increasing m_{H^0} forces $\kappa_{WW}^{H^0}$ to decrease according to Eqs. (3.22)–(3.24), exhibiting the decoupling behaviour $\kappa_{WW}^{H^0} \rightarrow 0$ as $m_{H^0} \rightarrow \infty$, while h^0 becomes SM-like [13].

3.4.3. Georgi–Machacek Model

In the GM model, the scattering process also receives contributions from the custodial fiveplet states H_5^0 and H_5^{++} . The couplings obey the custodial-symmetry-modified sum rule from GM, see Eq. 3.16:

$$(\kappa_V^{h^0})^2 + (\kappa_V^{H^0})^2 + (\kappa_{WW}^{H_5^0})^2 - (\kappa_{WW}^{H_5^{++}})^2 = 1, \quad (3.25)$$

where replacing the $\kappa_{WW}^{H_5^0} = \kappa_{WW}^{H_5^{++}} / \sqrt{6}$, we get

$$(\kappa_V^{h^0})^2 + (\kappa_V^{H^0})^2 - \frac{5}{6}(\kappa_{WW}^{H_5^{++}})^2 = 1, \quad (3.26)$$

The unitarity condition from the $W^+W^- \rightarrow W^+W^-$ scattering in Eq. 3.7 becomes:

$$2(\kappa_V^{h^0})^2 m_{h^0}^2 + 2(\kappa_V^{H^0})^2 m_{H^0}^2 + \frac{4}{3}(\kappa_{WW}^{H_5^{++}})^2 m_5^2 \leq 8\pi v^2. \quad (3.27)$$

For $\kappa_{WW}^{H^0} = 0$, $(\kappa_V^{h^0})_{\max}^2 = 1 + \frac{5}{6}(\kappa_{WW}^{H_5^{++}})^2$ and the above reduces to [13]:

$$(\kappa_{WW}^{H_5^{++}})^2 \leq \frac{3(8\pi v^2 - 2m_h^2)}{4m_5^2 + 5m_{h^0}^2} \simeq \frac{(734 \text{ GeV})^2}{m_5^2}. \quad (3.28)$$

or,

$$2\sin^2 \theta_H \leq \frac{3(8\pi v^2 - 2m_h^2)}{4m_5^2 + 5m_{h^0}^2} \simeq \frac{(734 \text{ GeV})^2}{m_5^2}. \quad (3.29)$$

This shows $s_H \propto 1/m_5$ for large m_5 , demonstrating the decoupling of the triplet contribution [13].

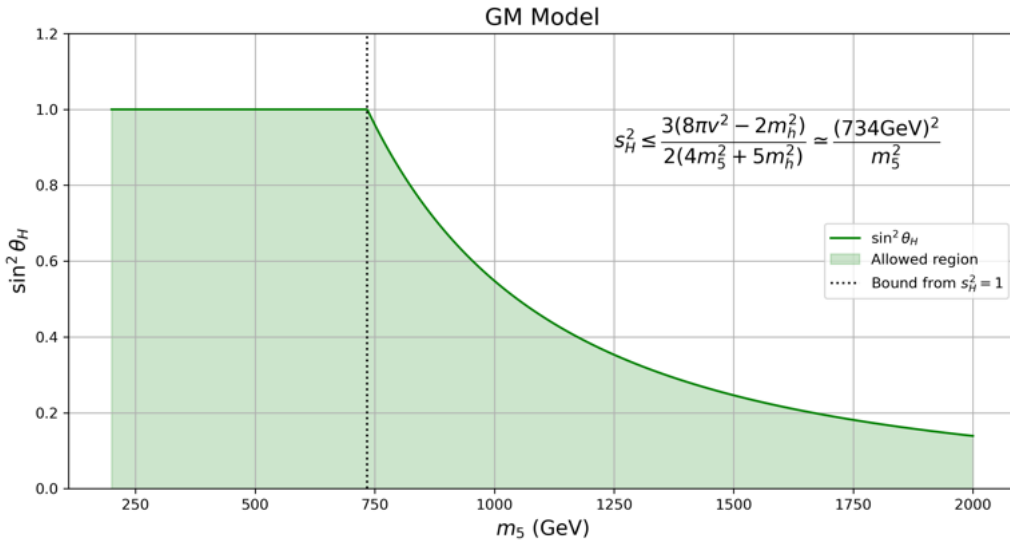


Figure 3.5.: **Georgi–Machacek model: mass bound for H_5^{++} .** Constraint derived from the custodial-sum rule of Eq. (3.16) and the s -wave unitarity condition in sec. 3.4; bound shown as a function of $\kappa_{WW}^{H_5^{++}}$ and m_5 .

In Fig. 3.5, the GM bound appears as the allowed region in the (m_5, s_H^2) plane and depicts the mass bound that we derived in Equation 3.29. The plot follows the analytic behaviour $s_H^2 \propto 1/m_5^2$; as $m_5 \rightarrow \infty$ (i.e. $\kappa_{WW}^{H_5^{++}} \rightarrow 0$) we have $s_H \rightarrow 0$.

3.4.4. Scalar Septet Model

In the septet model, additional doubly-charged scalars H^{++} modify the sum rule to:

$$(\kappa_V^h)_{\max}^2 = 1 + (\kappa_{WW}^{H^{++}})^2, \quad (3.30)$$

Now following a similar procedure and applying the unitary condition to the Equation 3.11, we obtain the mass bound as [17]

$$(\kappa_{WW}^{H^{++}})^2 \leq \frac{8\pi v^2 - 2m_h^2}{m_{H^{++}}^2 + 2m_h^2}. \quad (3.31)$$

This yields an upper bound on the septet vev parameter s_7 [17]:

$$s_7^2 \leq \frac{1}{15} \frac{8\pi v^2 - 2m_h^2}{m_{H^{++}}^2 + 2m_h^2} \simeq \left(\frac{260 \text{ GeV}}{m_{H^{++}}} \right)^2, \quad (3.32)$$

which scales as $1/m_{H^{++}}^2$ for large $m_{H^{++}}$, demonstrating the decoupling behavior of the septet vev.

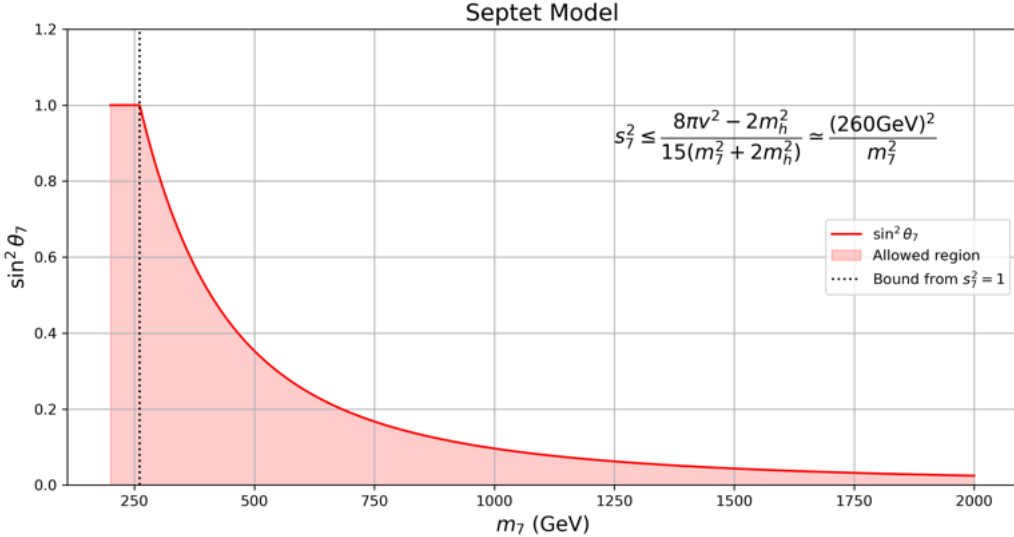


Figure 3.6.: **Septet model: mass bound for H^{++} .** Constraint obtained using the septet unitarity relation in sec. 3.4 (see the H^{++} bound) and expressed in terms of $\kappa_{WW}^{H^{++}}$ versus $m_{H^{++}}$.

Similarly, Fig. 3.6 shows the Septet mass bound in the (m_7, s_7^2) plane. The unitarity relation (Eq. 3.32) again shows a trend similar to that in GM and 2HDM as $s_7^2 \propto 1/m_7^2$. Thus, for $m_7 \rightarrow \infty$ (equivalently $\kappa_{WW}^{H^{++}} \rightarrow 0$) the septet contribution decouples [17].

4. Comparative Analysis of Extended Higgs Sectors and Experimental Limits

This chapter provides a comparative analysis of the extended Higgs sectors considered in the thesis: the 2HDM, the GM model, and the scalar Septet model. The following sections highlight the similarities and key differences in the models, including the field content, the physical spectrum, that govern their Higgs and vector–boson couplings κ_V , and the unitarity sum rules derived in Chapter 3. We shall also compare the sum rules and mass bounds obtained in the last chapter.

We will then investigate the experimental limits on SM like Higgs–vector boson coupling that we obtain from the CMS Collaborative report published in 2023 [20], in particular the CMS global fit $\kappa_V = 1.02 \pm 0.08$. Using these bounds, we try to get 2σ experimental bounds on the other physical heavy Higgs states from our extended Higgs models including the heavy neutral (H^0) and the doubly charged Higgs state (H^{++}). Finally, we try to obtain further constraints on the mixing angles and the mass bounds.

4.1. Comparative Analysis of extended Higgs models

4.1.1. Field Content and Physical Spectrum

The scalar multiplets of the three models extend the SM Higgs doublet by additional representations under $SU(2)_L \times U(1)_Y$. Their decomposition after electroweak symmetry breaking leads to distinct physical states, including additional neutral, charged, and, in some cases, doubly charged scalars. Table 4.1 compares the field content and the vev structures for the models as discussed in detail in chapter 2.

Despite their differences, all three models respect custodial symmetry such that the dangerous $\mathcal{O}(E^2)$ growth in $V_L V_L$ scattering is cancelled once the following unitarity sum rules hold:

$$2\text{HDM}: (\kappa_{VV}^{h^0})^2 + (\kappa_{VV}^{H^0})^2 = 1, \quad (4.1)$$

$$\text{GM}: (\kappa_{VV}^{h^0})^2 + (\kappa_{VV}^{H^0})^2 + (\kappa_{VV}^{H_5^0})^2 - (\kappa_{WW}^{H_5^{++}})^2 = 1, \quad (4.2)$$

$$\text{Septet}: (\kappa_{VV}^h)^2 + (\kappa_{VV}^H)^2 - (\kappa_{WW}^{H^{++}})^2 = 1. \quad (4.3)$$

These relations ensure perturbative unitarity of longitudinal vector-boson scattering in the respective models.

4.1.2. VEV Structure and Mixing Angles

The decomposition of the electroweak scale $v \simeq 246$ GeV into doublet and extended multiplet representations differs in each model, leading to different mixing angles and coupling relations:

$$\text{2HDM: } v^2 = v_1^2 + v_2^2, \quad \tan \beta = \frac{v_2}{v_1}, \quad (4.4)$$

$$\text{GM: } v^2 = v_\phi^2 + 8v_\chi^2, \quad c_H = \frac{v_\phi}{v}, \quad s_H = \frac{2\sqrt{2}v_\chi}{v}, \quad (4.5)$$

$$\text{Septet: } v^2 = v_\phi^2 + 16v_\chi^2, \quad c_7 = \frac{v_\phi}{v}, \quad s_7 = \frac{4v_\chi}{v}. \quad (4.6)$$

In each case, the extended multiplet vev v_χ vanishes in the decoupling limit $v_\phi \rightarrow v$, recovering the SM Higgs sector with $\kappa_V^H = 1$. Increasing v_χ , on the other hand, enhances the couplings of custodial fiveplet states in GM or the doubly charged H^{++} in the Septet model.

Model	Field content	VEV structure	$\tan(\beta, \theta_H, \theta_7)$
2HDM	$\Phi_1 = \begin{pmatrix} \phi_1^+ \\ \phi_1^0 \end{pmatrix}, \Phi_2 = \begin{pmatrix} \phi_2^+ \\ \phi_2^0 \end{pmatrix}$	$v^2 = v_1^2 + v_2^2$	$\tan \beta = \frac{v_2}{v_1}$
GM	$\Phi = \begin{pmatrix} \phi^+ \\ \phi^0 \end{pmatrix}, \chi = \begin{pmatrix} \chi^{++} \\ \chi^+ \\ \chi^0 \end{pmatrix}, \xi = \begin{pmatrix} \xi^+ \\ \xi^0 \\ \xi^- \end{pmatrix}$	$v^2 = v_\phi^2 + 8v_\chi^2$	$\tan \theta_H = \frac{2\sqrt{2}v_\chi}{v_\phi}$
Septet	$\Phi = \begin{pmatrix} \phi^+ \\ \phi^0 \end{pmatrix}, X = \begin{pmatrix} \chi^{+5} \\ \chi^{+4} \\ \chi^{+3} \\ \chi^{+2} \\ \chi_1^{+1} \\ \chi^0 \\ \chi_2^{-1} \end{pmatrix}$	$v^2 = v_\phi^2 + 16v_\chi^2$	$\tan \theta_7 = \frac{4v_\chi}{v_\phi}$

Table 4.1.: Model comparison for field content and vev structure for the 2HDM, GM, and Septet models.

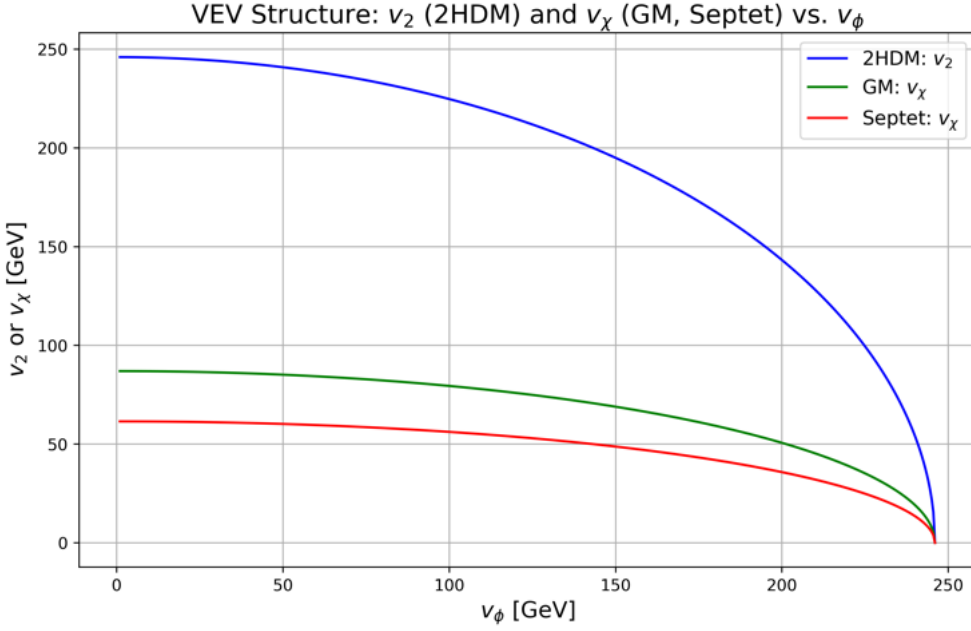


Figure 4.1.: Vev structure in the three models: v_2 (2HDM), v_χ (GM), and v_χ (Septet) as functions of the SM-like doublet VEV v_ϕ . The relations $v^2 = v_1^2 + v_2^2$, $v^2 = v_\phi^2 + 8v_\chi^2$, and $v^2 = v_\phi^2 + 16v_\chi^2$ illustrates how extended multiplet contributions decouple as $v_\phi \rightarrow v$.

4.1.3. Higgs and Vector Boson Effective Couplings and Sum Rules

We now consider the Higgs and vector-boson effective couplings that are relevant for the longitudinal vector-boson scattering amplitudes, especially the WW scattering process, and we compare said effective couplings for each model. The Table 4.2 contains the different Higgs state effective couplings for the 3 models including the CP-even neutral and doubly charged states.

Feature	2HDM	GM	Septet
$\kappa_V^{h^0}$	$\sin(\beta - \alpha)$	$c_H c_\alpha - \sqrt{\frac{8}{3}} s_H s_\alpha$	$c_7 c_\alpha - 4 s_7 s_\alpha$
$\kappa_V^{H^0}$	$\cos(\beta - \alpha)$	$c_H s_\alpha + \sqrt{\frac{8}{3}} s_H c_\alpha$	$c_7 s_\alpha + 4 s_7 c_\alpha$
Additional effective couplings	—	$\kappa_{VV}^{H_5^0} = \frac{1}{\sqrt{3}} s_H$, $\kappa_{WW}^{H_5^{++}} = \sqrt{2} s_H$	$\kappa_{WW}^{H^{++}} = \sqrt{15} s_7$

Table 4.2.: Effective Higgs–vector–boson couplings grouped by model. Here $V = W, Z$.

In the following Figures 4.2–4.4, we plot the effective coupling vs mixing angle plots, where we fix the CP–even mixing angle to $\alpha = \pi/4$ and scan the mixing angles β , θ_H , and θ_7 for 2HDM, GM and Septet, respectively, as

$$\beta \in [-\frac{\pi}{2}, \frac{\pi}{2}], \quad \theta_H \in [-\frac{\pi}{2}, \frac{\pi}{2}], \quad \theta_7 \in [-\frac{\pi}{2}, \frac{\pi}{2}].$$

We fix the alpha value for the following plots to see the behaviour of the effective coupling with the

above-mentioned mixing angles. So, this is only a specific case, and we see similar trends for other angles; plots for these can be found in the appendix. F

The colored curves show the effective couplings κ as functions of the corresponding mixing angle. We also plot the sum rule in the plots to show that the sum rule remains one (Eqs. 4.1 - 4.3) for all mixing angle values.

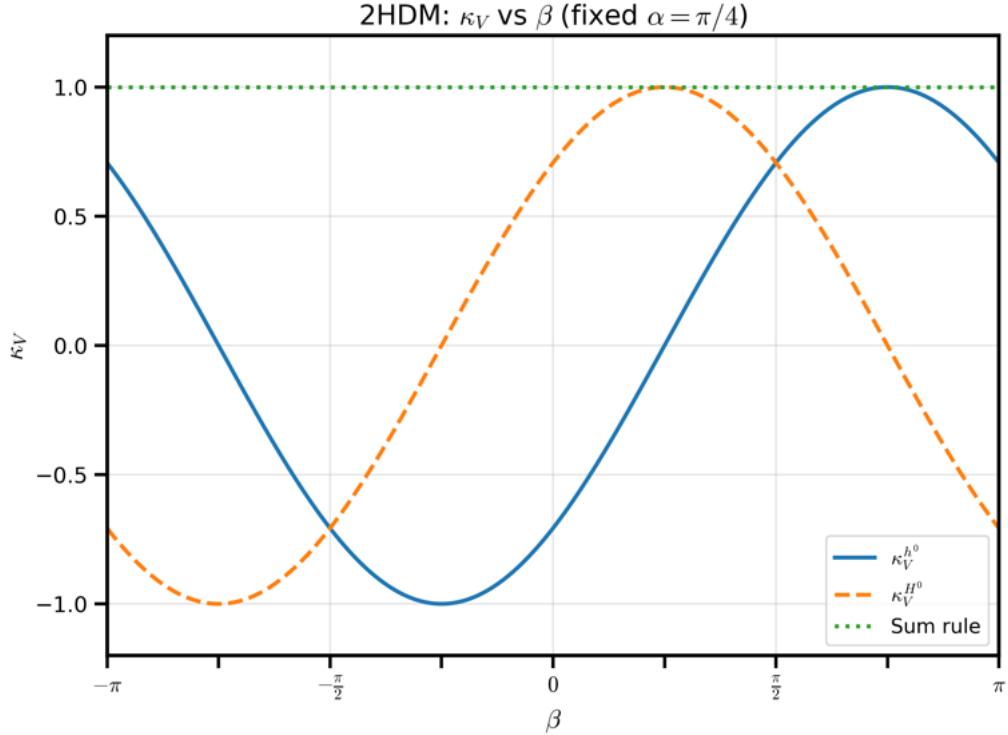


Figure 4.2.: 2HDM effective couplings $\kappa_{VV}^{h^0}$ and $\kappa_{VV}^{H^0}$ versus β at fixed $\alpha = \pi/4$. The green dotted curve shows $(\kappa_{VV}^{h^0})^2 + (\kappa_{VV}^{H^0})^2$.

In Figures 4.2 – 4.4, we plot the effective Higgs–vector–boson couplings as functions of the mixing angles with the CP–even mixing angle fixed to $\alpha = \pi/4$. The analytical relations are taken from Table 4.2 and the unitarity relations discussed in Chapter 3 (see also Refs. [13, 17]).

In 2HDM (Fig. 4.2), at $\alpha = \pi/4$ the effective couplings reduce to

$$\kappa_V^{h^0} = \sin(\beta - \frac{\pi}{4}), \quad \kappa_V^{H^0} = \cos(\beta - \frac{\pi}{4}). \quad (4.7)$$

During the scan $\beta \in [-1.6, 1.6]$ the curve for $\kappa_V^{h^0}$ increases as $\kappa_V^{H^0}$ decreases in a complementary way, as is evident by their coupling structures. The sum rule, $\kappa_V(h^0)^2 + \kappa_V(H^0)^2 = 1$, is also maintained as seen in the horizontal dotted line in Fig. 4.2. This symmetric behaviour reflects the presence of two doublets in the 2HDM.

In the Georgi–Machacek model (Fig. 4.3), using $c_H \equiv \cos \theta_H$ and $s_H \equiv \sin \theta_H$, the CP–even singlet couplings at $\alpha = \pi/4$ become

$$\kappa_V^{h^0} = \frac{c_H - \sqrt{\frac{8}{3}}s_H}{\sqrt{2}}, \quad \kappa_V^{H^0} = \frac{c_H + \sqrt{\frac{8}{3}}s_H}{\sqrt{2}}. \quad (4.8)$$

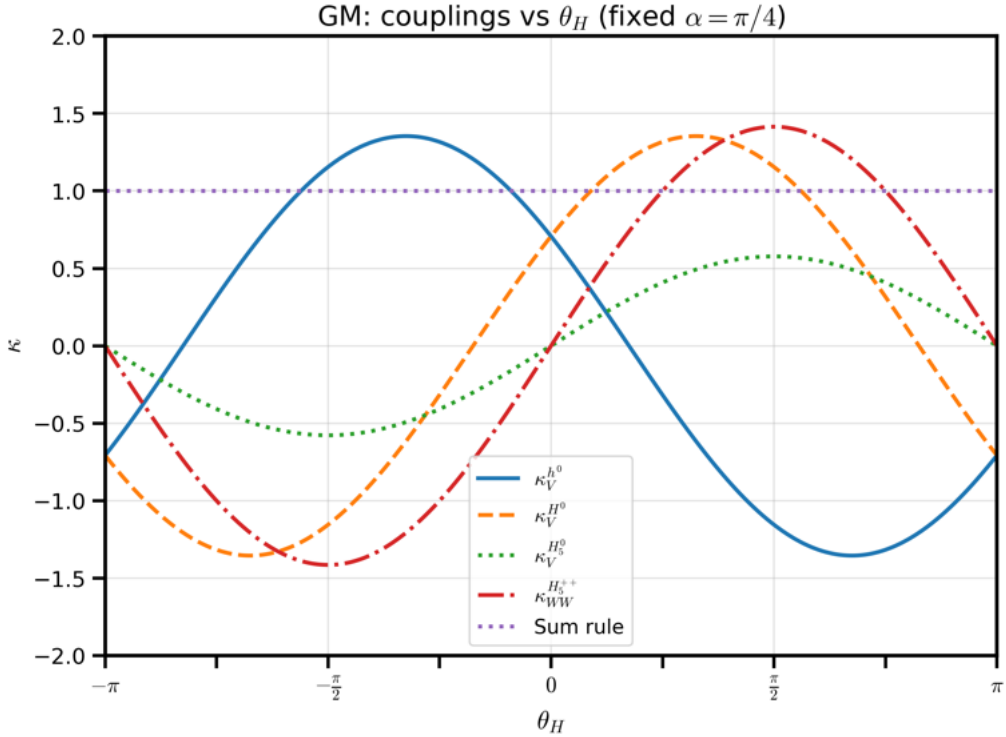


Figure 4.3.: GM effective couplings versus θ_H at fixed $\alpha = \pi/4$ with effective couplings $\kappa_{VV}^{h^0}$, $\kappa_{VV}^{H^0}$, $\kappa_{VV}^{H_5^0}$, and $\kappa_{WW}^{H_5^{++}}$. The purple dotted curve shows the GM sum-rule $(\kappa_{VV}^{h^0})^2 + (\kappa_{VV}^{H^0})^2 + (\kappa_{VV}^{H_5^0})^2 - (\kappa_{WW}^{H_5^{++}})^2$.

The presence of the numerical weight $\sqrt{8/3}$ in the effective coupling relations (see Table 4.2), $\kappa_V^{h^0}$ decreases as θ_H moves away from zero, while $\kappa_V^{H^0}$ increases. The other neutral and doubly charged Higgs states grow linearly with s_H ,

$$\kappa_V^{H_5^0} = \frac{s_H}{\sqrt{3}}, \quad \kappa_{WW}^{H_5^{++}} = \sqrt{2}s_H, \quad (4.9)$$

which explains the rising green and red curves. The purple dotted line reflects the sum rule and remains constant at 1, where the unitarity sum rule is given by

$$(\kappa_{VV}^{h^0})^2 + (\kappa_{VV}^{H^0})^2 + (\kappa_{VV}^{H_5^0})^2 - (\kappa_{WW}^{H_5^{++}})^2 = 1.$$

as derived in Chapter 3.

In the Septet model (Fig. 4.4), where $c_7 \equiv \cos \theta_7$ and $s_7 \equiv \sin \theta_7$, the CP-even couplings at $\alpha = \pi/4$ become

$$\kappa_{VV}^{h^0} = \frac{c_7 - 4s_7}{\sqrt{2}}, \quad \kappa_{VV}^{H^0} = \frac{c_7 + 4s_7}{\sqrt{2}}, \quad (4.10)$$

and the doubly charged coupling is

$$\kappa_{WW}^{H_5^{++}} = \sqrt{15}s_7. \quad (4.11)$$

The coefficient 4 in the neutral couplings (Table 4.2) alters the behaviour of the septet couplings relative to the 2HDM. $\kappa_{VV}^{h^0}$ decreases with increasing θ_7 while $\kappa_{VV}^{H^0}$ increases, and the $\kappa_{WW}^{H_5^{++}}$ curve

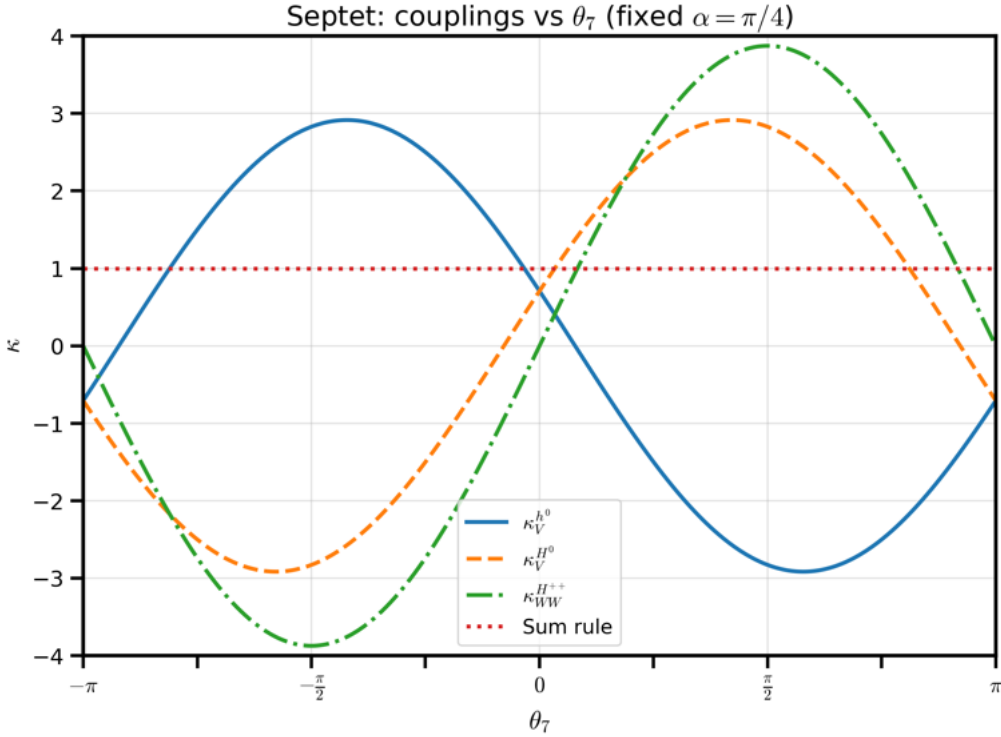


Figure 4.4.: Septet effective couplings versus θ_7 at fixed $\alpha = \pi/4$: $\kappa_{VV}^{h^0}$, $\kappa_{VV}^{H^0}$, and $\kappa_{WW}^{H^{++}}$. The red dotted curve shows the Septet sum-rule $(\kappa_{VV}^h)^2 + (\kappa_{VV}^H)^2 - (\kappa_{WW}^{H^{++}})^2$.

increases linearly with s_7 . The dotted line again sits at 1, confirming the Septet sum rule

$$(\kappa_V^{h^0})^2 + (\kappa_V^H)^2 - (\kappa_{WW}^{H^{++}})^2 = 1.$$

4.2. Experimental limits on extended Higgs models

In the following section, we will obtain constraints on effective Higgs-vector boson couplings for our models with the CMS [20] data in the κ -framework. In this framework, the coupling strength modifiers for production and decay are expressed in terms of rescalings of SM couplings and for electroweak gauge bosons and are defined such that the cross section (σ_i) and branching ratios (Γ^f) scale as κ^2 .

$$\kappa_V^2 = \frac{\Gamma(H \rightarrow VV)^{\text{BSM}}}{\Gamma(H \rightarrow VV)^{\text{SM}}} \cdot \frac{\sigma(X \rightarrow VV)^{\text{BSM}}}{\sigma(X \rightarrow VV)^{\text{SM}}},$$

where, X in the cross section represents the production mode which depends on the channels under consideration in CMS/ATLAS we refer to. The production and decay modes will be discussed in detail in section 5.5. Hence, we can refer to κ (the coupling strength modifier) as discussed in the main reference paper to the effective coupling in our analysis.

The CMS Run-2 global fit to the Higgs boson couplings [20] reports¹

$$\kappa_V^{obs} = 1.02 \pm 0.08 \quad \Rightarrow \quad \kappa_V^{obs} \in [0.86, 1.18] \text{ (95% CL).} \quad (4.12)$$

We assume $\kappa_V \equiv \kappa_W \simeq \kappa_Z$ ². This interval gives us the 2σ bound on the light Higgs coupling modifier (or effective coupling in our notation) and is taken as the experimental target for the 125 GeV Higgs identified in our models with the light CP-even scalar (h^0 in 2HDM, GM and Septet).

Using these limits, we calculate the 2σ ranges for the effective couplings of the heavier Higgs states including H^0 for the 2HDM, H^0, H^{++} for the septet model and H^0, H_5^{++} for the GM model. Additionally, we obtain mass limits for the heavier states (H^0).

4.3. Effective Couplings of heavy Higgs States Constrained by $\kappa_V^{h^0}$

We now discuss the analysis for the mixing-angle scans by the CMS global fit to the Higgs-vector-boson effective coupling of the observed state h^0 , $\kappa_V^{h^0} = 1.02 \pm 0.08$, which we use as the 2σ interval $0.86 \leq \kappa_V^{h^0} \leq 1.18$ [20].

4.3.1. Heat maps for $\kappa_V^{h^0}$ and 2σ constraint

We plot the heat maps for the effective coupling $\kappa_V^{h^0}$ as a function of the mixing angles as shown below and then plot the 2σ bounds on the heatmap.

Quantity	Symbol	Range / Value
CP-even mixing angle	α	$[-\pi, \pi]$
2HDM angle	β	$[-\pi, \pi]$
GM angle	θ_H	$[-\pi, \pi]$
Septet angle	θ_7	$[-\pi, \pi]$

Table 4.3.: Mixing angle set for all heatmaps as a grids in $(\alpha, \beta / \theta_H / \theta_7)$.

The heat maps in Figures 4.5, 4.6 and 4.7, show the effective coupling of the observed state, $\kappa_V^{h^0}$, across all $(\beta / \theta_H / \theta_7, \alpha)$ domains for the three models: 2HDM (β, α), GM (θ_H, α), and Septet (θ_7, α). The colour encodes the value of $\kappa_V^{h^0}$; analytic forms are given in Table 4.2.

To impose the experimental constraint of the CMS global fit, $\kappa_V^{h^0} = 1.02 \pm 0.08$, we overlay three contours at $\{0.86, 1.02, 1.18\}$ corresponding to the 2σ lower, central, and upper values. The allowed band is then the set

$$\mathcal{R}_{h^0} = \{(\Theta, \alpha) : 0.86 \leq \kappa_V^{h^0}(\Theta, \alpha) \leq 1.18\}, \quad (4.13)$$

¹We use the κ limits from CMS for W-boson gauge couplings.

²In the paper mentioned, $\kappa_Z = 1.04 \pm 0.07$, and hence we assume, $\kappa_V \equiv \kappa_W \simeq \kappa_Z$

with $\Theta \in \{\beta, \theta_H, \theta_7\}$ depending on the model. This region \mathcal{R}_{h^0} is used as a mask on the heavy-state coupling heatmap to extract the allowed ranges quoted in Table 4.4 and visualized in Figures 4.8 – 4.11b.

For each model, we produce a filled contour of the heavy Higgs state effective coupling ($\kappa_{VV}^{H^0}$ or $\kappa_{WW}^{H^{++}}$) on the (mixing angle, α) plane. We then superimpose the three $\kappa_V^{h^0}$ contours $\{0.86, 1.02, 1.18\}$ as {white dashed, black, white dashed}. The allowed 2σ interval for the heavy Higgs effective coupling is read from the colorbar but only over the points that satisfy $0.86 \leq \kappa_V^{h^0} \leq 1.18$. From the above plots, we also obtain α and $(\beta, \theta_H, \theta_7)$ combinations that lie within the 2σ interval. In the 2HDM heatmap for $\kappa_V^{h^0}$ constrained by 2σ experimental limits, $\kappa_V^{h^0} = \sin(\beta - \alpha)$ produces diagonal stripes of constant value. In the heat maps of the GM and the Septet model, we see quadrants of yellow and blue areas due to the triplet and septet weight of $\sqrt{8/3}$ and 4, respectively, in $\kappa_V^{h^0}$ in the (θ_H, α) ((θ_7, α)) plane. These mixing angle combinations serve as input values for our `HiggsTools` analysis, which we will discuss in the next chapter 5.

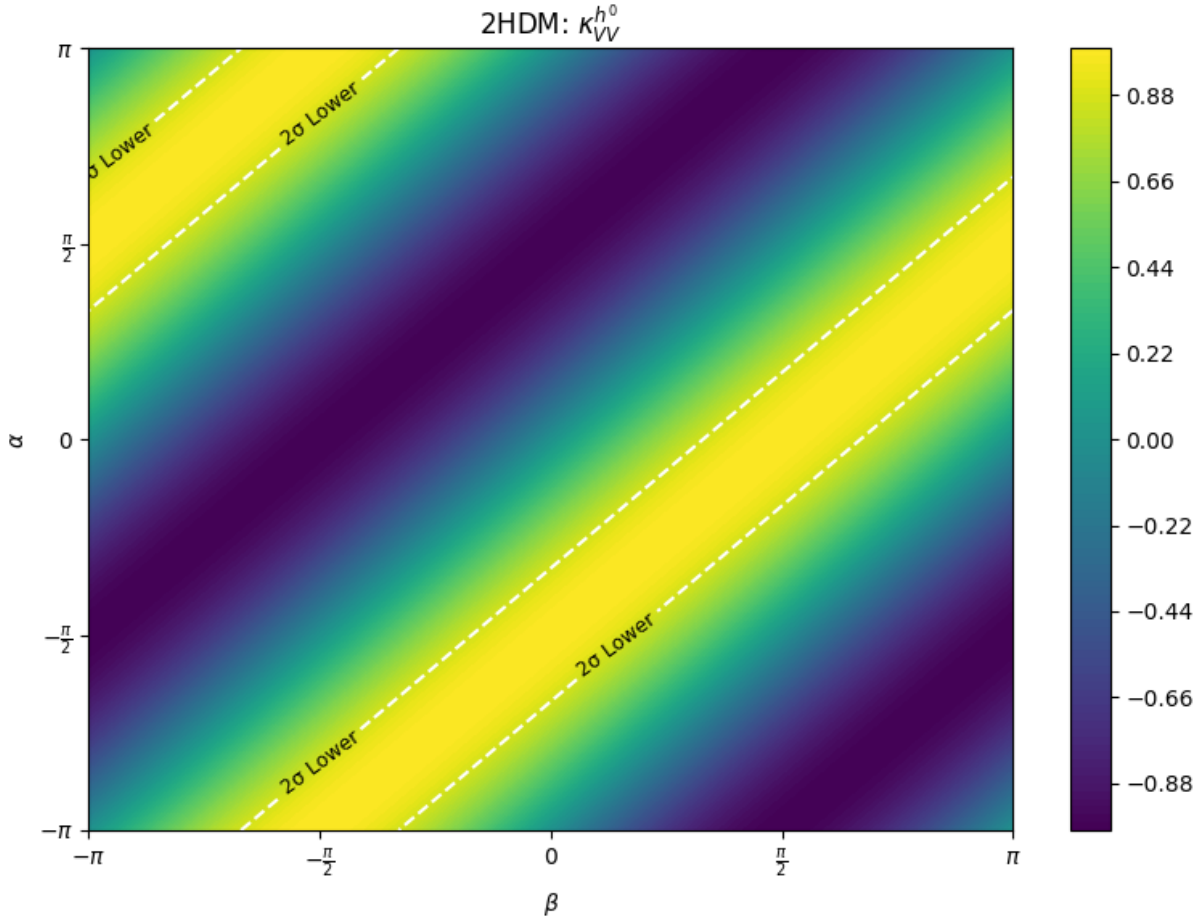


Figure 4.5.: 2HDM heat map in the (β, α) plane. The white dashed lines mark the 2σ edges of $0.86 \leq \kappa_V^{h^0} \leq 1.18$; the black line is absent because the best-fit value is $\kappa_V^{h^0} = 1.02$, which lies outside the 2HDM $\kappa_V^{h^0}$ range.³ Mixing-angle scan ranges are given in Table 4.3.

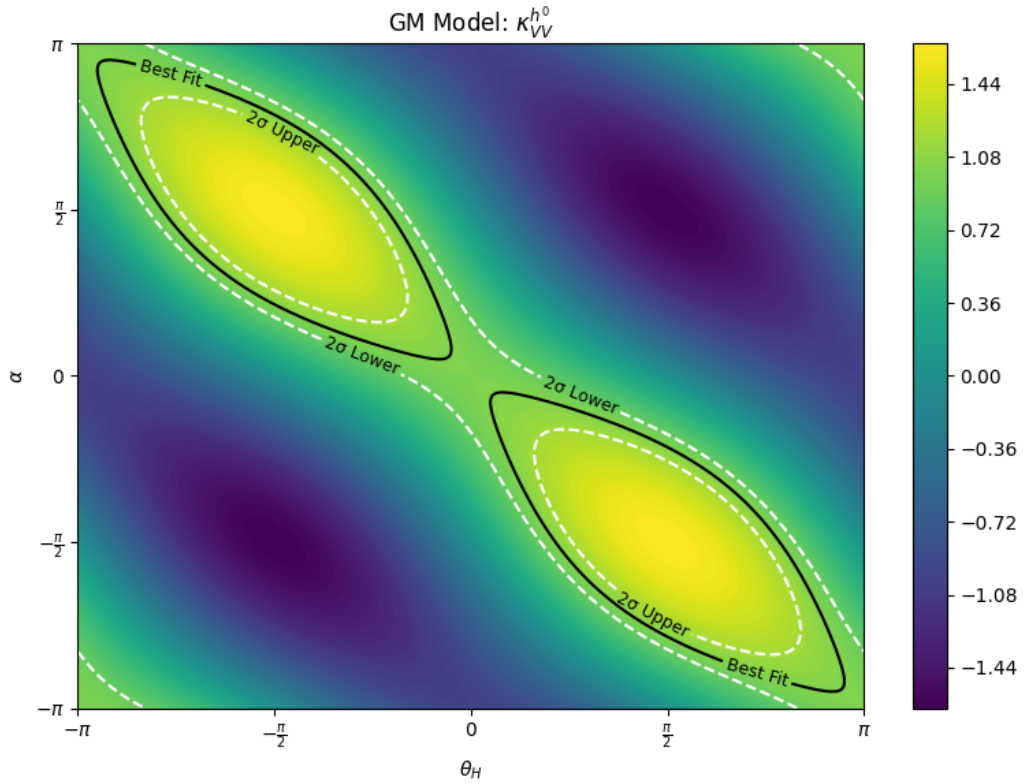


Figure 4.6.: GM heat map in the (θ_H, α) plane with the same 2σ and best-fit conventions as mentioned in the caption of Fig. 4.5.

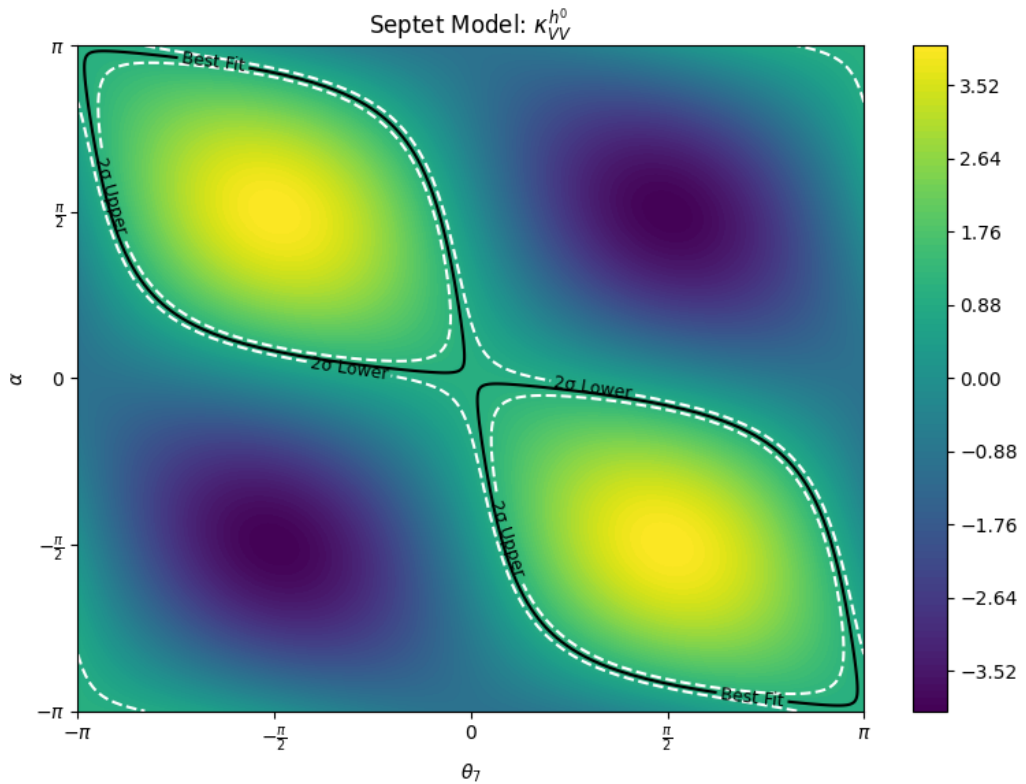


Figure 4.7.: Septet heat map in the (θ_7, α) plane with the same 2σ and best-fit conventions as in Fig. 4.5.

4.3.2. Heat maps for $\kappa_V^{H^0}$ constrained by the 2σ $\kappa_V^{h^0}$ Experimental Limits

In the 2HDM heatmap for $\kappa_V^{H^0}$, constrained by the $\kappa_V^{h^0}$ limits, as shown in Fig. 4.8, $\kappa_V^{H^0} = \cos(\beta - \alpha)$ produces diagonal stripes, similar to the $\kappa_V^{h^0}$ heat maps above. We observe similar patterns for the GM and Septet models due to the representation weights; the allowed region forms parallel stripes in (mixing angles $(\beta, \theta_H, \theta_7)$, α) and the heavy coupling is confined to a narrow range.

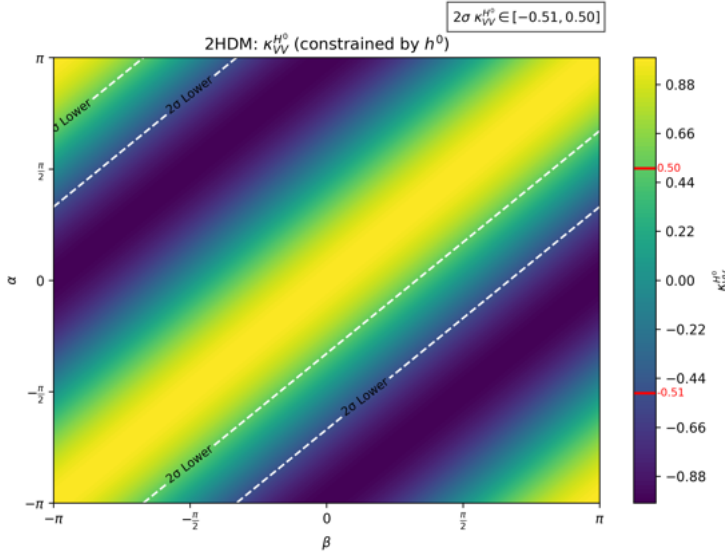


Figure 4.8.: 2HDM: Heatmap for $\kappa_V^{H^0}(\beta, \alpha)$.

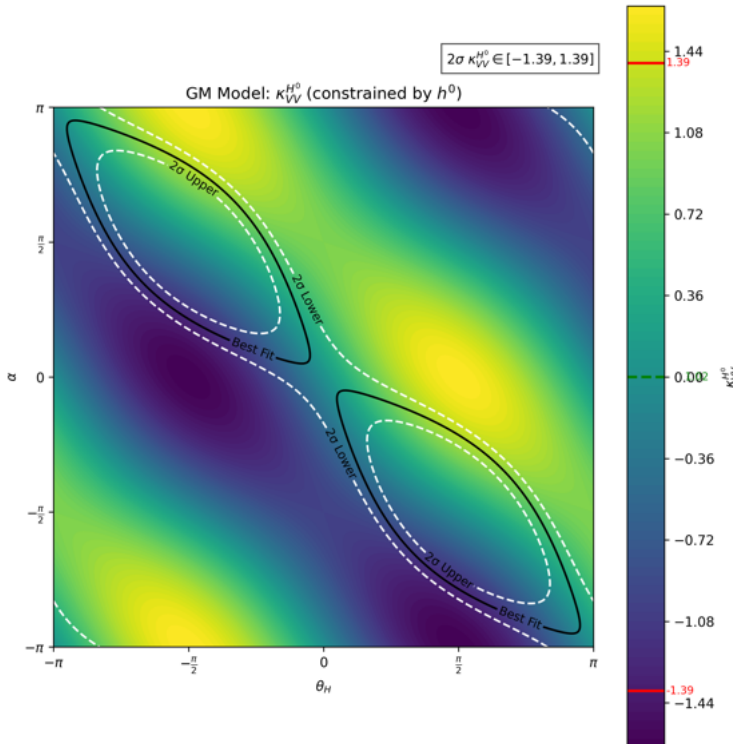


Figure 4.9.: GM: Heatmap for $\kappa_{VV}^{H^0}(\theta_H, \alpha)$.

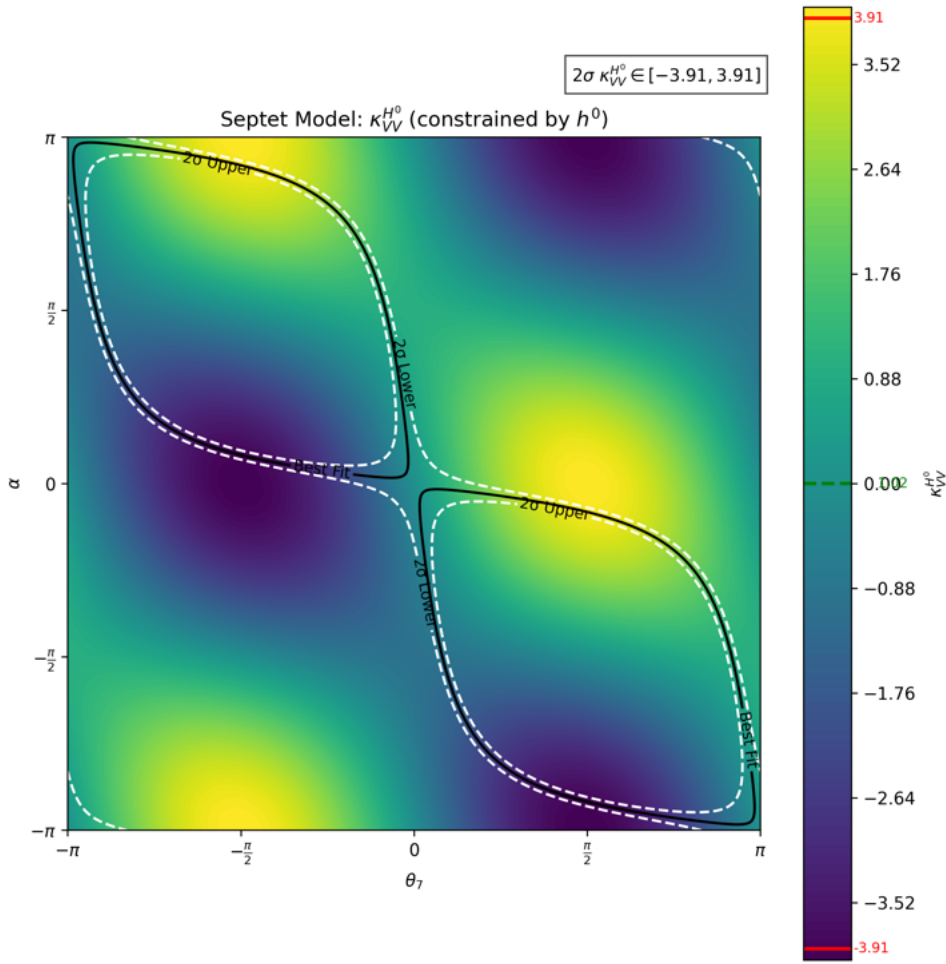


Figure 4.10.: Septet: Heatmap for $\kappa_V^{H^0}(\theta_7, \alpha)$.

4.3.3. Heat maps for $\kappa_{WW}^{H^{++}}$ constrained by the 2σ $\kappa_V^{h^0}$ experimental limits

For the doubly charged states, we impose the same 2σ band on the light Higgs effective coupling, $0.86 \leq \kappa_V^{h^0} \leq 1.18$, and display the resulting allowed regions for the effective couplings to vector bosons:

$$\begin{aligned} \text{GM: } \kappa_{WW}^{H_5^{++}} &= \sqrt{2} \sin \theta_H \quad (\alpha\text{-independent}), \\ \text{Septet: } \kappa_{WW}^{H^{++}} &= \sqrt{15} \sin \theta_7. \end{aligned}$$

In the GM model, the heat map exhibits vertical structure in (θ_H, α) because $\kappa_{WW}^{H_5^{++}}$ does not depend on α . In the Septet model, we observe a similar vertical structure due to only the θ_7 dependence.

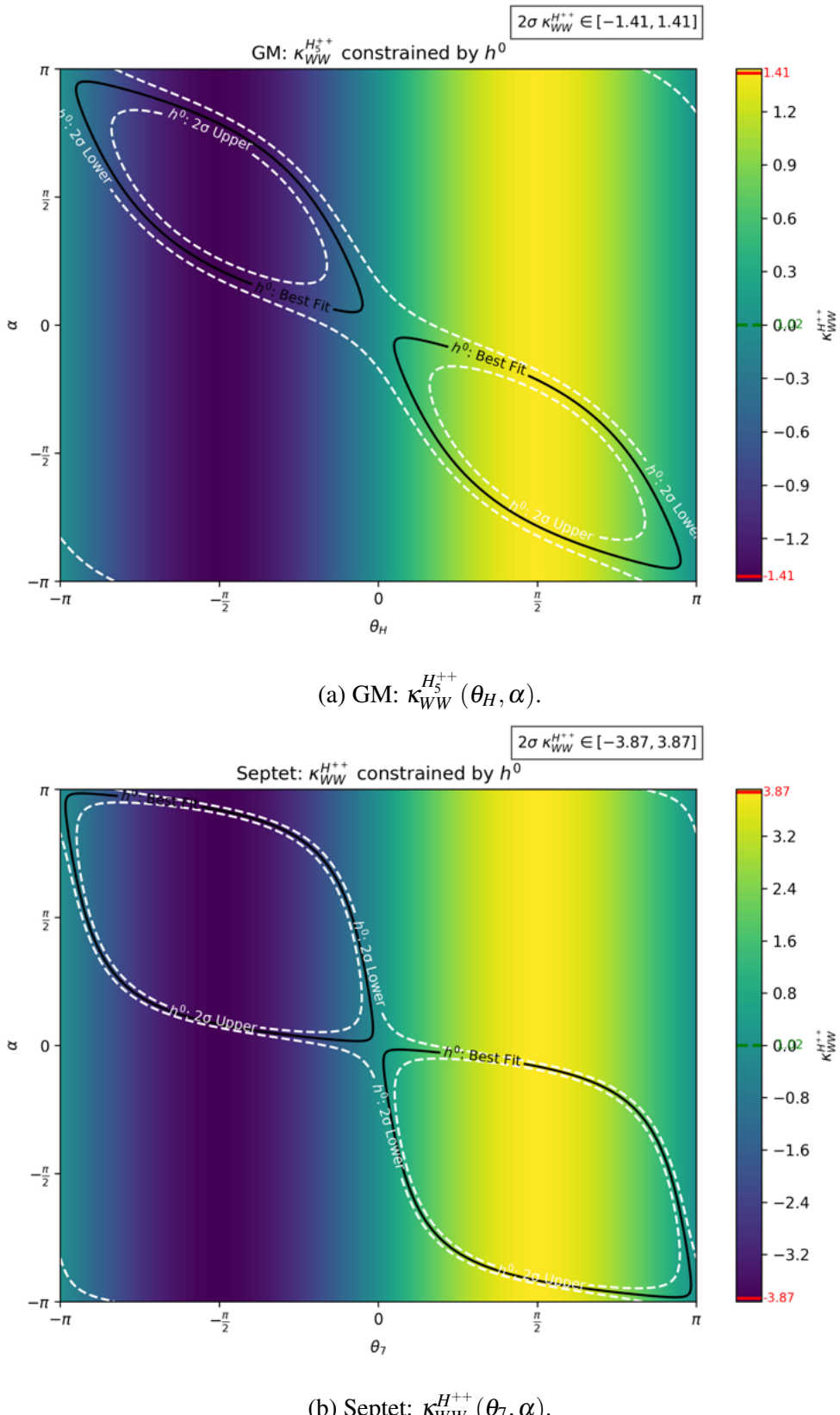


Figure 4.11.: Doubly charged effective-coupling maps constrained by the 2σ $\kappa_V^{h^0}$ constrained by $0.86 \leq \kappa_V^{h^0} \leq 1.18$.

4.3.4. Numerical 2σ intervals for effective couplings for all Higgs states for the extended Higgs models

The coupling intervals from the colorbars (restricted to the masked regions satisfying $0.86 \leq \kappa_V^{h^0} \leq 1.18$) are collected below, and a dash denotes the couplings being absent in that model.

Model	$\kappa_V^{h^0} (2\sigma)$	$\kappa_V^{H^0} (2\sigma)$	$\kappa_{WW}^{H^{++}} (2\sigma)$
GM	[0.86, 1.18]	[-1.39, 1.39]	[-1.41, 1.41]
Septet	[0.86, 1.18]	[-3.91, 3.91]	[-3.87, 3.87]
2HDM	[0.86, 1.18]	[-0.51, 0.50]	—

Table 4.4.: 2σ effective–coupling intervals derived from the CMS band on $\kappa_V^{h^0}$ [20].

In the next chapter, we shall exploit the effective coupling limits, Table 4.4, and obtain cross sections for different decay channel and updated $\kappa_V^{h^0}$ ranges using `HiggsTools`.

5. HiggsTools Framework and Analysis

Strategy

The study of extended Higgs sectors requires systematic confrontation with the wide array of collider data available from LEP, the Tevatron, and the LHC. Direct searches for additional scalar resonances and precision measurements of the 125 GeV Higgs boson have produced an extensive and heterogeneous collection of experimental results, each reported in terms of exclusion limits or signal strength fits. A consistent and reliable comparison of theoretical predictions to this data set is not feasible without a dedicated framework that unifies the treatment of exclusion limits and Higgs rate measurements. For this purpose, the tools `HiggsBounds` [32] and `HiggsSignals` [33] were originally developed, providing, respectively, exclusion tests from direct Higgs searches and global fits to Higgs boson signal strengths. Both unified and updated into a single C++ package, `HiggsTools` [34]. This framework not only integrates the functionalities of the original tools but also introduces additional physics features, such as the treatment of non-resonant di-Higgs final states and doubly-charged Higgs searches, while adopting a maintainable and transparent data format. An extension of this thesis is the analysis of the exclusion limits of the doubly charged Higgs boson (H^{++}), for which one would need to provide the cross sections and branching ratio through references mentioned in the `HiggsTools` paper mentioned in Table 2 of reference [34]. Native interfaces for Python and MATHEMATICA complement the C++ core, allowing the framework to be used seamlessly in large-scale phenomenological scans.

Internally, `HiggsTools` is organized into three subpackages with distinct functions [34]. The `HiggsPredictions` module serves as the entry point for the user, where new-physics models are defined by providing the properties of their scalar particles. At a minimum, the mass ranges, total widths, production cross sections, and branching ratios into all relevant final states must be specified and this process needs to be followed for the doubly charged Higgs boson analysis. Alternatively, predictions may be provided via the effective-coupling input mode, where coupling modifiers rescale tabulated Standard Model reference values included in the package, this method is used in our following analysis. The `HiggsBounds` module implements the database of collider search limits and provides the exclusion logic, while `HiggsSignals` performs statistical fits to the signal rates of the observed 125 GeV Higgs boson. We primarily use the `HiggsBounds` and `HiggsPredictions` packages for our analysis.

A key advantage in `HiggsTools` is the use of JSON data files as the format for implemented limits and measurements [34]. Each JSON file corresponds to a specific experimental result and contains the metadata required for reproducibility and consistency checks (including arXiv identifier, collider, integrated luminosity, and search channel), as well as the tabulated observed and expected 95% CL limits. These are parameters that we scan for according to our model specifications. Hence,

a sample HiggsBounds result looks like

HB result 1

```
[ALLOWED] obsRatio 0.749, expRatio: 0.359 for ["H0"] with LHC13
[vbfH,H]>[ZZ] from 1804.01939 (CMS 35.9fb-1, M=(130, 3000),
Gam/M=(0, 0.3))
```

where the obsRatio and expRatio are parameters that HiggsTools calculates to determine the most sensitive channel given a kappa and mass combination.

The arXiv number mentioned corresponds to the research paper(s) which provides the exclusion limit. Hence, for consistency checks, we can compare our results with the corresponding limits provided by the paper. Some examples of such comparisons are discussed in the Appendix G.

5.1. Exclusion Logic and Ratios

In our analysis, the exclusion test is carried out by HiggsBounds by comparing the model prediction for the signal rate with the published 95% CL limits of the corresponding experimental analyses. For each parameter point, we compute the theoretical rate $(\sigma \times BR)_{\text{theory}}$ from the model and compare it to the observed and expected limits supplied in the HiggsTools datafiles for that analysis [34]. The comparison is expressed through

$$\text{obsRatio} \equiv \frac{(\sigma \times BR)_{\text{theory}}}{(\sigma \times BR)_{\text{obs}}^{95\%}}, \quad \text{expRatio} \equiv \frac{(\sigma \times BR)_{\text{theory}}}{(\sigma \times BR)_{\text{exp}}^{95\%}}, \quad (5.1)$$

where the experimental limits in the denominators are mass dependent and are evaluated at the each mass parameter for all channels, which will be discussed in detail in the following sections, and used internally by HiggsBounds for each mass and coupling point [34]. The most sensitive analysis is identified by the largest expected ratio, and the exclusion decision is based on the data, a point is excluded at 95% CL if $\text{obsRatio} > 1$ for each particular point [34].

For consistency checks we also use the corresponding experimental curves. The analysis descriptor returned by HiggsBounds contains the arXiv identifier of the paper that provides the limits; using this reference we discuss a direct comparison between our predicted rates and the published observed/expected limits in Appendix G.

5.2. Parameter Scan Setup

In order to apply these exclusion tests to the models studied in this thesis, model predictions are provided via the Python interface of HiggsPredictions [34]. Each parameter point defines the properties of the heavy neutral scalar H^0 , including its mass m_{H^0} , total width, and effective couplings. As discussed above the production cross sections and branching ratios are supplied either explicitly or via the effective-coupling input mode, and in our analysis we provide the effective couplings obtained

from the 2σ limits as listed in Table 4.4 [34]. The input mixing angles for the three models are obtained from mapping the 2σ bound of $\kappa_V^{h^0}$, hence we obtain α and $\beta/\theta_H/\theta_7$ combinations as input values for our analysis we shown in Figures 4.5, 4.6 and 4.7. This ensures a consistent mapping from the coupling parameters of the model (e.g. $\kappa_V^{H^0}$) to the production and decay processes relevant to the implemented limits.

The heavy scalar mass is varied in the range $m_{H^0} \in [130, 1000]$ GeV with $\Delta m = 20$ GeV,¹ while the coupling modifier to vector bosons is scanned over model-specific ranges as discussed above, and presented below again:

$$\kappa_V^{H^0} \in \begin{cases} [-0.51, 0.50] & \text{2HDM}, \\ [-1.39, 1.39] & \text{Georgi–Machacek}, \\ [-3.91, 3.91] & \text{Septet.} \end{cases}$$

To ensure compatibility with the observed Higgs boson, only mixing angles that reproduce the 2σ range for the SM-like Higgs coupling to vector bosons, $0.86 \leq \kappa_V^{h^0} \leq 1.18$, are retained [20]. For each valid point, we evaluate the cross section times branching ratio for the most sensitive² channel flagged by HiggsBounds in its scan results. The exclusion test itself uses the rate of the *most sensitive* analysis selected by HiggsBounds together with its observed/expected ratios [34]. For comparison in the Appendix, we also reconstruct $(\sigma \times \text{BR})_{\text{obs}}^{95\%}$ and $(\sigma \times \text{BR})_{\text{exp}}^{95\%}$ from these ratios, but these derived limits are not used as primary results, but only serves as a subset of the overall analysis.

5.3. Post-processing and Physics Filters

After the scan, the raw predictions and the outputs from HiggsBounds are saved as CSV files that are used to produce the figures in sec. 5.4. Each row contains the model identifiers(mixing angles, effective coupling values, and mass values) of the heavy Higgs boson, together with the total width, the predicted rates, including the branching ratios and the corresponding channel wise cross sections, and the full set of HiggsBounds diagnostics: the allow/exclude status, the observed and expected ratios, and the descriptor of the most sensitive analysis, including its metadata (collider, luminosity, channel and arXiv identifier) [34]. For quality control, we also retain the predicted $\sigma \times \text{BR}$ values for individual production modes (ggH, VBF, bbH). These mode-specific numbers are used only as internal cross-checks against the *most sensitive* rate selected by HiggsBounds; the exclusion test and all provided results are based on the most sensitive analysis.

Before plotting, we standardize the process names and energy tags so that identical production–decay topologies use a single notation (for example, we write ggH>ZZ and vbfH>WW, ZZ, and we denote the collider energy uniformly as LHC8 or LHC13). The description returned by HiggsBounds for the most sensitive analysis already contains the necessary metadata, which we use to assign these

¹Here $\Delta m = 20$ GeV refers to the mass step size that we have used in our Python scan. One can surely increase the mass step size for more precision.

²The meaning of *most sensitive* is mentioned in section 5.1.

labels consistently. Whenever a theory rate is compared to a limit, it is evaluated at the same collider energy as that limit; mode-specific rates at other energies remain diagnostic only and are not used for exclusion statements.

To ensure physical reliability and numerical stability we apply some set of filters. Points must satisfy the narrow-width approximation, implemented as ³ $\Gamma/M < 0.05$ [35]. We remove points whose most-sensitive $\sigma \times \text{BR}$ falls below a small threshold, as we do get some point with extremely small cross section of the order 10^{-31} pb , so for visual sanity and comparison we plot points till (10^{-6} pb) . These filters are applied consistently across the plotting functions and remove only clearly unphysical or numerically irrelevant values.

5.4. Data Visualization and Analysis

Our goal in this section is to summarize our analysis, using the filtered data set obtained from our HiggsTools analysis. We focus, in the following plots, on which channels are relevant for the allowed and excluded regions, the cross-section ranges associated with those channels as functions of mass and coupling, and hence, we obtain updated ranges of the effective coupling $\kappa_V^{H^0}$. In the following subsections, we present scatter panels, channel-wise plots, $\kappa_V^{H^0}$ versus m_{H^0} scans, and coupling heatmaps.

5.4.1. Scatter Panel for BSM model : $\sigma \times \text{BR}$ vs. $\kappa_V^{H^0}$ (allowed points)

In Figure 5.1, the scatter panels show the predicted $(\sigma \times \text{BR})_{\text{theory}}$ for the allowed points as a function of $\kappa_V^{H^0}$, with color indicating the corresponding most sensitive channel provided by HiggsBounds, see HBResult 1 1. This view highlights the coupling dependence of the allowed and categorized the allowed points to their corresponding channels for a given $\kappa_V^{H^0}$ interval. It is worth noting, that the 2HDM plots seem not continuous compared to the GM and Septet plots, but it is just because of the difference in the kappa intervals and all models are analysed for the kappa ranges, as mentioned in Table 4.4.

³Here Γ is the particle's decay width and M is the mass of the particle.

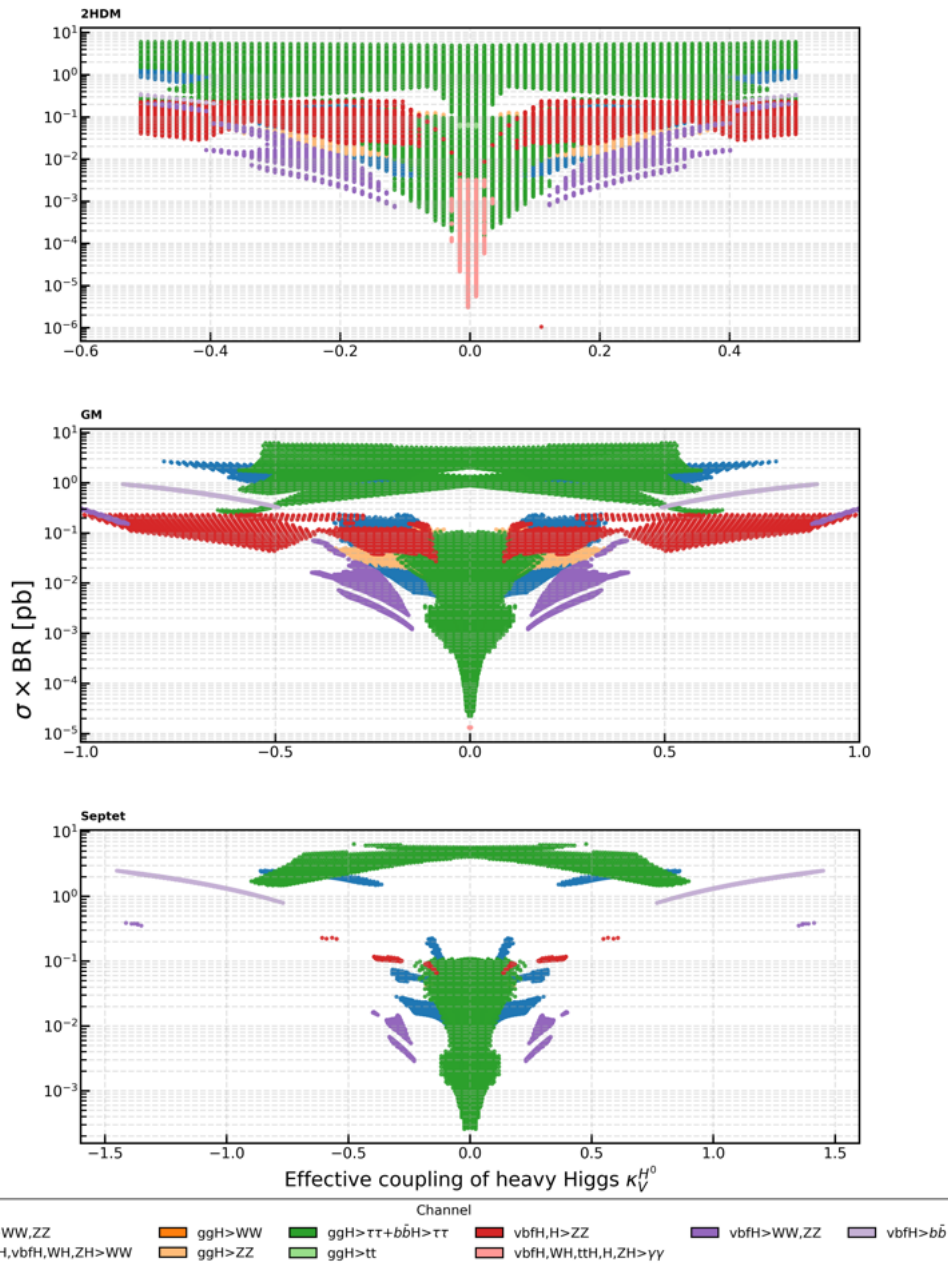


Figure 5.1.: The panel depicts $(\sigma \times \text{BR})_{\text{theory}}$ versus $\kappa_V^{H^0}$ for the 2HDM, GM and Septet model. The colour of the markers are obtained from the most-sensitive channel.

5.4.2. Channel-wise panels: $\sigma \times \text{BR}$ vs. m_{H^0} (allowed points, model-coloured)

In the following panels, Figure 5.2, we show the allowed points as a function of m_{H^0} , as channel-wise scatter plots. Here by "allowed" we mean all the points that were flagged by HiggsTools as `status = allowed`, see HBResult 1. Each panel corresponds to one search channel/topology (for example $H \rightarrow WW, ZZ$ (inclusive), $ggH \rightarrow ZZ$, VBF $\rightarrow WW, ZZ, \tau\tau$, etc.). On each panel we plot all allowed predictions $(\sigma \times \text{BR})_{\text{theory}}$ as a function of the heavy-Higgs mass m_{H^0} and colour the points by **model** (2HDM, GM, Septet). The masses are scanned on a discrete grid and multiple points at the same mass come from different $\kappa_V^{H^0}$ values and thus correspond to different $\sigma \times \text{BR}$,

hence the vertical spread. For channels that only exist in a narrow mass window, see Figure 5.3, in HiggsTools, the x -range is automatically zoomed to the populated region so that the structure is visible instead of being squeezed into the 130–1000 GeV mass range. The figure displays the results for the three models in an inclusive, stacked format. The points corresponding to the 2HDM model are plotted first, which are then overlaid by points from the GM model, and finally the Septet model. This means that any parameter space covered by the Septet model (green) also includes the allowed space for the GM (orange) and 2HDM (blue) models, which lie underneath.

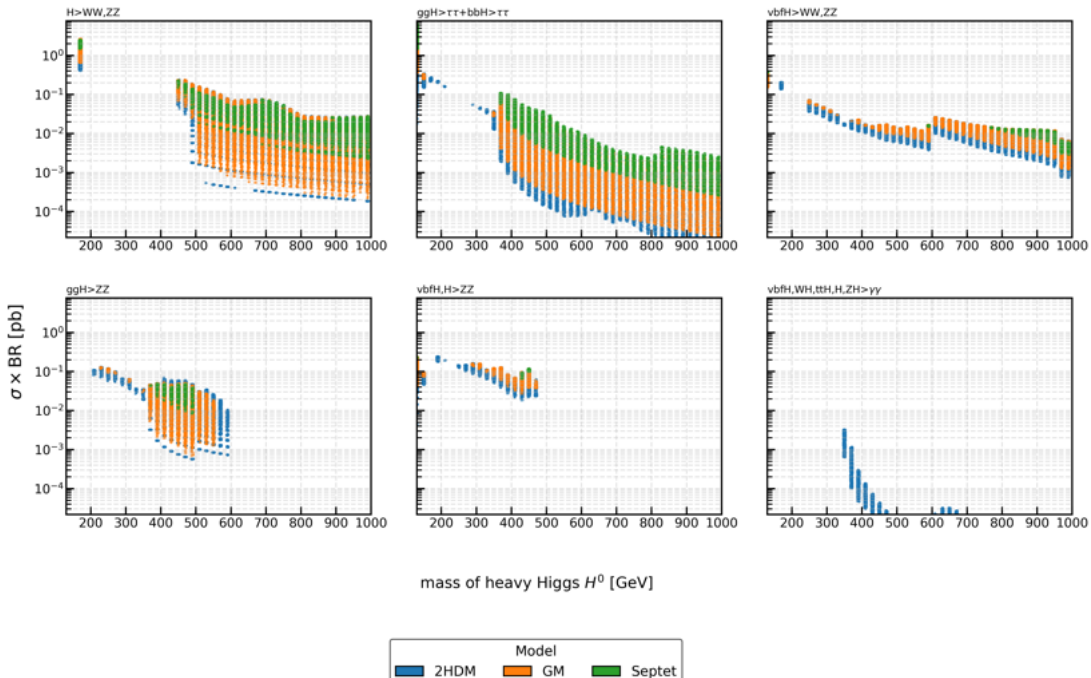


Figure 5.2.: Channel-wise panels with allowed points coloured by model for the most sensitive channels with broad mass coverage: inclusive $H \rightarrow WW, ZZ$, combined $\tau\tau$ ($ggH+bbH$), $VBF \rightarrow WW, ZZ$, $ggH \rightarrow ZZ$, inclusive $H \rightarrow ZZ$, and $\gamma\gamma$. These panels let us directly compare which cross sections remain viable in each channel across the three models, which can be compared to confirm the channel specific ranges, as discussed in Appendix G.

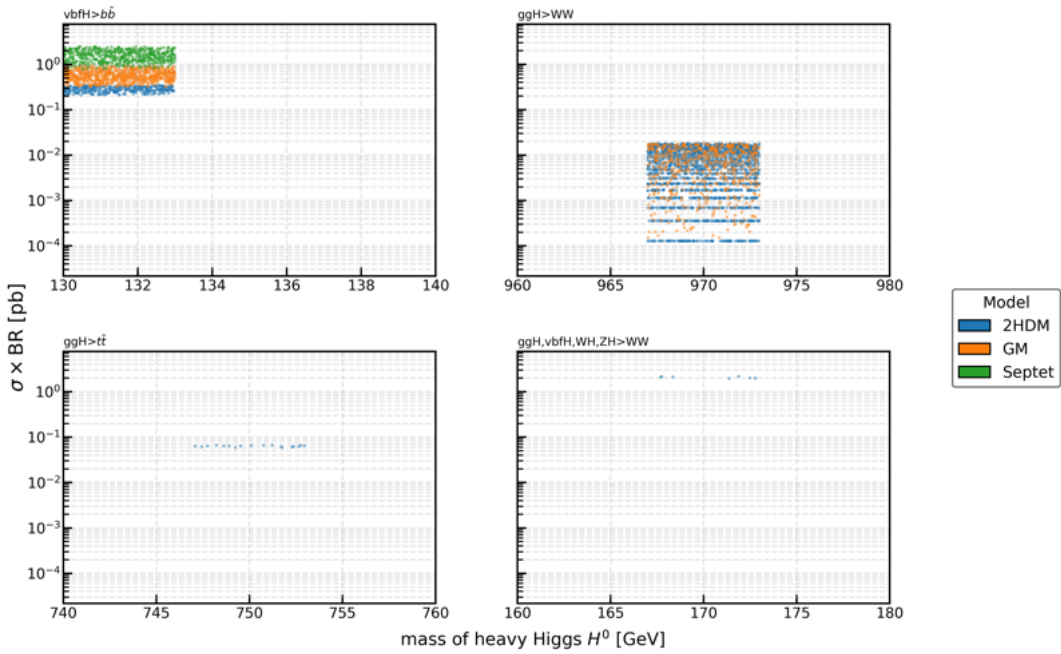


Figure 5.3.: Channel-wise panels with allowed points coloured by model. This figure groups channels with sparse mass coverage or smaller samples (e.g. $vbfH \rightarrow b\bar{b}$, $ggH \rightarrow t\bar{t}$, $ggH, vbfH, WH, ZH \rightarrow WW$).

5.4.3. Plots for $\kappa_V^{H^0}$ versus m_{H^0} (allowed region)

The following plots, see Figure 5.4 summarizes, for each model (2HDM, GM, Septet), the range of the heavy–Higgs gauge coupling $\kappa_V^{H^0}$ that is still allowed by HiggsBounds, according to the most sensitive analysis, as discussed in previous section. For every mass value, we scan all allowed points and take the largest and the smallest $\kappa_V^{H^0}$. The solid line shows the per mass **maximum**; the dashed line shows the per mass **minimum**. It is important to notice, that these correspond to the global κ_{min} and κ_{max} , so it is possible that the values come from different channels. For channel specific kappa ranges please refer to Table 5.2 and the channel specific κ and mass grid, $(m_{H^0}, \kappa_V^{H^0})$, please refer to the channel-coded heatmaps in Appendix G.2.1.

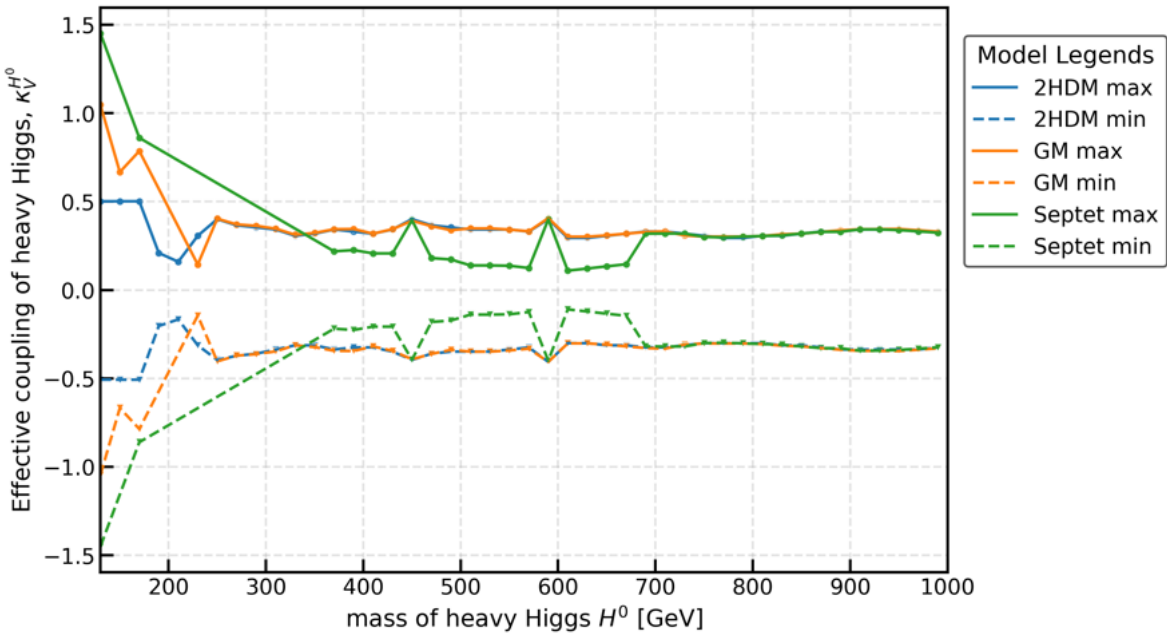


Figure 5.4.: Allowed ranges of $\kappa_V^{H^0}$ as a function of m_{H^0} for the three models. Solid (dashed) curves are the per-mass maxima (minima) over all allowed points. The edges at a given mass can be set by different channels; see the channel coded heatmaps for channel specific $\kappa_V^{H^0}$ vs m_{H^0} in Appendix G.2.1.

The scatter plots, see Figure 5.1, and the maximum coupling plots, see Figure 5.4, provide us with a comparative view of the kappa ranges of the three models. We notice that we obtain more concentrated model-specific bounds on $\kappa_V^{H^0}$ than the initial scan ranges after the exclusion analysis. Table 5.1 summarizes the prior scan intervals and the updated ranges inferred from the allowed data set.

Table 5.1.: Model-wise ranges for the effective coupling $\kappa_V^{H^0}$. The “scan range” is the input interval used to generate points. The “updated range” is inferred from the allowed points in the figures above.

Model	Scan range for $\kappa_V^{H^0}$	Updated range from allowed points
2HDM	$[-0.51, 0.50]$	$\approx [-0.5, 0.5]$
GM	$[-1.39, 1.39]$	$\approx [-1.0, 1.0]$
Septet	$[-3.91, 3.91]$	$\approx [-1.49, 1.49]$

5.4.4. Mass panels for $\kappa_V^{H^0}$ coupling heatmaps with allowed and excluded points

To resolve how the exclusions depend on the mixing parameters, we show, in Figures 5.5, 5.6 and 5.7, the heatmaps at fixed heavy-Higgs masses in the relevant mixing planes of each model. The background color is the effective vector coupling $\kappa_V^{H^0}$ implied by the angles. On top of this, we

overlay the scan points and mark the outcome of the HiggsBounds test (allowed or excluded), with the point color indicating the most-sensitive search channel for the excluded points. These panels let us read, mass by mass, the allowed range of $\kappa_V^{H^0}$ and which analyses are responsible for the exclusions. We also notice the complementary behaviour of the allowed and excluded points for a particular mass value. Where applicable, the band corresponding to the 2σ constraint on the SM-like Higgs coupling is also drawn for reference, which provided us with our initial scan input values for the mixing angles.

Two-Higgs-Doublet Model (2HDM)

Figure 5.5 shows, at representative masses, the (β, α) plane overlayed by a narrow diagonal band of viable $\kappa_V^{H^0}$ values for 2HDM. Allowed and excluded points cluster along this band, and the channel colors indicate which searches dominate according to the coupling values. We notice important exclusion channels $ggH>ZZ$ for lower masses, as seen in $m = 290$ GeV and $H>WW, ZZ$ and $vbf>WW, ZZ$ for the larger masses.

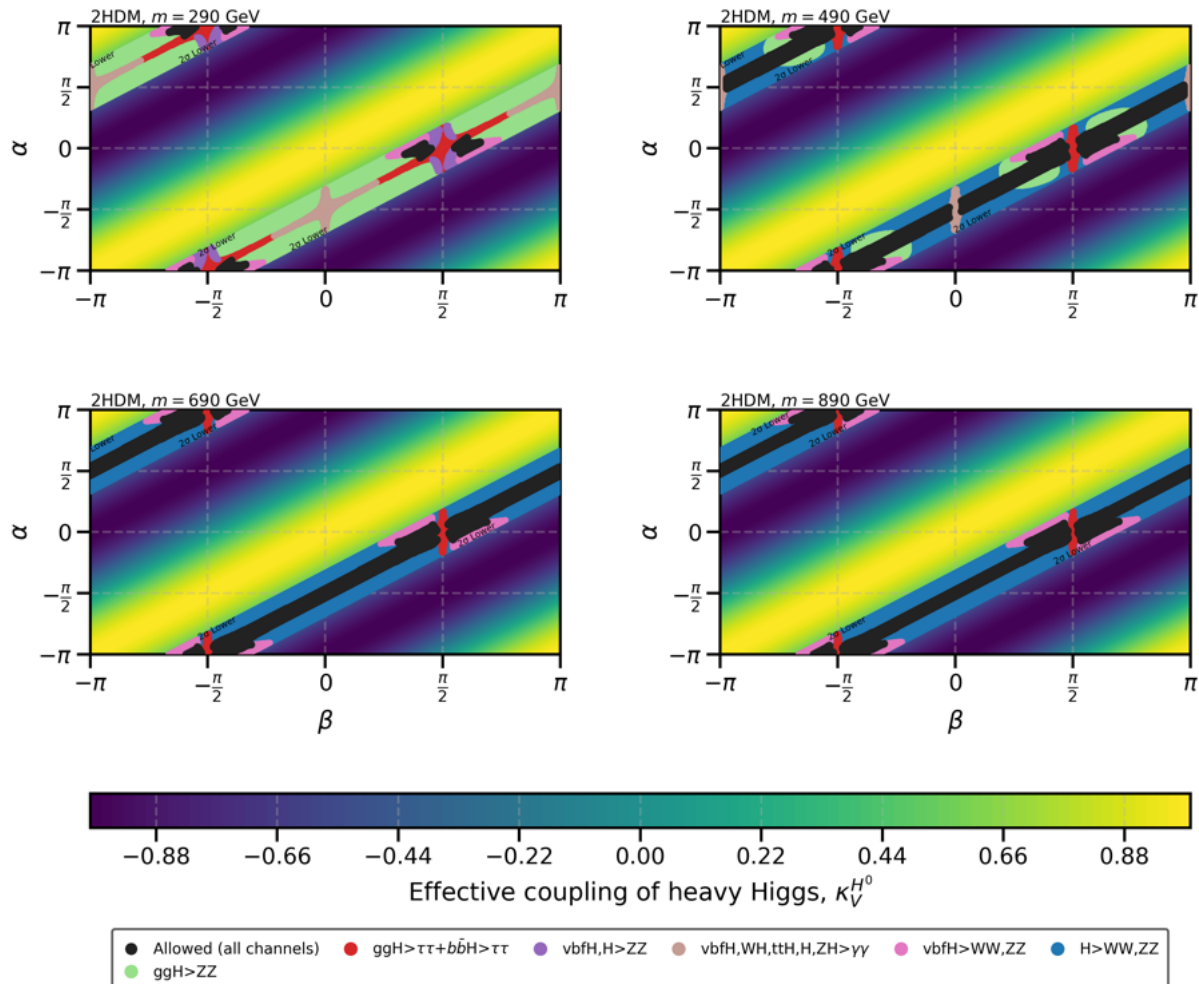


Figure 5.5.: 2HDM mass panel overlays in the (β, α) plane, with a $\kappa_V^{H^0}$ heatmap as the background and the color-coded regions are most-sensitive channel from the HiggsBounds result.

Georgi-Machacek (GM)

For the GM model, Figure 5.6 shows the (θ_H, α) plane. The 2σ band from Higgs-coupling measurements appears as a broad curve across the plane; within and near this band the allowed points concentrate. The channel labels indicate the region of dominant search channels for a given mass value. In the following panels, similar to 2HDM, we notice important exclusion channels including, $ggH>ZZ$ for lower masses, as seen in $m = 290$ GeV and $H>WW, ZZ$ for the larger masses.

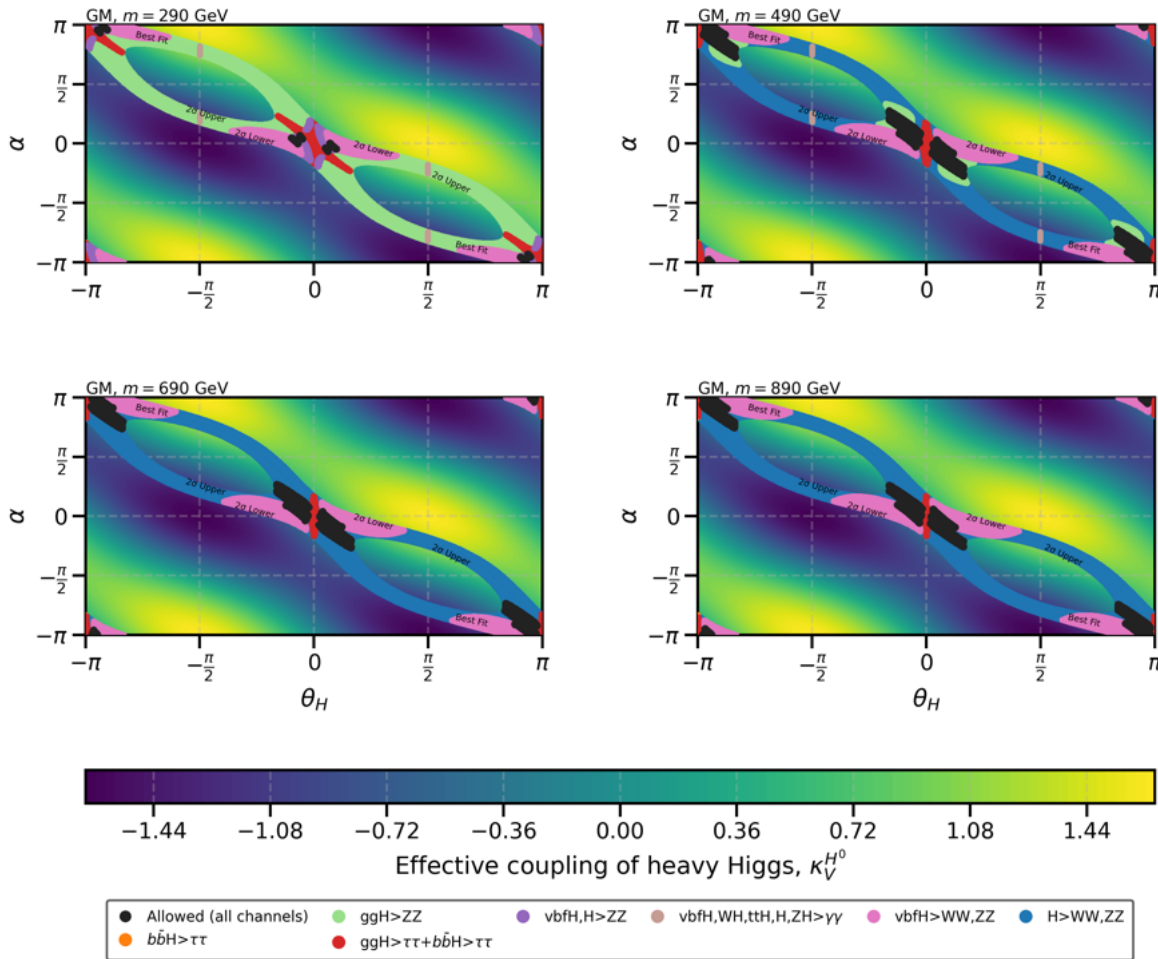


Figure 5.6.: GM mass panel overlays in the (θ_H, α) plane, with a $\kappa_V^{H^0}$ heatmap as the background and the color-coded regions are most-sensitive channel from the HiggsBounds result.

Septet

In the Septet model, Figure 5.7, shows the (θ_7, α) maps where we see a wider range of $\kappa_V^{H^0}$. But once the searches are applied the allowed points occupy a smaller subset. As in the previous panel, colors identify the excluded channel as colored regions. In contrast to the 2HDM and GM, we see $vbf>WW, ZZ$ as the most important exclusion channel over all mass ranges with $ggH>ZZ$ and $H>WW, ZZ$ channels also contributing to lower and higher masses respectively.

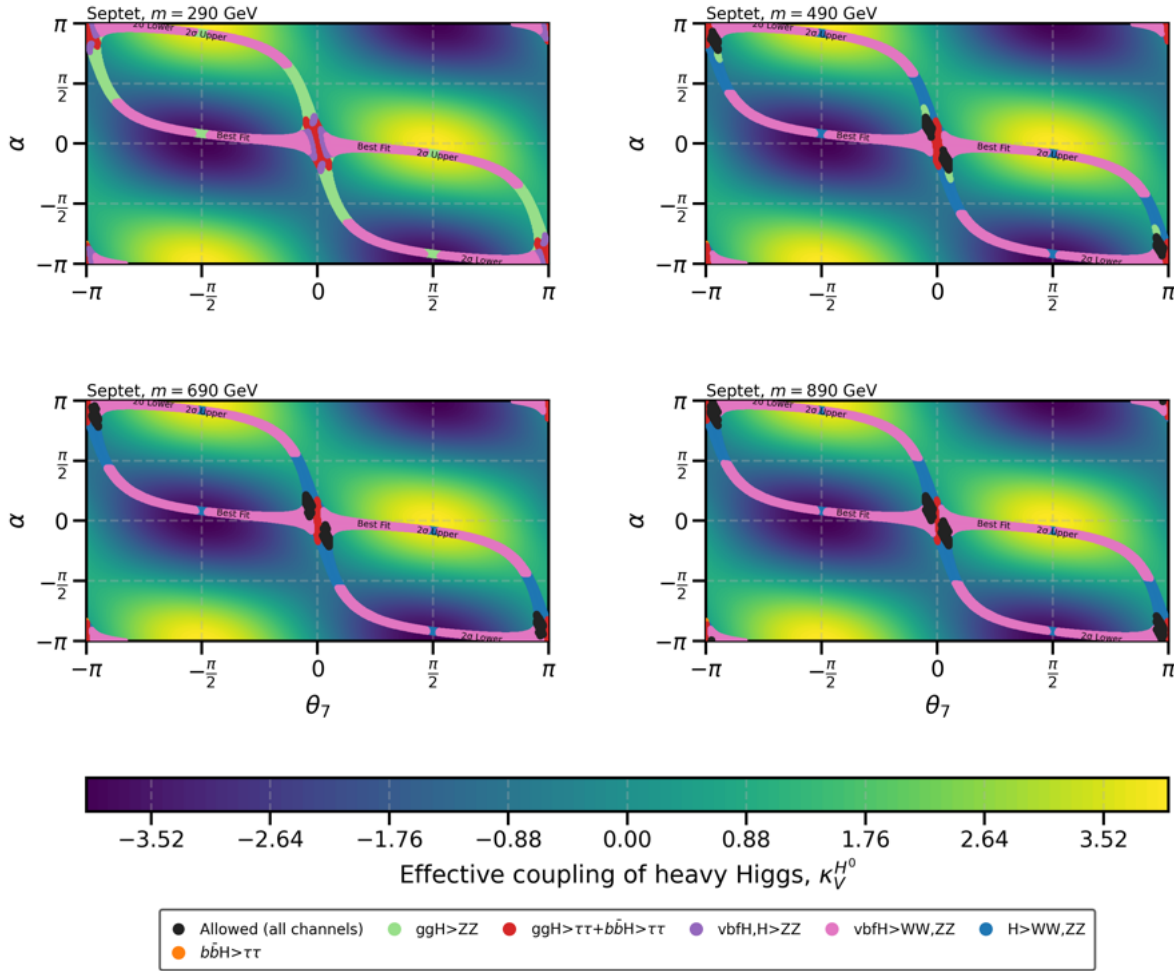


Figure 5.7.: Septet mass panel overlays in the (θ_7, α) plane, with a $\kappa_V^{H^0}$ heatmap as the background and the color-coded regions are most-sensitive channel from the HiggsBounds result.

Taken together, these overlays complement the plots and panels between the $\sigma \times \text{BR}$, the effective couplings, and mass, as they show the mass-by-mass window of $\kappa_V^{H^0}$ that remains viable and make clear which searches are actually responsible for the excluded and allowed regions in the mixing-angle plane.

5.5. Interpretation of Results

In the following section, we discuss the allowed points given by HiggsBounds (see sec. 5.3). Relative to the input scans, the viable ranges of the effective coupling are narrowed, after the analysis to

$$\kappa_V^{H^0} \in [-0.50, 0.50] \text{ (2HDM)}, \quad \kappa_V^{H^0} \in [-1.05, 1.05] \text{ (GM)}, \quad \kappa_V^{H^0} \in [-1.45, 1.45] \text{ (Septet)},$$

in also shown in Fig. 5.4 and Table 5.1. From the most sensitive channel analysis, based on the linear scan of mixing angles, α and $\beta/\theta_H/\theta_7$, diboson searches ($vbfH, H \rightarrow WW, ZZ$ from inclusive or other production modes) contributes about 79.5% of the allowed points, $\tau\tau$ searches account for 16.3%, diphoton analyses for 3.4%, and $b\bar{b}$ for 0.8%. These are shown with the channel maps and the $\sigma \times BR$ vs mass and scatter panels in sec. 5.4.

The numerical ranges quoted below correspond to the allowed sample for each channel. We consider the most relevant channel and their corresponding $\sigma \times BR$ rates observed among the allowed points.⁴ In Table 5.2, we refer to the canonical labels returned by HiggsBounds as follows:

- **Vector-Boson Fusion (vbf) decaying to dibosons** ($vbfH \rightarrow WW, ZZ$)
- **gluon fusion to ZZ** ($ggH \rightarrow ZZ$)
- **tautau decay** ($ggH \rightarrow \tau\tau + bbH \rightarrow \tau\tau$)
- **vbf to ZZ** ($vbfH \rightarrow ZZ$)
- **inclusive channels** ($vbfH, H \rightarrow ZZ$), this channel is attributed to an "inclusive" analysis, where we sum the cross sections of all the production modes in accordance with the HiggsTools code.
- **Diphoton** ($vbfH, HW, Htt, H, HZ \rightarrow \gamma\gamma\gamma\gamma$)
- **vbf to bb** ($vbfH \rightarrow bb$)
- **Inclusive diboson** ($H \rightarrow WW, ZZ$)

⁴For reference, some excluded points in the low-mass region reach $\sigma \times BR \sim 10^3$ pb for $ggH/bbH \rightarrow \tau\tau$; these are removed by the observed limits and do not appear in the allowed sample. In contrast, the largest value in the allowed set is ~ 6.4 pb for the same channel as shown in Table 5.2.

Table 5.2.: Channel-wise ($\sigma \times \text{BR}$) ranges for the HB-selected analysis for the allowed points (sec. 5.3). A uniform floor of 10^{-6} pb is applied to the lower bound of ($\sigma \times \text{BR}$) to match the plotting convention. The last column lists representative references used in the `HiggsTools` dataset for each channel.

Channel	$(\sigma \times \text{BR})$ range [pb]	Reference Papers
VBF $\rightarrow WW, ZZ$	$[1.4 \times 10^{-3} - 2.7 \times 10^{-2}]$	[36, 37, 38]
ggF $\rightarrow ZZ$	$[5.8 \times 10^{-4} - 0.1 \times 10^{-1}]$	[36]
$\tau\tau$ (ggF+bbH)	$[1 \times 10^{-6} - 6.40]$	[39, 40, 41]
VBF $\rightarrow ZZ$	$[3 \times 10^{-3} - 7 \times 10^{-2}]$	[42, 36]
vbfH, H $\rightarrow ZZ$	$[2 \times 10^{-2} - 0.2]$	[42, 36]
Diphoton	$[2.5 \times 10^{-5} - 6.7 \times 10^{-4}]$	[43]
VBF $\rightarrow b\bar{b}$	$[0.2 - 2.49]$	[44]
$H \rightarrow WW, ZZ$	$[1 \times 10^{-6} - 7 \times 10^{-2}]$	[36, 45]

Some other specifications, that we notice, through the analysis are that some excluded points⁵ attain very large predicted rates, up to $\mathcal{O}(10^3)$ pb, but these points are excluded as lie well outside the allowed regions identified here; within the allowed sample the largest $(\sigma \times \text{BR})_{\text{most sensitive}}$ is 6.4 pb for the channel $ggH \rightarrow ZZ$ at 130 GeV as shown in the second panel of the Figure 5.2.

To summarize the results, across all three benchmark models, the allowed regions primarily from diboson searches, with $\tau\tau$ providing the next most important handle. The allowed $\kappa_V^{H^0}$ intervals further contract to $\sim [-0.5, 0.5]$ (2HDM), $\sim [-1.0, 1.0]$ (GM), and $\sim [-1.45, 1.45]$ (Septet), and the allowed $\sigma \times \text{BR}$ rates are typically around $10^{-3} - 10^{-2}$ pb in VBF decaying to dibosons, $10^{-3} - 10^{-2}$ pb in $ggH \rightarrow ZZ$, and up to a few pb in $\tau\tau$, see Figure 5.2, consistent with the Run 2 observed and expected limits encoded in `HiggsTools`.

⁵Please refer to appendix G to see model-wise shaded regions for $\sigma \times \text{BR}$ for all points including $\sigma \times \text{BR}$ the excluded points

6. Summary and Future Prospects

6.1. Summary of Theoretical Analysis

This thesis has developed a coherent theoretical framework for testing extended Higgs sectors in which the electroweak ρ parameter is preserved at tree level and perturbative unitarity is maintained in high-energy longitudinal vector–boson scattering. We focused on three models: the Two–Higgs–Doublet Model (2HDM), the Georgi–Machacek (GM) model, and the Scalar Septet model, chosen because their field content and vacuum alignment allow custodial symmetry to be preserved¹. For each model, we derived the physical spectrum, and derived the tree–level Higgs–vector–boson couplings, see Chapter 2. These couplings were then used to derive model–specific unitarity sum rules, see Chapter 3, that guarantee the cancellation of the $\mathcal{O}(E^2)$ growth in tree-level $V_L V_L \rightarrow V_L V_L$ amplitudes. In the 2HDM, the sum rule derived is $(\kappa_V^{h^0})^2 + (\kappa_V^{H^0})^2 = 1$. In the GM and Septet models, the charged custodial multiplets enter the sum rules with opposite sign relative to neutral exchange, yielding

$$(\kappa_V^{h^0})^2 + (\kappa_V^{H^0})^2 + (\kappa_{VV}^{H_5^0})^2 - (\kappa_{WW}^{H_5^{\pm\pm}})^2 = 1 \quad (\text{GM}),$$

$$(\kappa_V^h)^2 + (\kappa_V^H)^2 - (\kappa_{WW}^{H^{\pm\pm}})^2 = 1 \quad (\text{Septet}).$$

These identities encode the custodial cancellations and explicitly tells us how the charged states ($H_5^{\pm\pm}$ in GM and $H^{\pm\pm}$ in the Septet) participate in restoring unitarity.

After deriving the sum rules, we utilised these to obtain theoretical mass bounds for the extended Higgs models under consideration, see 3.4.

6.2. Experimental Constraints and the 2σ Higgs–Coupling Band

To compare our theoretical predictions with experimental data, we adopted the κ –framework for the observed 125 GeV Higgs boson and imposed the Run–2 global constraint on the vector–boson coupling modifier [20],

$$\kappa_V^{h^0} = 1.02 \pm 0.08 \quad \Rightarrow \quad 0.86 \leq \kappa_V^{h^0} \leq 1.18 \quad (2\sigma).$$

This bound restricts the mixing angles that enter the model–specific couplings, thereby constraining the viable (α, β) (2HDM), (α, θ_H) (GM), and (α, θ_7) (Septet) combinations. We made this connection explicit via heat maps of $\kappa_V^{h^0}$, see sub-section 4.3.1, across the relevant mixing planes and by using the allowed bands into corresponding ranges for the heavy Higgs–boson couplings $\kappa_V^{H^0}$ (and,

¹ ρ parameter = 1, see section 1.20

where applicable, $\kappa_{WW}^{H^{\pm\pm}}$). In each case, the indirect 2σ band narrows the priors used for the collider analysis.

6.3. HiggsTools Analysis and Results

In our analysis, we use our theoretically derived parameters as inputs into HiggsTools [34], and compare the model predictions for masses, widths, production rates, and branching ratios, provided via effective couplings. Within HiggsTools we exploit two packages HiggsBounds and HiggsSignals to obtain our relevant results. For each parameter point $(\kappa_V^{H^0}, m_{H^0})$, HiggsBounds selects the most sensitive channel which it obtains by evaluating the largest expRatio, where the exp and obsRatios are defined as [34]:

$$\text{obsRatio} = \frac{(\sigma \times \text{BR})_{\text{theory}}}{(\sigma \times \text{BR})_{\text{obs}}^{95\%}}, \quad \text{expRatio} = \frac{(\sigma \times \text{BR})_{\text{theory}}}{(\sigma \times \text{BR})_{\text{exp}}^{95\%}},$$

declaring the point excluded when $\text{obsRatio} > 1$. We scanned $m_{H^0} \in [130, 1000] \text{ GeV}$ and applied uniform physics filters (narrow-width approximation, numerical guards on effective couplings, and a pragmatic floor for extremely small $\sigma \times \text{BR}$ rates) to maintain physical and numerical stability across models.

Interpreting the final results, see section 5.4.4, we note that in the 2HDM, exclusions regions in the low-mass window ($\sim 250\text{--}300 \text{ GeV}$) dominated by gluon-fusion diboson searches ($\text{ggH} \rightarrow \text{ZZ}$), while exclusion region for larger masses is dominated by $\text{H} \rightarrow \text{WW/ZZ}$. A similar trend is followed in the GM model with an addition of the vector-boson-fusion (VBF) channels, $\text{vbfH} \rightarrow \text{WW/ZZ}$, also providing the exclusion regions. In contrast, in the Septet model, we note that $\text{vbfH} \rightarrow \text{WW/ZZ}$ is the dominant channel which provides us with the exclusion ranges.

As a compact numerical summary, the effective heavy-state couplings inferred from the allowed points contract to

$$\kappa_V^{H^0} \in [-0.50, 0.50] \text{ (2HDM)}, \quad \kappa_V^{H^0} \in [-1.00, 1.00] \text{ (GM)}, \quad \kappa_V^{H^0} \in [-1.50, 1.50] \text{ (Septet)},$$

consistent with the model sum rules and the 2σ band imposed on $\kappa_V^{h^0}$, see Figures 5.1 and 5.4. Apart from the concentrated kappa ranges we also obtain exclusion and allowed regions of the same using different channels provided by LEP and LHC searches², see section 5.4.4.

6.4. Future Prospects

The analysis strategy developed here can be extended in the following ways:

²HiggsTools analyses around 258 experiments from CMS, ATLAS and LEP searches, see [34]

(i) Heavier mass reach (up to 3 TeV). In our current analysis with `HiggsTools`, we obtain results upto 1 TeV, but some search channels have cross section limits upto 3 TeV. Hence, the same pipeline can be used to obtain limits at higher masses, without any major changes to the pipeline itself.

(ii) Incorporation of Run–3 datasets in `HiggsTools`. The integration of the LHC Run–3 analyses into `HiggsTools` will provide us with better estimates for our results. We can also expect to be able to utilize data from HL-LHC, to further improve our analysis in the future.

(iii) Systematic study of doubly charged Higgs bosons. `HiggsTools` natively supports searches for $H^{\pm\pm}$ through curated JSON entries and references. Using the same interface adopted here, one can provide the required production rates and branching ratios for $H^{\pm\pm}$ (following the references listed in the `HiggsTools` paper)[34] and repeat the full exclusion analysis. This is particularly compelling for the GM and Septet models, where $H^{\pm\pm}$ plays a direct role in the unitarity sum rules and yields striking collider signatures (e.g. same-sign WW).

In summary, the present work establishes a robust, model–specific comparative analysis between theory and experiment for the BSM models in our consideration. The combination of unitarity sum rules, model-wise Higgs couplings, and `HiggsTools` exclusions limits, provide us with an overview of the constraints. Another advantage of `HiggsTools` is that the pipeline can scale easily to higher masses, new datasets, and exotic signatures in the future.

A. Perturbative Unitarity in Quantum Field Theory

A.1. Unitarity and Partial Wave Expansion

The unitarity of the S -matrix, $S^\dagger S = 1$, guarantees probability conservation in quantum mechanics. For elastic $2 \rightarrow 2$ scattering, the incoming plane wave along the z -axis can be expressed as [13]:

$$\psi(\vec{r}) = e^{i\vec{k} \cdot \vec{r}} = e^{ikr \cos \theta}, \quad (\text{A.1})$$

which expands into spherical waves using Bessel functions j_ℓ and Legendre polynomials P_ℓ :

$$\psi(\vec{r}) = \sum_{\ell=0}^{\infty} (2\ell+1) i^\ell j_\ell(kr) P_\ell(\cos \theta). \quad (\text{A.2})$$

At large distances ($kr \gg \ell$), this becomes:

$$\psi(\vec{r}) \simeq \frac{i}{2k} \sum_{\ell=0}^{\infty} (2\ell+1) i^\ell \left[\frac{e^{-i(kr-\ell\pi/2)}}{r} - \frac{e^{+i(kr-\ell\pi/2)}}{r} \right] P_\ell(\cos \theta). \quad (\text{A.3})$$

In the presence of scattering, the outgoing wave picks up a phase $S_\ell(k)$:

$$\psi(\vec{r}) \simeq \frac{i}{2k} \sum_{\ell=0}^{\infty} (2\ell+1) i^\ell \left[\frac{e^{-i(kr-\ell\pi/2)}}{r} - S_\ell(k) \frac{e^{+i(kr-\ell\pi/2)}}{r} \right] P_\ell(\cos \theta). \quad (\text{A.4})$$

A.1.1. Unitarity Constraint

Conservation of flux requires $|S_\ell(k)| \leq 1$, leading to the definition of the partial wave amplitude [13]:

$$a_\ell(k) = \frac{S_\ell(k) - 1}{2i}, \quad (\text{A.5})$$

and the full wavefunction becomes:

$$\psi(\vec{r}) \simeq e^{ikr \cos \theta} + \frac{1}{r} \sum_{\ell=0}^{\infty} (2\ell+1) a_\ell(k) P_\ell(\cos \theta) e^{ikr}. \quad (\text{A.6})$$

Each a_ℓ must lie within a unit circle in the complex plane:

$$|a_\ell| \leq 1, \quad \text{Re}(a_\ell) \leq \frac{1}{2}, \quad 0 \leq \text{Im}(a_\ell) \leq 1. \quad (\text{A.7})$$

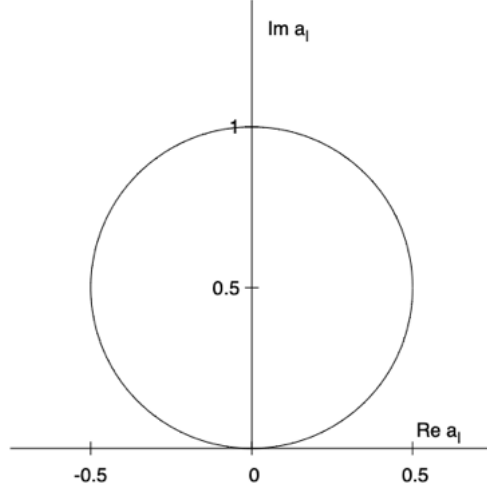


Figure A.1.: Allowed region for partial wave amplitudes a_ℓ in the complex plane.

A.2. From Quantum Mechanics to Field Theory

In quantum mechanics, the scattering amplitude is the second term of equation A.6:

$$f(\theta) = \frac{1}{k} \sum_{\ell=0}^{\infty} (2\ell+1) a_\ell(k) P_\ell(\cos \theta), \quad (\text{A.8})$$

with differential cross section:

$$\frac{d\sigma}{d\Omega} = |f(\theta)|^2. \quad (\text{A.9})$$

In QFT, the two-to-two cross section is:

$$\left(\frac{d\sigma}{d\Omega} \right)_{\text{CM}} = \frac{|\mathcal{M}|^2}{64\pi^2 E_{\text{CM}}^2}, \quad (\text{A.10})$$

and the matrix element expands in partial waves as:

$$\mathcal{M}(s, \theta) = 16\pi \sum_{\ell=0}^{\infty} (2\ell+1) a_\ell P_\ell(\cos \theta). \quad (\text{A.11})$$

A.2.1. Tree-Level Unitarity Bound

Since tree-level amplitudes are real, the unitarity condition becomes [13]:

$$|\text{Re}(a_\ell)| \leq \frac{1}{2}. \quad (\text{A.12})$$

This constraint ensures that scattering amplitudes remain bounded and physical at high energies, and places critical limits on model parameters like Higgs masses and couplings in BSM theories.

B. Mass Matrices in the 2HDM

To extract the physical scalar masses, we expand the Higgs potential up to second order in the component fields $\rho_{1,2}$ (CP-even), $\eta_{1,2}$ (CP-odd), and $\omega_{1,2}^\pm$ (charged). The bilinear part of the potential contains the terms:

$$V_{\text{bilinear}} = \frac{1}{2} \begin{pmatrix} \rho_1 & \rho_2 \end{pmatrix} M_\rho^2 \begin{pmatrix} \rho_1 \\ \rho_2 \end{pmatrix} + \frac{1}{2} \begin{pmatrix} \eta_1 & \eta_2 \end{pmatrix} M_\eta^2 \begin{pmatrix} \eta_1 \\ \eta_2 \end{pmatrix} + \frac{1}{2} \begin{pmatrix} \omega_1^+ & \omega_2^+ \end{pmatrix} M_\omega^2 \begin{pmatrix} \omega_1^- \\ \omega_2^- \end{pmatrix}. \quad (\text{B.1})$$

Below we list the explicit forms of the mass matrices. These are derived by collecting the second-order (quadratic) coefficients of each pair of fields after substituting the parametrized Higgs doublets into the potential.

CP-even Higgs (Scalar) Mass Matrix M_ρ^2

$$M_{\rho 11}^2 = \frac{\lambda_1 v_1^3 + m_{12}^2 v_2}{v_1}, \quad (\text{B.2})$$

$$M_{\rho 22}^2 = \frac{\lambda_2 v_2^3 + m_{12}^2 v_1}{v_2}, \quad (\text{B.3})$$

$$M_{\rho 12}^2 = (\lambda_3 + \lambda_4 + \lambda_5) v_1 v_2 - m_{12}^2. \quad (\text{B.4})$$

CP-odd Higgs (Pseudoscalar) Mass Matrix M_η^2

$$M_{\eta 11}^2 = (-\lambda_5 v_1 v_2 + m_{12}^2) \frac{v_2}{v_1}, \quad (\text{B.5})$$

$$M_{\eta 22}^2 = (-\lambda_5 v_1 v_2 + m_{12}^2) \frac{v_1}{v_2}, \quad (\text{B.6})$$

$$M_{\eta 12}^2 = \lambda_5 v_1 v_2 - m_{12}^2. \quad (\text{B.7})$$

Charged Higgs Mass Matrix M_ω^2

$$M_{\omega 11}^2 = (2m_{12}^2 - (\lambda_4 + \lambda_5)v_1 v_2) \frac{v_2}{2v_1}, \quad (\text{B.8})$$

$$M_{\omega 22}^2 = (2m_{12}^2 - (\lambda_4 + \lambda_5)v_1 v_2) \frac{v_1}{2v_2}, \quad (\text{B.9})$$

$$M_{\omega 12}^2 = \frac{1}{2}(\lambda_4 + \lambda_5)v_1 v_2 - m_{12}^2. \quad (\text{B.10})$$

Tree-level Masses from Diagonalization

Diagonalizing each mass matrix yields the physical Higgs masses in the mass eigenbasis. Assuming the tadpole conditions are imposed at tree level, the resulting masses are:

CP-even neutral Higgs bosons:

$$m_{h^0}^2 = \frac{1}{2} \left[M_{\rho 11}^2 + M_{\rho 22}^2 - \sqrt{(M_{\rho 11}^2 - M_{\rho 22}^2)^2 + 4(M_{\rho 12}^2)^2} \right], \quad (\text{B.11})$$

$$m_{H^0}^2 = \frac{1}{2} \left[M_{\rho 11}^2 + M_{\rho 22}^2 + \sqrt{(M_{\rho 11}^2 - M_{\rho 22}^2)^2 + 4(M_{\rho 12}^2)^2} \right]. \quad (\text{B.12})$$

CP-odd neutral Higgs boson:

$$m_{A^0}^2 = \left(\frac{m_{12}^2}{v_1 v_2} - \lambda_5 \right) v^2, \quad (\text{B.13})$$

$$m_{G^0}^2 = 0. \quad (\text{B.14})$$

Charged Higgs bosons:

$$m_{H^\pm}^2 = \left(\frac{m_{12}^2}{v_1 v_2} - \frac{\lambda_4 + \lambda_5}{2} \right) v^2, \quad (\text{B.15})$$

$$m_{G^\pm}^2 = 0. \quad (\text{B.16})$$

The eigenstates G^0 and G^\pm are the Goldstone bosons, which are “eaten” by the Z and W^\pm bosons, respectively, to give them longitudinal polarization and mass.

C. Custodial Symmetry Transformations in the GM Model

To ensure custodial symmetry is preserved in the Georgi-Machacek (GM) model, we impose a global $SU(2)_L \times SU(2)_R$ symmetry on the scalar potential. Under this symmetry, the doublet and triplet scalar fields transform as:

$$\Phi \rightarrow L\Phi R^\dagger, \quad (\text{C.1})$$

$$\Delta \rightarrow L\Delta R^\dagger, \quad (\text{C.2})$$

where $L = e^{i\sigma^a\theta^a/2}$ and $R = e^{iT^a\theta^a}$ are group elements of $SU(2)_L$ and $SU(2)_R$, and σ^a and T^a are the generators in the doublet and triplet representations, respectively.

Triplet Basis and Similarity Transformation

The T^a generators of $SU(2)$ in the adjoint (triplet) basis are given by:

$$T^1 = \frac{1}{\sqrt{2}} \begin{pmatrix} 0 & 1 & 0 \\ 1 & 0 & 1 \\ 0 & 1 & 0 \end{pmatrix}, \quad T^2 = \frac{1}{\sqrt{2}} \begin{pmatrix} 0 & -i & 0 \\ i & 0 & -i \\ 0 & i & 0 \end{pmatrix}, \quad T^3 = \begin{pmatrix} 1 & 0 & 0 \\ 0 & 0 & 0 \\ 0 & 0 & -1 \end{pmatrix}. \quad (\text{C.3})$$

To relate these triplet generators to their adjoint action (as required when constructing invariants like λ_5 , μ_1 , and μ_2 terms), we use a similarity transformation defined via the operator P :

$$P = \frac{1}{\sqrt{2}} \begin{pmatrix} -1 & i & 0 \\ 0 & 0 & \sqrt{2} \\ 1 & i & 0 \end{pmatrix}. \quad (\text{C.4})$$

Adjoint Representation and $SO(3)$ Rotation

The adjoint transformation of the generators under $SU(2)$ is given by:

$$e^{(i\theta^b\sigma^b)/2} \frac{\sigma^a}{2} e^{(-i\theta^c\sigma^c)/2} = R(\vec{\theta})_{aa'} \frac{\sigma^{a'}}{2}, \quad (\text{C.5})$$

$$e^{(i\theta^b T^b)} T^a e^{(-i\theta^c T^c)} = R(\vec{\theta})_{aa'} T^{a'}, \quad (\text{C.6})$$

where $R(\vec{\theta}) = e^{i\theta^a T^a}$ is the adjoint representation of $SU(2)$, isomorphic to $SO(3)$. This acts as a rotation matrix satisfying $R_{ac}^T R_{cb} = \delta_{ab}$.

For example, the λ_5 term in the scalar potential can be written as:

$$\text{Tr} \left(\Phi^\dagger \frac{\sigma^a}{2} \Phi \frac{\sigma^b}{2} \right) \text{Tr} \left(\Delta^\dagger T^a \Delta T^b \right) = R_{aa'} R_{bb'} \text{Tr} \left(\Phi^\dagger \frac{\sigma^{a'}}{2} \Phi \frac{\sigma^{b'}}{2} \right) \text{Tr} \left(\Delta^\dagger T^{a'} \Delta T^{b'} \right), \quad (\text{C.7})$$

ensuring full custodial invariance under the adjoint transformation.

Transformation in the P Basis

To implement the transformation in a fixed basis (e.g. the T^3 eigenbasis), we rotate the adjoint generators via:

$$(P^\dagger e^{-i\theta^b T^b} P)_{aa'} = e_{aa'}^{(i\theta_{\text{adj}}^b)} = R(\vec{\theta})_{aa'}, \quad (\text{C.8})$$

showing that the same adjoint rotation is applied, but now expressed in the P -diagonalized basis.

In summary, the λ_5 , μ_1 , and μ_2 terms are constructed to be invariant under this adjoint action, ensuring full $SU(2)_L \times SU(2)_R \rightarrow SU(2)_C$ symmetry. This formalism is crucial in deriving a scalar potential that maintains custodial symmetry. A more detailed breakdown of the transformation properties and basis conversions can be found in references.

D. Coupling Structures in the GM Model

This appendix provides the effective coupling factors for Higgs interactions with gauge bosons in the Georgi-Machacek (GM) model. These couplings are derived from the electroweak Lagrangian involving the scalar fields and are essential for computing amplitudes in vector boson scattering processes.

The effective couplings $\kappa_{VV}^{h_i}$ (where h_i denotes a Higgs state and $V = W, Z$) describe the normalized strength of interaction between scalars and gauge bosons in the GM model. These are obtained from gauge-kinetic terms after symmetry breaking and field mixing.

D.1. Higgs Vector Boson Vector Boson Effective Couplings

Table D.1.: **Effective couplings** $\kappa_{VV}^{h_i}$ of scalar bosons to pairs of electroweak vector bosons in the GM model.

Interaction	Effective Coupling	Interaction	Effective Coupling
$\kappa_{WW}^{h^0}$	$c_H \cos \alpha - \frac{\sqrt{8}}{\sqrt{3}} s_H \sin \alpha$	$\kappa_{WW}^{H^0}$	$c_H \sin \alpha + \frac{\sqrt{8}}{\sqrt{3}} s_H \cos \alpha$
$\kappa_{ZZ}^{h^0}$	$c_H \cos \alpha - \frac{\sqrt{8}}{\sqrt{3}} s_H \sin \alpha$	$\kappa_{ZZ}^{H^0}$	$c_H \sin \alpha + \frac{\sqrt{8}}{\sqrt{3}} s_H \cos \alpha$
$\kappa_{ZZ}^{H_5^0}$	$-\frac{2}{\sqrt{3}} s_H$	$\kappa_{W^\mp Z}^{H_5^\pm}$	s_H
$\kappa_{W^\mp W^\mp}^{H_5^{\pm\pm}}$	$\sqrt{2} s_H$		

D.2. Higgs Higgs Vector Boson Couplings

Table D.2.: **Effective couplings** κ for Higgs–Higgs–Vector boson vertices in the GM model.

Interaction	Effective Coupling	Interaction	Effective Coupling
$H_5^{++} H_5^- A_\mu$	$2e$	$H_5^+ H_5^- A_\mu$	$-e$
$H_5^+ H_5^- Z_\mu$	$-\frac{g}{2c_W} (1 - 2s_W^2)$	$H_5^{++} H_5^- Z_\mu$	$\pm \frac{g}{2c_W} (1 - 2s_W^2)$
$H_5^0 H_5^0 Z_\mu$	$-\frac{g}{\sqrt{3}c_W} (1 - 2s_W^2)$	$H_3^0 H_2^0 Z_\mu$	$-\frac{g}{6c_W} (2\sqrt{6}c_H \cos \alpha - 3s_H \sin \alpha)$
$H_5^\pm H_2^0 W_\mu^\mp$	$-\frac{g}{\sqrt{2}} c_H$	$H_5^\pm H_0^0 W_\mu^\mp$	$\pm \frac{g}{2} c_H$
$H_3^0 H_0^0 W_\mu^\pm$	$-\frac{g}{6} \sqrt{3} c_H$	$H_3^0 H_0^0 W_\mu^\mp$	$\pm \frac{g}{2}$
$H_5^\pm H_0^0 W_\mu^\mp$	$\frac{g}{2\sqrt{3}} (\sqrt{8}c_H \cos \alpha + s_H \cos \alpha)$	$H_3^\pm H_0^0 W_\mu^\mp$	$-\frac{g}{2} \left(\frac{\sqrt{8}}{\sqrt{3}} c_H \cos \alpha - s_H \sin \alpha \right)$

E. Other Vector Boson Scattering Channels

E.1. 2HDM: Higgs-mediated $W_L^+ W_L^- \rightarrow Z_L Z_L$ Scattering

For the 2HDM, the matrix element for $W_L^+ W_L^- \rightarrow Z_L Z_L$ scattering via Higgs exchange is:

$$i\mathcal{M} \frac{1}{\sqrt{2}} = -\frac{i}{v^2} \frac{1}{\sqrt{2}} \left[\left(\kappa_{WW}^{h^0} \kappa_{ZZ}^{h^0} \right) \left(\frac{s^2}{s - m_{h^0}^2} \right) + \left(\kappa_{WW}^{H^0} \kappa_{ZZ}^{H^0} \right) \left(\frac{s^2}{s - m_{H^0}^2} \right) + \mathcal{O}(1) \right] \quad (\text{E.1})$$

$$\simeq \frac{i}{v^2} \frac{1}{\sqrt{2}} \left[\left(\kappa_{WW}^{h^0} \kappa_{ZZ}^{h^0} + \kappa_{WW}^{H^0} \kappa_{ZZ}^{H^0} \right) s + \dots \right]. \quad (\text{E.2})$$

The unitarity sum rule ensuring $\mathcal{O}(E^2)$ cancellation is:

$$\left(\kappa_{WW}^{h^0} \kappa_{ZZ}^{h^0} \right) + \left(\kappa_{WW}^{H^0} \kappa_{ZZ}^{H^0} \right) = 1. \quad (\text{E.3})$$

E.2. 2HDM: Higgs mediated $Z_L Z_L \rightarrow Z_L Z_L$ Scattering

This channel receives only Higgs-mediated contributions. There are no pure gauge diagrams such as $ZZZZ$, ZZZ , or $ZZ\gamma$, due to gauge structure constraints. The matrix element at high energy is:

$$i\mathcal{M} \frac{1}{2} = -\frac{i}{v^2} \frac{1}{2} \left[\left(\kappa_{ZZ}^{h^0} \right)^2 \left(\frac{s^2}{s - m_{h^0}^2} + \frac{t^2}{t - m_{h^0}^2} + \frac{u^2}{u - m_{h^0}^2} \right) + \left(\kappa_{ZZ}^{H^0} \right)^2 \left(\frac{s^2}{s - m_{H^0}^2} + \dots \right) + \mathcal{O}(1) \right] \quad (\text{E.4})$$

$$\simeq -\frac{i}{v^2} \frac{1}{2} \left[\left(\left(\kappa_{ZZ}^{h^0} \right)^2 + \left(\kappa_{ZZ}^{H^0} \right)^2 \right) (s + t + u) + 3m_{h^0}^2 + 3m_{H^0}^2 + \dots \right]. \quad (\text{E.5})$$

The unitarity sum rule:

$$\left(\kappa_{ZZ}^{h^0} \right)^2 + \left(\kappa_{ZZ}^{H^0} \right)^2 = 1. \quad (\text{E.6})$$

Since $s + t + u = 4m_Z^2$, there is no dangerous $\mathcal{O}(E^2)$ term to cancel.

E.3. GM Model: $W_L^+ W_L^- \rightarrow Z_L Z_L$

In the Georgi–Machacek (GM) model, the custodial symmetry allows both the CP-even singlets h^0 , H^0 and the custodial fiveplet H_5^0 to contribute to $W_L^+ W_L^- \rightarrow Z_L Z_L$ scattering. The Higgs-exchange amplitude at high energy is:

$$i\mathcal{M} \frac{1}{\sqrt{2}} = -\frac{i}{v^2} \frac{1}{\sqrt{2}} \left[\left(\kappa_{WW}^{h^0} \kappa_{ZZ}^{h^0} \right) \frac{s^2}{s - m_{h^0}^2} + \left(\kappa_{WW}^{H^0} \kappa_{ZZ}^{H^0} \right) \frac{s^2}{s - m_{H^0}^2} + \left(\kappa_{WW}^{H_5^0} \kappa_{ZZ}^{H_5^0} \right) \frac{s^2}{s - m_{H_5^0}^2} + \mathcal{O}(1) \right] \quad (\text{E.7})$$

$$\simeq \frac{i}{v^2} \frac{1}{\sqrt{2}} \left[\kappa_{WW}^{h^0} \kappa_{ZZ}^{h^0} + \kappa_{WW}^{H^0} \kappa_{ZZ}^{H^0} + \kappa_{WW}^{H_5^0} \kappa_{ZZ}^{H_5^0} \right] s + \dots \quad (\text{E.8})$$

The unitarity sum rule becomes:

$$\kappa_{WW}^{h^0} \kappa_{ZZ}^{h^0} + \kappa_{WW}^{H^0} \kappa_{ZZ}^{H^0} + \kappa_{WW}^{H_5^0} \kappa_{ZZ}^{H_5^0} = 1. \quad (\text{E.9})$$

E.4. GM Model: $Z_L Z_L \rightarrow Z_L Z_L$

Only scalar exchanges contribute, with h^0 , H^0 , and H_5^0 propagators:

$$i\mathcal{M} \frac{1}{2} = -\frac{i}{v^2} \frac{1}{2} \sum_{S=h^0, H^0, H_5^0} \left(\kappa_{ZZ}^S \right)^2 \left(\frac{s^2}{s - m_S^2} + \frac{t^2}{t - m_S^2} + \frac{u^2}{u - m_S^2} \right) + \mathcal{O}(1) \quad (\text{E.10})$$

$$\simeq -\frac{i}{v^2} \frac{1}{2} \left[\sum_S \left(\kappa_{ZZ}^S \right)^2 (s + t + u) + \dots \right]. \quad (\text{E.11})$$

The unitarity sum rule reads:

$$\left(\kappa_{ZZ}^{h^0} \right)^2 + \left(\kappa_{ZZ}^{H^0} \right)^2 + \left(\kappa_{ZZ}^{H_5^0} \right)^2 = 1. \quad (\text{E.12})$$

As in the 2HDM, $s + t + u = 4m_Z^2$, so the $\mathcal{O}(E^2)$ terms vanish.

E.5. Septet Model: $Z_L Z_L \rightarrow Z_L Z_L$

In the scalar septet model, the $Z_L Z_L \rightarrow Z_L Z_L$ scattering amplitude receives contributions from the s -, t -, and u -channel exchange of the neutral scalars h and H . The resulting matrix element is:

$$\mathcal{M} = -\frac{1}{2v^2} \left[(\kappa_V^h)^2 \left(\frac{s^2}{s - m_h^2} + \frac{t^2}{t - m_h^2} + \frac{u^2}{u - m_h^2} \right) + (\kappa_V^H)^2 \left(\frac{s^2}{s - m_H^2} + \frac{t^2}{t - m_H^2} + \frac{u^2}{u - m_H^2} \right) \right] \quad (\text{E.13})$$

$$\simeq -\frac{3}{2v^2} \left[(\kappa_V^h)^2 m_h^2 + (\kappa_V^H)^2 m_H^2 \right], \quad (\text{E.14})$$

where the high-energy limit $s + t + u \simeq 0$ has been used.

Here, a factor of $1/\sqrt{2}$ for each pair of identical particles in the initial and final states is included. There is no associated sum rule in this case, as the potentially dangerous $\mathcal{O}(E^2)$ growth cancels automatically. However, perturbative unitarity imposes the following bound on the masses and couplings:

$$(\kappa_V^h)^2 m_h^2 + (\kappa_V^H)^2 m_H^2 \leq \frac{16\pi v^2}{3}. \quad (\text{E.15})$$

E.6. Septet Model: $W^\pm Z \rightarrow W^\pm Z$

This process receives contributions from t -channel exchange of h and H , as well as from s - and u -channel exchange of the singly-charged scalars H_1^\pm and H_2^\pm . The matrix element is:

$$\mathcal{M} = -\frac{1}{v^2} \left[(\kappa_V^h)^2 \frac{t^2}{t - m_h^2} + (\kappa_V^H)^2 \frac{t^2}{t - m_H^2} + (\kappa_{WZ}^{H_1^+})^2 \left(\frac{s^2}{s - m_{H_1^+}^2} + \frac{u^2}{u - m_{H_1^+}^2} \right) \right] \quad (\text{E.16})$$

$$+ (\kappa_{WZ}^{H_2^+})^2 \left(\frac{s^2}{s - m_{H_2^+}^2} + \frac{u^2}{u - m_{H_2^+}^2} \right) \quad (\text{E.17})$$

$$\simeq -\frac{1}{v^2} \left[\left((\kappa_V^h)^2 + (\kappa_V^H)^2 - (\kappa_{WZ}^{H_1^+})^2 - (\kappa_{WZ}^{H_2^+})^2 \right) t \right. \quad (\text{E.18})$$

$$\left. + (\kappa_V^h)^2 m_h^2 + (\kappa_V^H)^2 m_H^2 + 2(\kappa_{WZ}^{H_1^+})^2 m_{H_1^+}^2 + 2(\kappa_{WZ}^{H_2^+})^2 m_{H_2^+}^2 \right], \quad (\text{E.19})$$

where the relation $s + u \simeq -t$ has been applied.

Matching this to the high-energy behaviour of the SM amplitude yields the sum rule:

$$(\kappa_V^h)^2 + (\kappa_V^H)^2 - (\kappa_{WZ}^{H_1^+})^2 - (\kappa_{WZ}^{H_2^+})^2 = 1. \quad (\text{E.20})$$

Perturbative unitarity also leads to the bound:

$$(\kappa_V^h)^2 m_h^2 + (\kappa_V^H)^2 m_H^2 + 2(\kappa_{WZ}^{H_1^+})^2 m_{H_1^+}^2 + 2(\kappa_{WZ}^{H_2^+})^2 m_{H_2^+}^2 \leq 8\pi v^2. \quad (\text{E.21})$$

E.7. Constraints from Perturbative Unitarity on Model

Parameters

In each extended Higgs model, perturbative unitarity of longitudinal vector boson scattering ($WZ \rightarrow WZ, ZZ \rightarrow ZZ$) places bounds on the scalar couplings, masses, and mixing angles. We discuss below the relevant constraints for the 2HDM, GM model, and the Septet model.

E.7.1. 2HDM: Bounds on $\cos^2(\beta - \alpha)$ and m_{H^0}

From the $W_L^+ Z \rightarrow W_L^+ Z$ and $Z_L Z_L \rightarrow Z_L Z_L$ scattering amplitudes in the 2HDM, from the vector boson scattering processes discussed above we obtain:

$$\cos^2(\beta - \alpha) \lesssim \frac{8\sqrt{2}\pi v^2 - m_{h^0}^2}{m_{H^0}^2 - m_{h^0}^2} \simeq \left(\frac{1500 \text{ GeV}}{m_{H^0}} \right)^2, \quad (\text{E.22})$$

$$\cos^2(\beta - \alpha) \lesssim \frac{6\pi v^2 - m_{h^0}^2}{m_{H^0}^2 - m_{h^0}^2} \simeq \left(\frac{1100 \text{ GeV}}{m_{H^0}} \right)^2. \quad (\text{E.23})$$

These lead to bounds on the heavy Higgs mass:

$$m_{H^0}^2 \lesssim \frac{(1500 \text{ GeV})^2}{\kappa_{ZZ}^{H^0} \kappa_{WW}^{H^0}}, \quad (\text{E.24})$$

$$m_{H^0}^2 \lesssim \left(\frac{1100 \text{ GeV}}{\kappa_{ZZ}^{H^0}} \right)^2, \quad (\text{E.25})$$

where $\kappa_{ZZ}^{H^0} = \kappa_{WW}^{H^0} = \cos(\beta - \alpha)$. These constraints show that, for a fixed m_{H^0} , there is a maximum allowed strength of its coupling to vector bosons, and conversely, for fixed couplings, a maximum allowed m_{H^0} .

E.7.2. GM Model: Bound on the Fiveplet Mass and s_H

For the process $W_L^+ W_L^- \rightarrow Z_L Z_L$ in the GM model, the zeroth partial wave amplitude a_0 receives contributions from h^0 , H^0 , and the custodial fiveplet H_5^0 as well as the charged scalars H_5^\pm . The high-energy limit gives:

$$-\frac{1}{v^2} \frac{1}{\sqrt{2}} \left[(\kappa_{WW}^{h^0} \kappa_{ZZ}^{h^0}) m_{h^0}^2 + (\kappa_{WW}^{H^0} \kappa_{ZZ}^{H^0}) m_{H^0}^2 + (\kappa_{WW}^{H_5^0} \kappa_{ZZ}^{H_5^0}) m_5^2 + 2(\kappa_{WZ}^{H_5^+})^2 m_5^2 \right] = 16\pi a_0, \quad (\text{E.26})$$

$$-\frac{1}{v^2} \frac{1}{\sqrt{2}} \left[m_{h^0}^2 + \frac{5}{3} s_H^2 m_{h^0}^2 - \frac{5}{3} s_H^2 m_{H^0}^2 - \frac{5}{3} s_H^2 m_5^2 \right] = 16\pi a_0, \quad (\text{E.27})$$

which leads to the bound:

$$s_H^2 \leq \frac{3}{5\sqrt{2}} \frac{16\pi v^2 - m_{h^0}^2}{m_{h^0}^2 - m_5^2} \approx \frac{(800 \text{ GeV})^2}{m_5^2}. \quad (\text{E.28})$$

As in the 2HDM, this can also be interpreted as an upper bound on the fiveplet mass m_5 for a given mixing angle Θ_H (including the special case $\kappa_{WW}^{H^0} = 0$). The decoupling of the triplet vev must occur at least as $1/m_5^2$ for large m_5 .

E.7.3. Septet Model: Constraint on s_7

Combining the unitarity sum rule and the mass bound from the $W^\pm Z \rightarrow W^\pm Z$ scattering amplitude, an upper limit on the septet vev parameter s_7 can be derived in terms of the charged scalar masses. Setting $\kappa_V^H = 0$ for a conservative bound gives:

$$s_7^2 \leq \frac{1}{15} \frac{8\pi v^2 - m_h^2}{2s_\gamma^2 m_{H_1^+}^2 + 2c_\gamma^2 m_{H_2^+}^2 + m_h^2} \simeq \frac{(225 \text{ GeV})^2}{s_\gamma^2 m_{H_1^+}^2 + c_\gamma^2 m_{H_2^+}^2}, \quad (\text{E.29})$$

where s_γ and c_γ are sine and cosine of the charged scalar mixing angle.

F. Reference plots for κ_V vs. mixing angles at several α

This appendix includes plots for reference of the effective Higgs and vector boson couplings for the three models (2HDM, GM and the Septet) as functions of their mixing angles, shown for four representative values of the CP-even mixing angle, $\alpha \in \{\pi/6, \pi/4, \pi/2, \pi\}$, as seen in Fig. F.1. The analytic expressions used in the scans are those listed in Table 4.2 and derived in Chapter 3 (see also Refs. [13, 17]).

$$2\text{HDM}: \quad \kappa_V^{h^0} = \sin(\beta - \alpha), \quad \kappa_V^{H^0} = \cos(\beta - \alpha), \quad (\text{F.1})$$

$$\text{GM: } \kappa_V^{h^0} = c_H c_\alpha - \sqrt{\frac{8}{3}} s_H s_\alpha, \quad \kappa_V^{H^0} = c_H s_\alpha + \sqrt{\frac{8}{3}} s_H c_\alpha, \quad (\text{F.2})$$

$$\kappa_V^{H_5^0} = \frac{1}{\sqrt{3}} s_H, \quad \kappa_{WW}^{H_5^{++}} = \sqrt{2} s_H, \quad (\text{F.3})$$

$$\text{Septet: } \kappa_V^h = c_7 c_\alpha - 4 s_7 s_\alpha, \quad \kappa_V^H = c_7 s_\alpha + 4 s_7 c_\alpha, \quad \kappa_{WW}^{H^{++}} = \sqrt{15} s_7. \quad (\text{F.4})$$

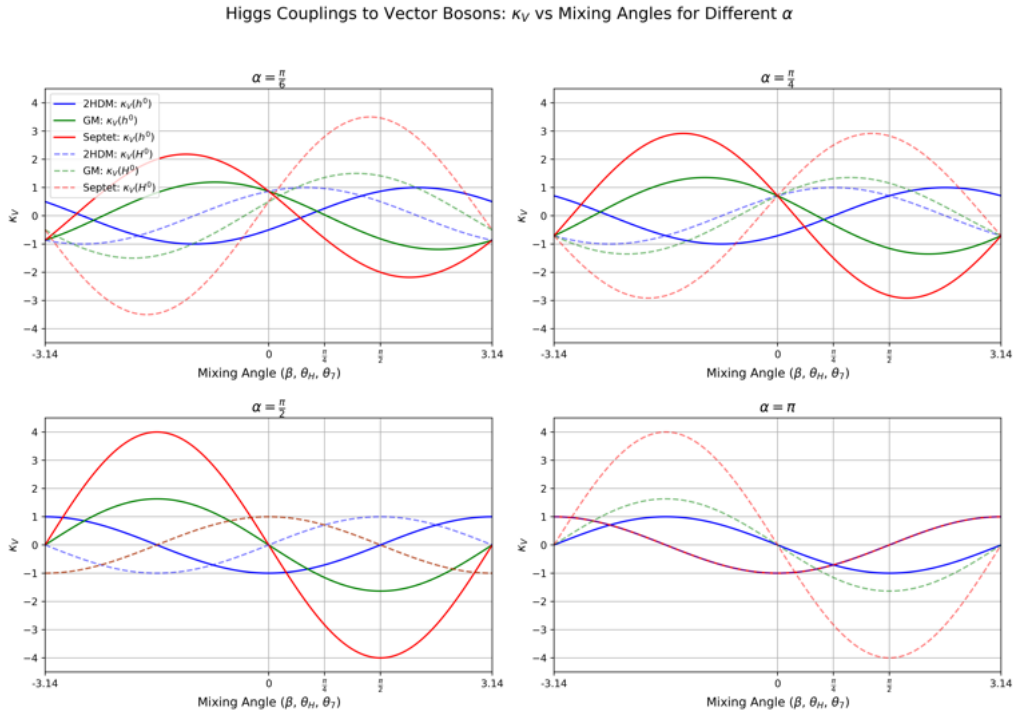


Figure F.1.: Effective couplings κ_V versus mixing angles for several fixed α values. Solid (dashed) lines show the h^0 (H^0) couplings in each model.

G. HiggsTools Analysis: Reference paper comparison and consistency checks

This appendix collects diagnostic overlays that compare our model predictions with the observed and expected 95% CL limits published by the experiments. These figures are used to validate the pipeline and to illustrate the correspondence between our results and the reference analyses. The exclusion decision in the main text is taken directly from `HiggsBounds` (selection by expected sensitivity and decision by the observed ratio), not from the derived curves shown here.

G.1. Channel wise comparison plots with reference papers

CMS: $ggH \rightarrow \tau\tau$ (Run 2)

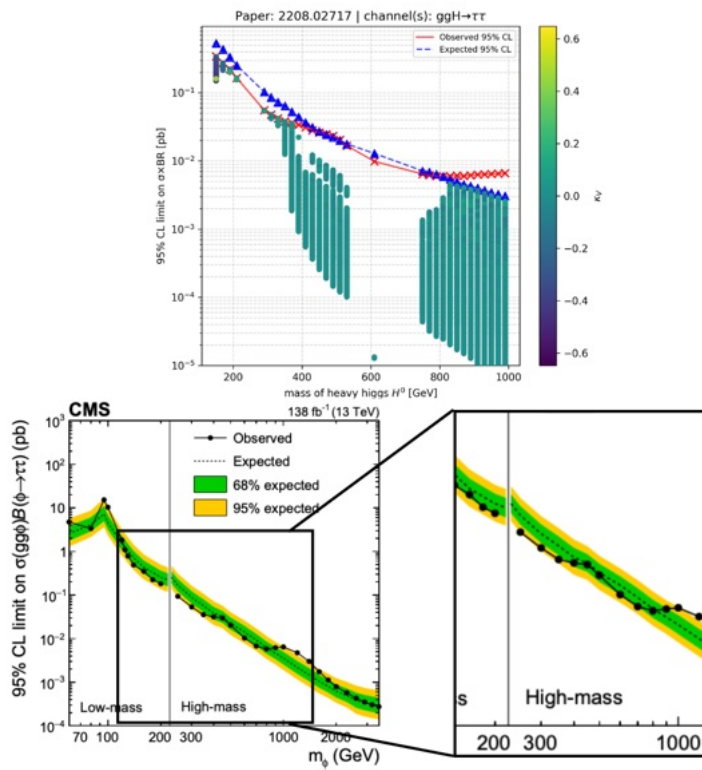


Figure G.1.: Comparison to CMS $ggH \rightarrow \tau\tau$ limits (138 fb^{-1}) [41]. Top: our overlay with observed/expected curves from the `HiggsTools` dataset and allowed points coloured by $\kappa_V^{H^0}$. Bottom: the corresponding CMS summary panel (units as in the original paper).

ATLAS: ggH , VBF $\rightarrow ZZ$ (Run 2)

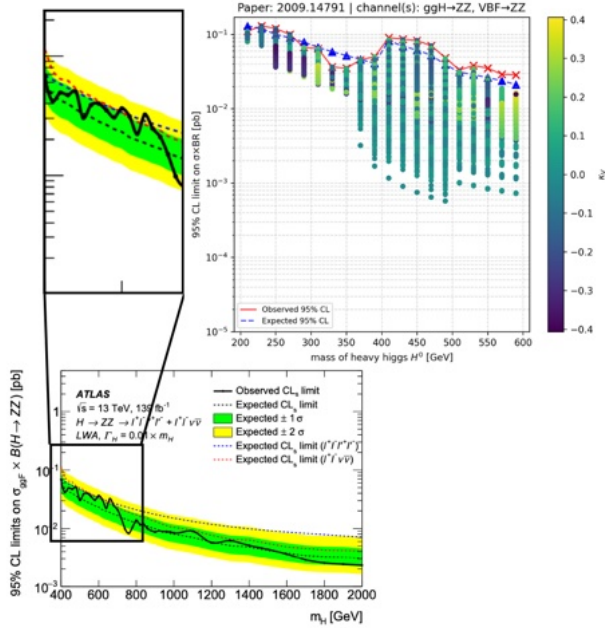


Figure G.2.: Comparison to ATLAS $H \rightarrow ZZ$ limits with ggH and VBF categories (139 fb^{-1}) [36]. Right: our overlay (pb); left/bottom: ATLAS reference panel (fb).

ATLAS: heavy resonance $\rightarrow VV$

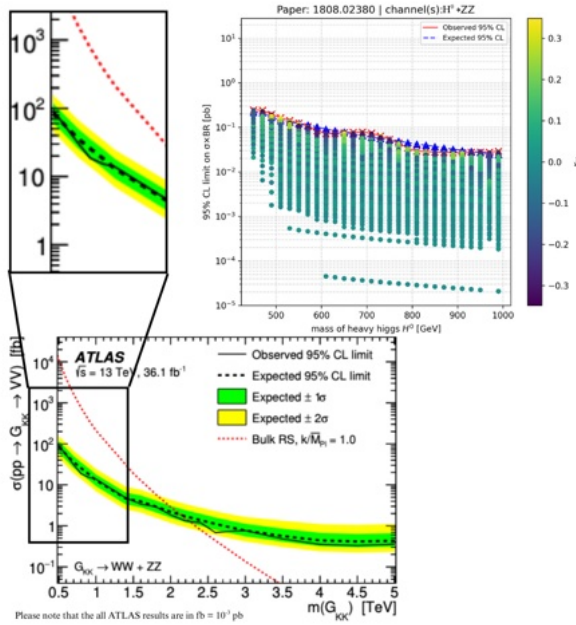


Figure G.3.: Overlay for a high-mass $H^0 \rightarrow ZZ$ comparison using the `HiggsTools` entry mapped to Ref. [45]. The ATLAS panel (bottom) is shown for visual scale (fb); the overlay (top right) is in pb.

ATLAS: $ggH \rightarrow \tau\tau$ (Run 2)

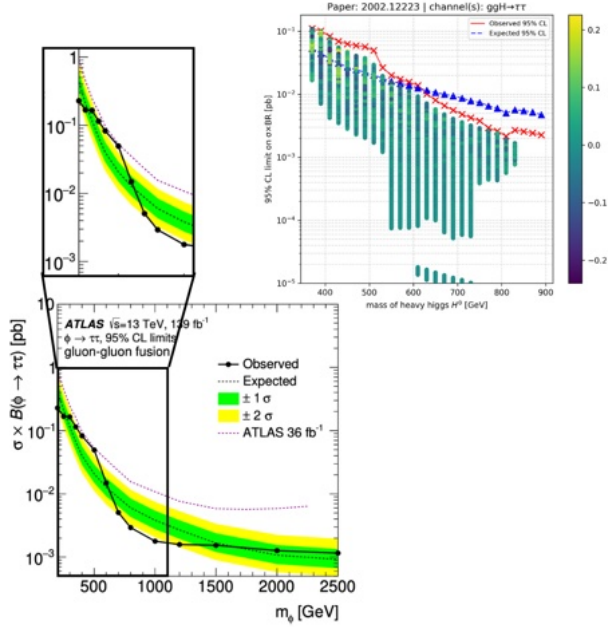


Figure G.4.: Comparison to ATLAS $ggH \rightarrow \tau\tau$ limits (139 fb^{-1}) [39]. Top right: our overlay; bottom: ATLAS reference figure.

CMS: VBF $\rightarrow ZZ$ (early Run 2)

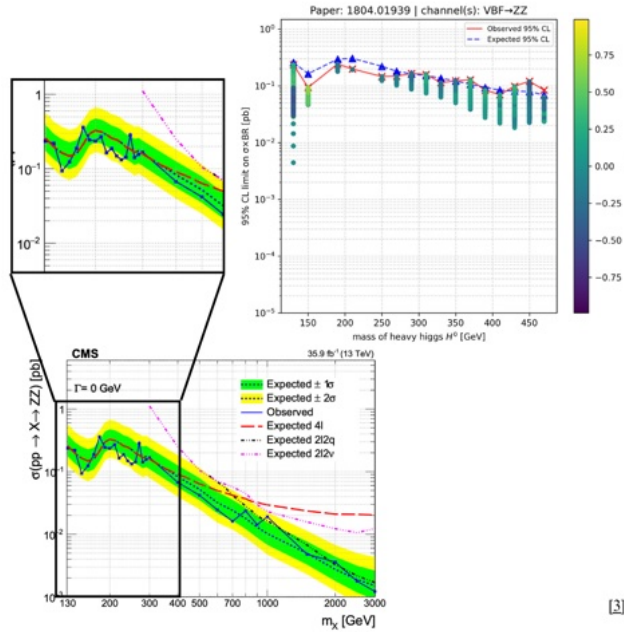


Figure G.5.: Comparison to CMS VBF $H \rightarrow ZZ$ limits (35.9 fb^{-1}) [42]. Right: our overlay in pb; left/bottom: CMS panel as published.

ATLAS: VBF $\rightarrow \gamma\gamma$ (Run 1, for completeness)

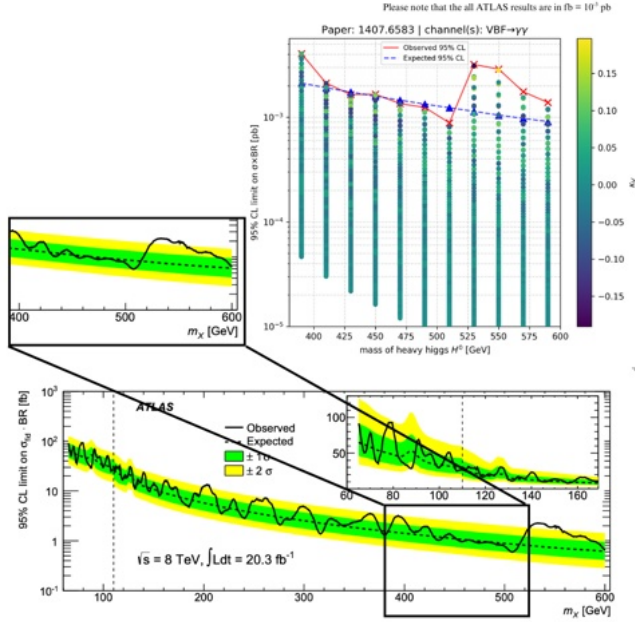


Figure G.6.: Comparison to ATLAS VBF $\gamma\gamma$ limits at 8 TeV [43]. Our overlay uses the `HiggsTools` entry for this analysis (top right); the ATLAS panel (bottom) is reproduced for context (fb).

G.2. Model-wise most sensitive $\sigma \times BR$ bands

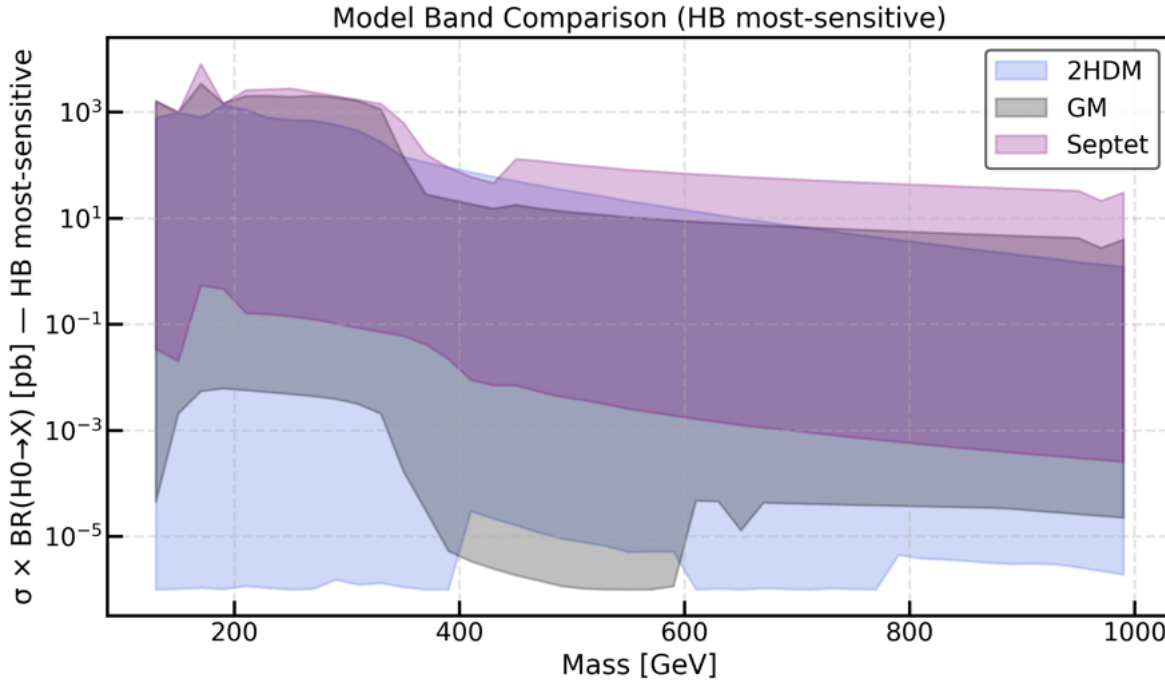


Figure G.7.: Envelope of $(\sigma \times BR)$ values over the most sensitive analysis at each point, shown versus m_{H^0} for the three benchmark models. Shaded bands indicate the range spanned by excluded points after the filters of Sec. 5.3. Note that while the bands appear continuous, our scan used a mass step of $\Delta m = 20$ GeV; the bands are a visual aid.

G.2.1. Heatmaps: most-sensitive channel in the $(m_{H^0}, \kappa_V^{H^0})$ plane

The heatmaps color each bin of the $(m_{H^0}, \kappa_V^{H^0})$ plane with the identifies most sensitive channel at that point. This gives a direct map from mass and coupling to the search topology that sets the constraint in that region. For the allowed sample, it also indicates which channels are expected to contribute in different mass ranges and helps visualize the overall $\kappa_V^{H^0}$ range inferred from the data.

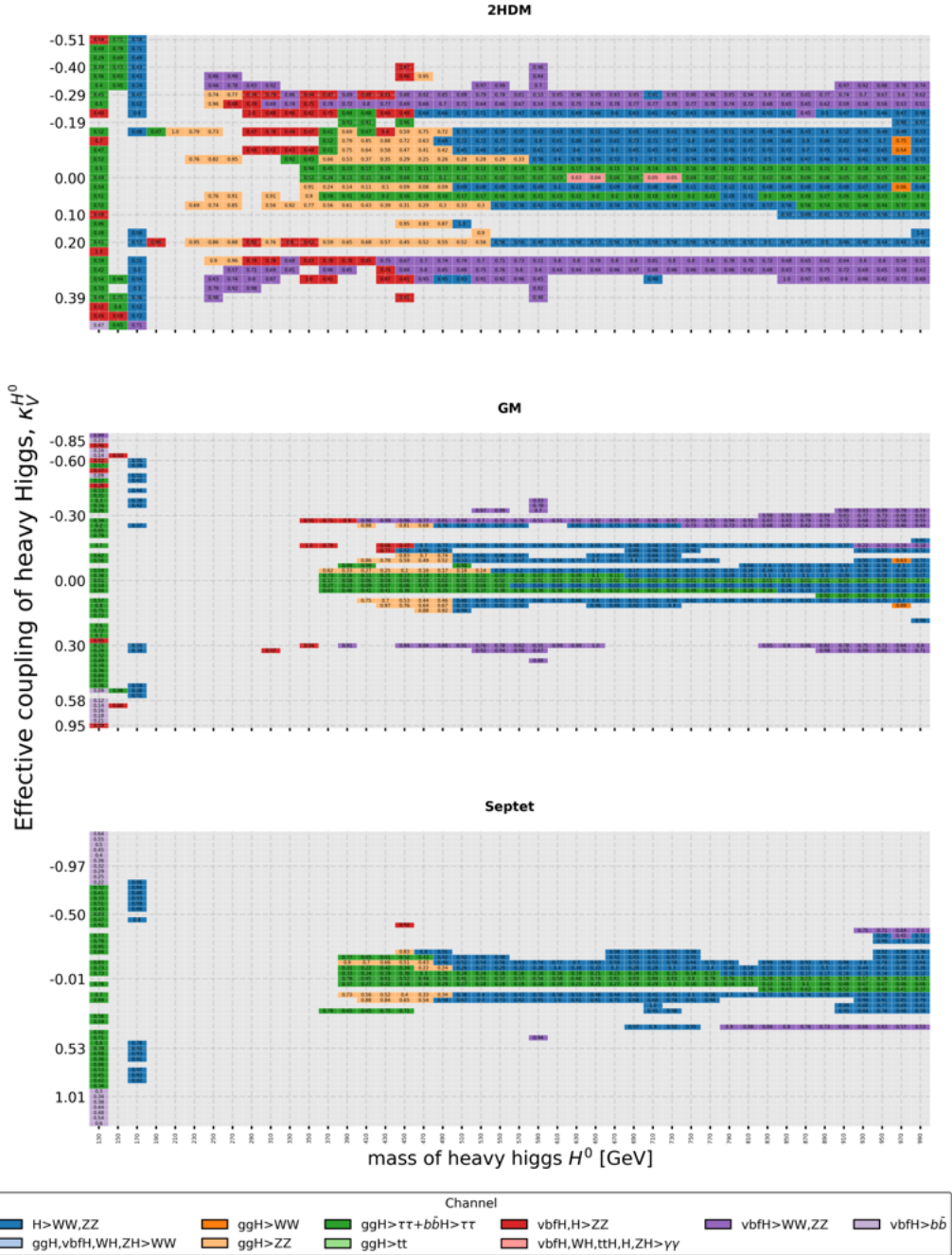


Figure G.8.: Most-sensitive channel across the $(m_{H^0}, \kappa_V^{H^0})$ plane for the three models. Each pixel indicates the production–decay topology that provides the most sensitive channel in that region. We also indicate the obsRatio of each bin.

Bibliography

- [1] M. Tanabashi et al. “Review of Particle Physics”. In: *Phys. Rev. D* 98.3 (2018), p. 030001. DOI: 10.1103/PhysRevD.98.030001.
- [2] Matthew D. Schwartz. *Quantum Field Theory and the Standard Model*. Cambridge University Press, Mar. 2014. ISBN: 978-1-107-03473-0, 978-1-107-03473-0.
- [3] Georges Aad and Andreas Schaelicke. “Observation of a new particle in the search for the Standard Model Higgs boson with the ATLAS detector at the LHC”. In: *Phys.Lett. B*716 (Sept. 2012), pp. 1–29.
- [4] S. Chatrchyan, V. Khachatryan, and A.M. Sirunyan. “Observation of a new boson at a mass of 125 GeV with the CMS experiment at the LHC”. In: *Physics Letters B* 716.1 (2012), pp. 30–61. ISSN: 0370-2693. DOI: <https://doi.org/10.1016/j.physletb.2012.08.021>. URL: <https://www.sciencedirect.com/science/article/pii/S0370269312008581>.
- [5] F. Englert and R. Brout. “Broken Symmetry and the Mass of Gauge Vector Mesons”. In: *Phys. Rev. Lett.* 13 (9 1964), pp. 321–323. DOI: 10.1103/PhysRevLett.13.321. URL: <https://link.aps.org/doi/10.1103/PhysRevLett.13.321>.
- [6] Dhananjay Saikumar. *Exploring the Frontiers: Challenges and Theories Beyond the Standard Model*. 2024. arXiv: 2404.03666 [hep-ph]. URL: <https://arxiv.org/abs/2404.03666>.
- [7] Philipp Basler, Margarete Mühlleitner, and Jonas Müller. *Electroweak Baryogenesis in the CP-Violating Two-Higgs-Doublet Model*. 2021. arXiv: 2108.03580 [hep-ph]. URL: <https://arxiv.org/abs/2108.03580>.
- [8] Marcel Krause. “On the Renormalization of the Two-Higgs-Doublet Model”. In: 2016. URL: <https://api.semanticscholar.org/CorpusID:125339200>.
- [9] G. C. Branco et al. “Theory and phenomenology of two-Higgs-doublet models”. In: *Phys. Rep.* 516.1-2 (2012), pp. 1–102. DOI: 10.1016/j.physrep.2012.02.002. URL: <http://dx.doi.org/10.1016/j.physrep.2012.02.002>.
- [10] John F. Gunion and Howard E. Haber. “CP-conserving two-Higgs-doublet model: The approach to the decoupling limit”. In: *Physical Review D* 67.7 (Apr. 2003). ISSN: 1089-4918. DOI: 10.1103/physrevd.67.075019. URL: <http://dx.doi.org/10.1103/PhysRevD.67.075019>.
- [11] John F. Gunion et al. *The Higgs Hunter’s Guide*. Vol. 80. 2000. ISBN: 978-0-429-49644-8. DOI: 10.1201/9780429496448.

- [12] Cheng-Wei Chiang and Kei Yagyu. “Testing the custodial symmetry in the Higgs sector of the Georgi-Machacek model”. In: *Journal of High Energy Physics* 2013 (Nov. 2012). DOI: 10.1007/JHEP01(2013)026.
- [13] Heather E. Logan. “Lectures on perturbative unitarity and decoupling in Higgs physics”. In: (July 2022). arXiv: 2207.01064 [hep-ph].
- [14] Katy Hartling, Kunal Kumar, and Heather Logan. “The decoupling limit in the Georgi-Machacek model”. In: *Physical Review D* 90 (Apr. 2014). DOI: 10.1103/PhysRevD.90.015007.
- [15] Ting-Kuo Chen et al. “Updated constraints on the Georgi-Machacek model and its electroweak phase transition and associated gravitational waves”. In: *Phys. Rev. D* 106 (5 2022), p. 055019. DOI: 10.1103/PhysRevD.106.055019. URL: <https://link.aps.org/doi/10.1103/PhysRevD.106.055019>.
- [16] C. Alvarado, L. Lehman, and B. Ostdiek. “Surveying the scope of the SU(2) L scalar septet sector”. In: *Journal of High Energy Physics* 2014.5 (May 2014). ISSN: 1029-8479. DOI: 10.1007/jhep05(2014)150. URL: [http://dx.doi.org/10.1007/JHEP05\(2014\)150](http://dx.doi.org/10.1007/JHEP05(2014)150).
- [17] Mary-Jean Harris and Heather E. Logan. “Constraining the scalar septet model through vector boson scattering”. In: *Physical Review D* 95.9 (May 2017). ISSN: 2470-0029. DOI: 10.1103/physrevd.95.095003. URL: <http://dx.doi.org/10.1103/PhysRevD.95.095003>.
- [18] Junji Hisano and Koji Tsumura. “Higgs boson mixes with an $\langle\!\langle$ mml:math xmlns:mml="http://www.w3.org/1998/Math/MathML" display="block">\langle\!\langlemml:mi>S $\rangle\!\rangle$ $\langle\!\langle$ mml:mi>U $\rangle\!\rangle$ $\langle\!\langle$ mml:mo stretchy="false">(<\!mml:mo stretchy="false">) $\rangle\!\rangle$ $\langle\!\langle$ mml:mo> $\rangle\!\rangle$ $\langle\!\langle$ mml:math> septet representation”. In: *Physical Review D* 87.5 (Mar. 2013). ISSN: 1550-2368. DOI: 10.1103/physrevd.87.053004. URL: <http://dx.doi.org/10.1103/PhysRevD.87.053004>.
- [19] Heather E. Logan. *TASI 2013 lectures on Higgs physics within and beyond the Standard Model*. 2022. arXiv: 1406.1786 [hep-ph]. URL: <https://arxiv.org/abs/1406.1786>.
- [20] A. Tumasyan et al. “A portrait of the Higgs boson by the CMS experiment ten years after the discovery”. In: *Nature* 607.7917 (July 2022), 60–68. ISSN: 1476-4687. DOI: 10.1038/s41586-022-04892-x. URL: <http://dx.doi.org/10.1038/s41586-022-04892-x>.
- [21] Aron J. Beekman, Louk Rademaker, and Jasper van Wezel. “An introduction to spontaneous symmetry breaking”. In: *SciPost Phys. Lect. Notes* (2019), p. 11. DOI: 10.21468/SciPostPhysLectNotes.11. URL: <https://scipost.org/10.21468/SciPostPhysLectNotes.11>.
- [22] S. Dawson. *Introduction to Electroweak Symmetry Breaking*. 1999. arXiv: hep-ph/9901280 [hep-ph]. URL: <https://arxiv.org/abs/hep-ph/9901280>.
- [23] Avelino Vicente. “Phenomenology of supersymmetric neutrino mass models”. In: (Apr. 2011).

- [24] Benjamin W. Lee, C. Quigg, and H. B. Thacker. “The Strength of Weak Interactions at Very High-Energies and the Higgs Boson Mass”. In: *Phys. Rev. Lett.* 38 (1977), pp. 883–885. DOI: 10.1103/PhysRevLett.38.883.
- [25] Cheng Li. *Phenomenology of extended two-Higgs-doublets models*. Universitaet Hamburg (Germany), 2023.
- [26] Philipp Basler, Margarete Mühlleitner, and Jonas Müller. *Electroweak Baryogenesis in the CP-Violating Two-Higgs-Doublet Model*. arXiv: 2108 . 03580 [hep-ph]. URL: <https://arxiv.org/abs/2108.03580>.
- [27] Ben Keeshan, Heather E. Logan, and Terry Pilkington. “Custodial symmetry violation in the Georgi-Machacek model”. In: *Physical Review D* 102.1 (July 2020). ISSN: 2470-0029. DOI: 10.1103/physrevd.102.015001. URL: <http://dx.doi.org/10.1103/PhysRevD.102.015001>.
- [28] Wolfram Research, Inc. *Mathematica, Version 14.0*. Champaign, IL, 2024. URL: <https://www.wolfram.com/mathematica>.
- [29] Vladyslav Shtabovenko, Rolf Mertig, and Frederik Orellana. “FeynCalc 9.3: New features and improvements”. In: *Computer Physics Communications* 256 (Nov. 2020), p. 107478. ISSN: 0010-4655. DOI: 10.1016/j.cpc.2020.107478. URL: <http://dx.doi.org/10.1016/j.cpc.2020.107478>.
- [30] H. Eck, R. Mertig, and D. Mücke. *FeynArts 3.9*. <http://www.feynarts.de>. Version 3.9. 2000.
- [31] F. Staub. *Sarah*. 2012. arXiv: 0806 . 0538 [hep-ph]. URL: <https://arxiv.org/abs/0806.0538>.
- [32] Philip Bechtle et al. “HiggsBounds-5: testing Higgs sectors in the LHC 13 TeV Era”. In: *The European Physical Journal C* 80.12 (Dec. 2020). ISSN: 1434-6052. DOI: 10.1140/epjc/s10052-020-08557-9. URL: <http://dx.doi.org/10.1140/epjc/s10052-020-08557-9>.
- [33] Philip Bechtle et al. “HiggsSignals-2: probing new physics with precision Higgs measurements in the LHC 13 TeV era”. In: *The European Physical Journal C* 81.2 (Feb. 2021). ISSN: 1434-6052. DOI: 10.1140/epjc/s10052-021-08942-y. URL: <http://dx.doi.org/10.1140/epjc/s10052-021-08942-y>.
- [34] Henning Bahl et al. “HiggsTools: BSM scalar phenomenology with new versions of HiggsBounds and HiggsSignals”. In: *Computer Physics Communications* 291 (Oct. 2023), p. 108803. ISSN: 0010-4655. DOI: 10.1016/j.cpc.2023.108803. URL: <http://dx.doi.org/10.1016/j.cpc.2023.108803>.

- [35] In: *Physics Reports* 1115 (Apr. 2025), 368–447. ISSN: 0370-1573. DOI: 10.1016/j.physrep.2024.09.004. URL: <http://dx.doi.org/10.1016/j.physrep.2024.09.004>.

- [36] G. Aad et al. “Search for heavy resonances decaying into a pair of Z bosons in the

$$\ell^+ \ell^- \ell'^+ \ell'^-$$

and

$$\ell^+ \ell^- v \bar{v}$$

final states using 139

$$\text{fb}^{-1}$$

of proton–proton collisions at

$$\sqrt{s} = 13$$

TeV with the ATLAS detector”. In: *The European Physical Journal C* 81.4 (Apr. 2021). ISSN: 1434-6052. DOI: 10.1140/epjc/s10052-021-09013-y. URL: <http://dx.doi.org/10.1140/epjc/s10052-021-09013-y>.

- [37] A. M. Sirunyan et al. “Search for additional neutral MSSM Higgs bosons in the final state in proton-proton collisions at

$$\sqrt{s} = 13$$

TeV”. In: *Journal of High Energy Physics* 2018.9 (Sept. 2018). ISSN: 1029-8479. DOI: 10.1007/jhep09(2018)007. URL: [http://dx.doi.org/10.1007/JHEP09\(2018\)007](http://dx.doi.org/10.1007/JHEP09(2018)007).

- [38] “Update on the search for the standard model Higgs boson in pp collisions at the LHC decaying to W + W in the fully leptonic final state”. In: (Mar. 2013).

- [39] G. Aad et al. “Search for Heavy Higgs Bosons Decaying into Two Tau Leptons with the ATLAS Detector Using $\langle \text{mml:math} \text{ xmlns:mml="http://www.w3.org/1998/Math/MathML" } \text{ display="inline"} \rangle \langle \text{mml:mi} \rangle p \langle / \text{mml:mi} \rangle \langle \text{mml:mi} \rangle p \langle / \text{mml:mi} \rangle \langle / \text{mml:math} \rangle$ Collisions at $\langle \text{mml:math} \text{ xmlns:mml="http://www.w3.org/1998/Math/MathML" } \text{ display="inline"} \rangle \langle \text{mml:mrow} \rangle \langle \text{mml:msqrt} \rangle \langle \text{mml:math} \text{ xmlns:mml="http://www.w3.org/1998/Math/MathML" } \text{ display="block"} \rangle \langle \text{mml:math} \text{ xmlns:mml="http://www.w3.org/1998/Math/MathML" } \text{ display="block"} \rangle$ In: *Physical Review Letters* 125.5 (July 2020). ISSN: 1079-7114. DOI: 10.1103/physrevlett.125.051801. URL: <http://dx.doi.org/10.1103/PhysRevLett.125.051801>.

- [40] A. Tumasyan et al. “Search for heavy resonances decaying to $\langle \text{mml:math} \text{ xmlns:mml="http://www.w3.org/1998/Math/MathML" } \text{ display="block" } \rangle \langle \text{mml:mrow} \rangle \langle \text{mml:mi} \rangle W \langle / \text{mml:mi} \rangle \langle / \text{mml:mrow} \rangle \langle \text{mml:mrow} \rangle \langle \text{mml:mi} \rangle W \langle / \text{mml:mi} \rangle \langle / \text{mml:mrow} \rangle \langle \text{mml:math} \text{ xmlns:mml="http://www.w3.org/1998/Math/MathML" } \text{ display="block" } \rangle \langle \text{mml:mrow} \rangle \langle \text{mml:msub} \rangle \langle \text{mml:math} \text{ xmlns:mml="http://www.w3.org/1998/Math/MathML" } \text{ display="block" } \rangle \langle \text{mml:math} \text{ xmlns:mml="http://www.w3.org/1998/Math/MathML" } \text{ display="block" } \rangle \langle / \text{mml:math} \rangle \langle / \text{mml:msub} \rangle \langle / \text{mml:mrow} \rangle \langle / \text{mml:math} \rangle$ or $\langle \text{mml:math} \text{ xmlns:mml="http://www.w3.org/1998/Math/MathML" } \text{ display="block" } \rangle \langle \text{mml:mrow} \rangle \langle \text{mml:msub} \rangle \langle \text{mml:math} \text{ xmlns:mml="http://www.w3.org/1998/Math/MathML" } \text{ display="block" } \rangle \langle \text{mml:math} \text{ xmlns:mml="http://www.w3.org/1998/Math/MathML" } \text{ display="block" } \rangle \langle / \text{mml:math} \rangle \langle / \text{mml:msub} \rangle \langle / \text{mml:mrow} \rangle \langle / \text{mml:math} \rangle$ boson pairs in a final state consisting of a lepton and a large-radius jet in proton-proton colli-

- sions at <mml:math xmlns:mml="http://www.w3.org/1998/Math/MathML" display="inline"><mml:mrow> In: Physical Review D 105.3 (Feb. 2022). ISSN: 2470-0029. DOI: 10.1103/physrevd.105.032008. URL: <http://dx.doi.org/10.1103/PhysRevD.105.032008>.
- [41] A. Tumasyan et al. “Searches for additional Higgs bosons and for vector leptoquarks in final states in proton-proton collisions at $\sqrt{s} = 13 \text{ TeV}$ ”. In: Journal of High Energy Physics 2023.7 (July 2023). ISSN: 1029-8479. DOI: 10.1007/jhep07(2023)073. URL: [http://dx.doi.org/10.1007/JHEP07\(2023\)073](http://dx.doi.org/10.1007/JHEP07(2023)073).
- [42] A. M. Sirunyan et al. “Search for a new scalar resonance decaying to a pair of Z bosons in proton-proton collisions at $sqrts = 13 \text{ TeV}$ ”. In: Journal of High Energy Physics 2018.6 (June 2018). ISSN: 1029-8479. DOI: 10.1007/jhep06(2018)127. URL: [http://dx.doi.org/10.1007/JHEP06\(2018\)127](http://dx.doi.org/10.1007/JHEP06(2018)127).
- [43] G. Aad et al. “Search for Scalar Diphoton Resonances in the Mass Range 65–600 GeV with the ATLAS Detector in Data at In: Physical Review Letters 113.17 (Oct. 2014). ISSN: 1079-7114. DOI: 10.1103/physrevlett.113.171801. URL: <http://dx.doi.org/10.1103/PhysRevLett.113.171801>.
- [44] V. Khachatryan et al. “Search for the standard model Higgs boson produced through vector boson fusion and decaying to $b\bar{b}$ ”. In: Physical Review D 92.3 (Aug. 2015). ISSN: 1550-2368. DOI: 10.1103/physrevd.92.032008. URL: <http://dx.doi.org/10.1103/PhysRevD.92.032008>.
- [45] M. Aaboud et al. “Combination of searches for heavy resonances decaying into bosonic and leptonic final states using proton-proton collision data at with the ATLAS detector”. In: Physical Review D 98.5 (Sept. 2018). ISSN: 2470-0029. DOI: 10.1103/physrevd.98.052008. URL: <http://dx.doi.org/10.1103/PhysRevD.98.052008>.

Eidesstattliche Versicherung

Ich versichere hiermit an Eides statt, dass ich diese Arbeit im Rahmen der Vorlesung Beschleuniger- und Teilchenphysik selbstständig verfasst und keine anderen als die angegebenen Hilfsmittel – insbesondere keine Internetquellen, außer denen, die im Quellenverzeichnis genannt sind – verwendet habe. Alle wörtlich oder sinngemäß aus Veröffentlichungen übernommenen Passagen sind als solche gekennzeichnet. Ich versichere außerdem, dass ich die Arbeit keinem anderen Prüfungsverfahren unterzogen habe und dass die eingereichte schriftliche Fassung mit der auf dem elektronischen Datenträger übereinstimmt. Mit der Veröffentlichung meiner Masterarbeit bin ich einverstanden.

Hamburg, den _____ 08.10.2025

Unterschrift: _____

